

TECHNISCHE UNIVERSITÄT MÜNCHEN

Max-Planck-Institut für Astrophysik

**Multidimensional hydrodynamic simulations  
of the core helium flash in low-mass stars**

**Miroslav Mocák**

Vollständiger Abdruck der von der Fakultät für Physik der Technischen Universität München zur  
Erlangung des akademischen Grades eines

*Doktors der Naturwissenschaften*

genehmigten Dissertation.

Vorsitzender: Univ.-Prof. Dr. St. Paul

Prüfer der Dissertation:

1. Priv.-Doz. Dr. E. Müller

2. Univ.-Prof. Dr. H. Friedrich

Die Dissertation wurde am 18. 12. 2008 bei der Technischen Universität München eingereicht  
und durch die Fakultät für Physik am 23. 01. 2009 angenommen.



# Contents

<b>1. Introduction</b>	<b>5</b>
1.1. The Core Helium Flash	6
1.1.1. Hydrostatic Calculations	9
1.1.2. Hydrodynamic Calculations	10
1.2. Aims	11
<b>2. Properties of the System</b>	<b>13</b>
2.1. Regime	13
2.2. Convection and Turbulence	14
2.3. Important Time Scales	17
2.4. Thermonuclear Reactions	18
2.5. Neutrinos	19
2.6. Thermal Transport	19
2.7. Geometry	20
<b>3. Input Physics</b>	<b>21</b>
3.1. Evolutionary Equations	21
3.2. Equation of State	22
3.3. Nuclear Burning	22
3.4. Neutrino Emission	24
3.5. Thermal Transport	24
<b>4. Code</b>	<b>27</b>
4.1. Hydrodynamics	28
4.1.1. Piecewise Parabolic Method	28
4.1.2. Courant-Friedrich-Levy Condition	32
4.1.3. Double Mach Reflection of a Strong Shock	32
4.2. Nuclear Reactions	32
4.2.1. One-Zone Nuclear Burning	35
4.2.2. White Dwarf Detonation Problem	36
4.3. Screening	37
4.4. Neutrinos	37
4.5. Gravitation	38
4.5.1. Polytropic Star	38
4.6. Thermal Transport	39
4.7. Performance and Parallelization	40
<b>5. Initial Stellar Models</b>	<b>41</b>
5.1. General Remarks	41
5.2. Stabilization	42
5.3. The Models	42

5.3.1. Model <b>M</b> : Mass = $1.25 M_{\odot}$ and $Z = 0.02$ . . . . .	43
5.3.2. Model <b>DM</b> : Mass = $0.85 M_{\odot}$ and $Z = 0.001$ . . . . .	45
5.3.3. Model <b>JW</b> : Mass = $1.49 M_{\odot}$ and $Z = 0.02$ . . . . .	45
5.3.4. Model <b>SC</b> : Mass = $0.85 M_{\odot}$ and $Z = 0.0$ . . . . .	45
<b>6. One-Dimensional Hydrodynamic Simulations</b>	<b>49</b>
6.1. Temporal Evolution . . . . .	49
<b>7. Two-Dimensional Hydrodynamic Simulations</b>	<b>51</b>
7.1. Temporal Evolution . . . . .	51
7.2. Energy Fluxes . . . . .	55
7.3. Turbulent Entrainment . . . . .	57
7.4. Long-Term Evolution . . . . .	59
7.5. Simulations with Different Resolution . . . . .	62
7.6. Other Two-Dimensional Simulations . . . . .	62
7.6.1. Model DM . . . . .	63
7.6.2. Model JW . . . . .	66
7.6.3. Model SC . . . . .	69
<b>8. Three-Dimensional Hydrodynamic Simulations</b>	<b>73</b>
8.1. Temporal Evolution . . . . .	74
8.2. Size and Structure of Convective Flow . . . . .	75
8.3. Stability of the Flow Structures . . . . .	78
8.4. Turbulent Entrainment and Size of the Convection Zone . . . . .	79
8.5. Energy Fluxes . . . . .	83
8.6. The flow within the convection zone . . . . .	85
8.7. Upflow-downflow asymmetry . . . . .	86
8.8. Mixing Within The Convection Zone . . . . .	87
8.9. Mixing Length Theory and Simulations . . . . .	87
<b>9. Summary</b>	<b>91</b>
<b>A. Appendix</b>	<b>93</b>
A.1. Hydrodynamical Equations in Spherical Geometry . . . . .	93
A.2. Energy Fluxes . . . . .	94
<b>List of Figures</b>	<b>98</b>
<b>List of Tables</b>	<b>99</b>
<b>Bibliography</b>	<b>105</b>
<b>Acknowledgment</b>	<b>107</b>



*Understanding is, after all, what science is all about - and science is a great deal more than mere mindless computation.*

Roger Penrose

# 1

## Introduction

Contemporary science is able to explain many astrophysical phenomena based on observations of stars which irradiate energy during most of their life in form of photons. However, all photons come from the stellar atmosphere which is typically very thin and in terms of volume and mass covers only a minor fraction of the whole star. Since, the stellar interior is optically thick, it does not leak any radiation which we can observe and therefore remains well hidden. Most of the stars are too far away for a detection of any physical signature coming from below their atmospheres (*e.g.* neutrinos, surface oscillations, gravity waves) and moreover, current observations reveal to us only a snapshot from the evolution of stars which may take billions of year. The only way to understand stars is therefore by numerical simulations. Such a canonical stellar evolutionary simulation, based on a solution of the stellar structure equations ([Kippenhahn & Weigert 1990](#); [Weiss et al. 2004](#)) can provide us with valuable informations about the structure of a star from its center up to the surface over its whole life. The canonical simulation is typically one-dimensional, hydrostatic and employs phenomenological theories. This approach is not computationally demanding which is one of its main advantages, however, faces the problem of free parameters based on incomplete physical models which must be often calibrated in order to fit observations.

With increasing computational capabilities, the importance of multidimensional hydrodynamic simulations in stellar evolution studies grows rapidly since they are based on a solution of conservation laws and are essentially parameter free. With present supercomputers we are not able to follow the whole “hydrodynamic” life of a star but still have to rely on the canonical stellar evolutionary studies. Mutual comparison of these two approaches to stellar evolution is therefore crucial, since it can give us hints on where the canonical theory is doing fine, and where and up to what extent it fails.

The canonical stellar evolutionary calculations are typically in agreement with observations during most of the life of stars which can be represented by the Hertzsprung-Russell diagram (or H-R diagram); a graph of stellar luminosity versus surface temperature of a star. The stellar calculations can fit in many cases the diagrams very well. Problems occur when stars experience evolutionary phases which are hydrodynamic *i.e.* involving fast expansion, rapid collapse or strong turbulent convection.

While the standard stellar evolutionary calculations have been successful in reproducing obser-

vations of stars characterized by core hydrogen burning (the main sequence or MS), and of the stars that have exhausted central hydrogen and burn it only in a shell (the red giant branch or RGB), we recognize several discrepancies concerning the phases after the subsequent central helium ignition, **the core helium flash**. In particular, we recall the lack of an understanding about the horizontal-branch morphology (Catelan 2005), where the star quiescently burns helium in its core (a phase following shortly after the core helium flash). Low-luminosity carbon stars and hydrogen-deficient stars are difficult to explain as well. Since all of these (and other) problems appear after the RGB phase, it is plausible to suspect that the helium flash may be treated incorrectly in standard (hydrostatic) stellar evolutionary calculations. We hope to resolve this issue by an analysis of our hydrodynamic simulations.

## 1.1. The Core Helium Flash

In low-mass stars of mass  $0.7 M_{\odot}^1 \leq M \leq 2.2 M_{\odot}$ , the onset of helium burning constitutes a major event – the core helium flash. When the star finishes hydrogen burning period in its center and starts to leave the main sequence on the H-R diagram (Fig. 1.1), it contains a core composed of almost pure helium with a surrounding hydrogen burning shell (Fig. 1.2). The hydrogen burning shell moves outwards and leaves helium layers behind, *i.e.* the helium core grows in mass. At the same time, the helium core contracts until the central densities reach values of  $\rho_c \sim 10^6 \text{ g cm}^{-3}$  at which the plasma is electron degenerate and the supporting pressure of the electron gas stops the contraction.

The density of the ambient hydrogen burning shell is by a factor of  $10^{10}$  lower than the density in the center of the star (Fig. 1.3). Therefore, it does not have any influence on the upper layers of the helium core which on the other side has a strong influence on the hydrogen shell due to gravitational energy release in the helium core during its contraction. Refsdal & Weigert (1970) have shown that the temperature of the hydrogen burning shell  $T_H$  obeys the following relation  $T_H \propto M_{He}/R_{He}$ , where  $M_{He}$  and  $R_{He}$  are the mass and radius of the helium core, respectively. Since the electron gas is a very good heat conductor, the helium core is almost isothermal and has a temperature equal to that of the hydrogen burning shell.

The radius of objects containing degenerate matter decreases with increasing mass, therefore  $T_H$  will be rising which results in an increase of the energy production due to hydrogen burning shell, and consequently to an increase of the luminosity of the star. At the same time, outer layers of the star expand and the temperature drops on its surface *i.e.* the star becomes a red giant that climbs up the H-R diagram towards the right (Fig. 1.1).

The temperature in the helium core  $T_H$  increases due to the strong thermal coupling with the hydrogen burning shell and due to the release of the gravitational energy of the contracting core. When the temperature reaches  $\sim 10^8 \text{ K}$  in the core, the strong temperature dependent triple- $\alpha$  reaction ignites in a relatively dense environment. The ignition occurs off-center due to plasma- and photo-neutrino cooling. The neutrinos are efficiently produced only in the densest central part of the core and leave the star without interaction. Therefore, helium burning (triple- $\alpha$  reaction) begins in a concentric shell, and not in the center. This happens when the helium core of the star has a mass of  $\sim 0.45 M_{\odot}^2$ . At this point, the helium core contains a white dwarf-like degenerate structure and an off-center temperature maximum (Fig. 1.3).

<sup>1</sup> $M_{\odot}$  is a mass of Sun which is equal to  $\sim 1.98 \times 10^{33}$  grams.

<sup>2</sup>In stars with a mass less than  $0.45 M_{\odot}$  helium will never be ignited. This led Hansen (2005) to the conclusion that some bright white dwarfs observed in open clusters are  $\sim 0.5 M_{\odot}$  white dwarfs with a helium core instead of a carbon core. This may happen if mass loss during the ascent along the red giant branch is strong enough to prevent the star from reaching the core helium flash.

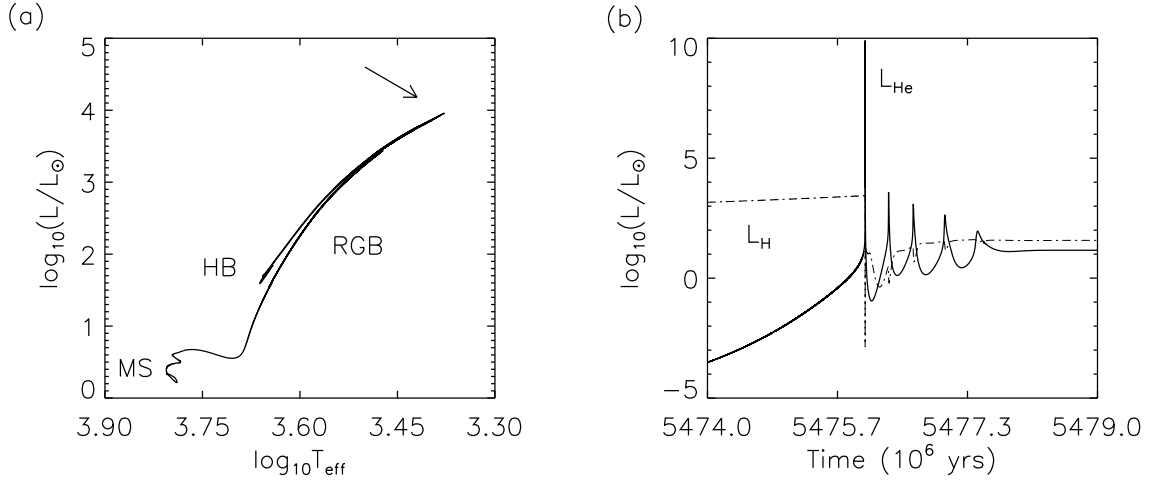


**Figure 1.1.:** (a) Theoretical evolutionary track of a  $1.25 M_{\odot}$  star with a metallicity  $Z=0.02$  in the H-R diagram. The core helium flash begins at the tip of the red giant branch indicated by the arrow (MS is the main sequence, RGB is the red giant branch, HB is the horizontal branch). (b) Temporal evolution of helium luminosity  $L_{\text{He}}$  (solid) versus the hydrogen luminosity  $L_{\text{H}}$  (dash-dotted) during the core helium flash ( $L_{\odot} \sim 3.839 \times 10^{33} \text{ erg s}^{-1}$  is a luminosity of Sun).

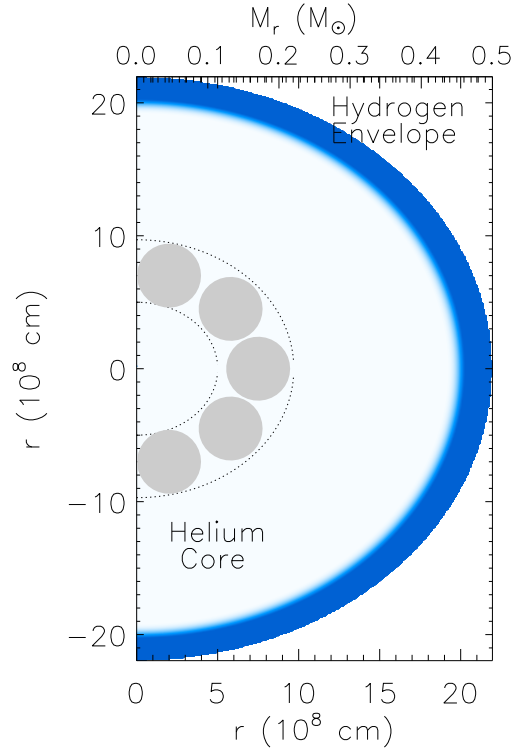


**Figure 1.2.:** Sketch of a helium core (white region) surrounded by a hydrogen burning envelope (blue layer) up to a radius  $r = 2.2 \times 10^9 \text{ cm}$  enclosing a mass  $M_r \sim 0.5 M_{\odot}$  in a  $1.25 M_{\odot}$  star with a metallicity  $Z=0.02$  near the peak of the core helium flash. The dotted lines mark boundaries of the convection zone (grey circles).

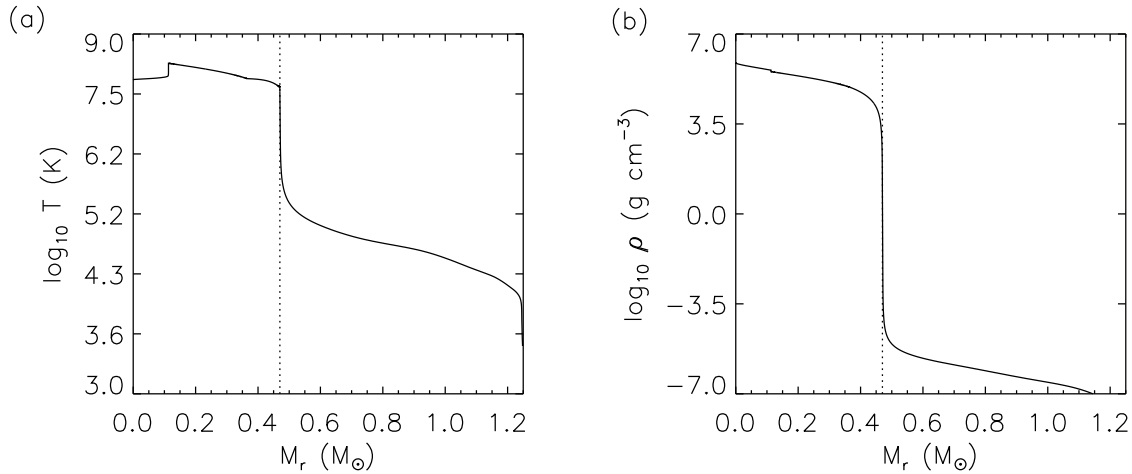


**Figure 1.3.:** (a) Temperature and (b) density profile of a  $1.25 M_{\odot}$  star with a metallicity  $Z=0.02$  at the peak of the core helium flash as a function of enclosed mass  $M_r$  at radius  $r$ . The vertical lines mark the surface of the helium core at  $M_r \sim 0.47 M_{\odot}$ .

When helium burning commences in the degenerate core, the liberated nuclear energy cannot be used to expand and cool the layers close to the temperature maximum. Instead it causes further heating and a strong increase in the nuclear energy release. Only when convection sets in can part of the excess energy be transported away from the burning regions, inhibiting a thermonuclear runaway. This convection zone never reaches the hydrogen burning shell (Fig. 1.2), unless metallicity<sup>3</sup> of the star is very small. By the end of the flash, the core has expanded to densities of the order of  $10^4 \text{ g cm}^{-3}$  and helium burning continues quiescently in the core. The star has settled onto the horizontal branch (Fig. 1.1). Given that the maximum temperature in the helium core is  $T \sim 1 \times 10^8 \text{ K}$ , the star reaches the peak in nuclear energy production rate during the core helium flash in less than  $10^4$  yrs (Fig. 1.4).

A core helium flash can be described by the following general scenario (based on the evolution of a  $1.25 M_{\odot}$  star with a metallicity  $Z=0.02$ ):

1. Helium ignition occurs off-center due to neutrino cooling and the resulting off-center temperature maximum (Fig. 1.3, Fig. 1.4). The temperature and the nuclear energy production begins to rise slowly. From the onset of core helium burning at a helium luminosity  $L_{He} \sim 10^1 L_{\odot}$ , it takes almost  $3 \times 10^4$  yrs to reach  $L_{He} \sim 10^4 L_{\odot}$  during which the core builds up a convection zone, and starts to expand slowly ( $\sim \text{m s}^{-1}$ )
2. During the next 40 yrs, the core helium flash reaches its peak with a central temperature up to  $2 \times 10^8 \text{ K}$ , and a peak luminosity of  $L_{He} \sim 10^{10} L_{\odot}$  (Fig. 1.1). At this point, the core's degeneracy is almost completely lifted, and the core expansion inhibits a further rise of the core temperature.
3. When the temperature drops in the core again, the thickness of the helium burning shell decreases. When the shell reaches a critical thickness it becomes thermally unstable *i.e.* the first core helium flash described above is followed by several subsequent mini flashes (Fig. 1.1) identified as thermal pulses by Thomas (1967) until the degeneracy is lifted completely in the helium core and the star settles down on the horizontal branch quiescently burning helium in its core.

<sup>3</sup>Metallicity is the ratio of the mass fraction of all elements heavier than helium to the whole mass of a star.

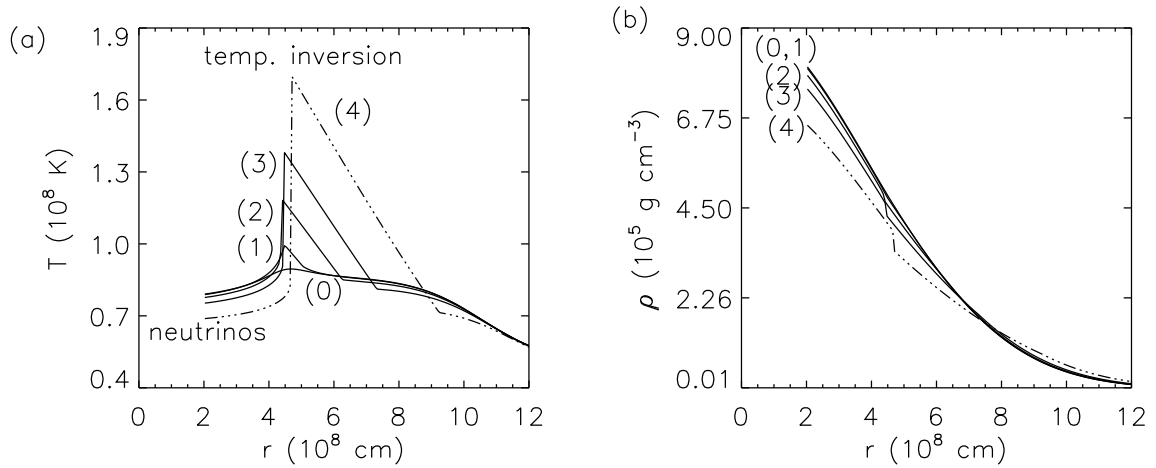


**Figure 1.4.:** (a) Temperature and (b) density profile of a  $1.25 M_{\odot}$  star with a metallicity  $Z=0.02$  at the onset of the core helium flash (0) till its peak (4). The different curves correspond to the peak of the core helium flash  $t = 0$  yrs (4) and the rest to  $t = -0.12$  yrs (3),  $t = -4.52$  yrs (2),  $t = -485$  s (1) and  $t = -8715$  yrs (0), respectively.

All these results were obtained from canonical hydrostatic stellar evolutionary calculations (see the next Sect. 1.1.1).

### 1.1.1. Hydrostatic Calculations

Stars are during most of their life in hydrostatic equilibrium, and roughly spherical. This gives one an opportunity to model the evolution of stellar structure by means of one-dimensional simulations where multidimensional flow phenomena are treated by an approximate phenomenological description (Kippenhahn & Weigert 1990; Weiss et al. 2004). Such simulations are called stellar evolutionary calculations.

Indeed, the first results on the core helium flash were gained from such one-dimensional hydrostatic numerical simulations. The star had a mass of a  $1.3 M_{\odot}$  star and a metallicity  $Z = 0.001$  (Schwarzschild & Härm 1962). This simulation was done under the assumptions of a simple equation of state consisting of an ideal ion gas and an degenerate electron gas with  $\gamma = 5/3$ . For the nuclear reactions they considered only helium and hydrogen burning approximated by a simple fit formula. In addition, they assumed the core to be in hydrostatic equilibrium and completely degenerate at the edge of the core, being surrounded by an ideal gas. They have found that the star underwent a thermal runaway due to the ignition of helium under degenerate conditions in its center. From the beginning of helium burning at a central temperature  $\sim 8.3 \times 10^7$  K, it took half a million years before helium burning started to accelerate at temperatures  $\sim 10^8$  K. From that time on, the star reached a peak core temperature of  $\sim 3.5 \times 10^8$  K and a total energy generation rate of  $\sim 10^{12} L_{\odot}$  in less than 700 yrs. Therefore, Schwarzschild and Härm called this event core helium **flash**. With improved physics and numerical approaches, similar simulations were done later by Härm & Schwarzschild (1964, 1966) with no significantly different outcome.

An interesting study was performed by Tomasko (1970) who studied the pulsational stability of the helium core during the flash. He found that perturbations in the interior of the core can propagate outwards and can be partially reflected from the relatively abrupt change in density at the edge of the core (Fig. 1.3). Upon returning to the central regions, these reflected disturbances

can enhance the central perturbations and result in a pulsation of the core. The pulsation can be energized by the high rate of nuclear burning at the peak of the flash, and eventually lead to mass loss of a star.

A major breakthrough in the research of the flash was achieved by [Thomas \(1967\)](#) and [Demarque & Mengel \(1971\)](#) who found that the ignition of helium during the flash can occur off-center due to neutrino losses ([Ramadurai 1976](#)). Calculations of the flash were redone later with better numerical techniques and an improved treatment of the major physical processes by [Sweigart & Gross \(1978\)](#). The ignition of helium occurred again off-center due to neutrino processes, but the general picture mentioned earlier remain unchanged.

Based on the core helium flash, [Paczynski & Tremaine \(1977\)](#) attempted to explain peculiar carbon abundances observed in some stars. They assumed the mass fraction at which helium ignites to be a free parameter as at that time the neutrino cooling rate was only poorly known ([Ramadurai 1976](#)). Indeed, from their simulations of a  $0.8 M_{\odot}$  star with helium ignition at the mass coordinate  $M_r \sim 0.4 M_{\odot}$ , they got a significant surface carbon increase. Nowadays, the neutrino production is very well understood, and their approach is no longer adequate.

At very low metallicity, the helium ignites further out from the center in low-mass stars. This fact leads to interesting phenomena in metal-poor stars due to hydrogen entrainment in the helium core during the flash ([Fujimoto et al. 1990](#); [Schlattl et al. 2001](#)). Under certain circumstances, such a flash results in an enrichment of the stellar surface by elements produced during helium burning and can explain observations of metal-poor, but carbon-rich stars.

### 1.1.2. Hydrodynamic Calculations

The conceptual problems associated with the helium core flash arise from the extremely short timescales involved in the event. While the pre-flash evolution proceeds on a nuclear timescale of  $\sim 10^8$  yrs, typical e-folding times for the energy release from helium burning can become as short as hours at the peak of the flash. These short times are comparable to convective turnover times, *i.e.* the common assumptions used for the treatment of convection in stellar evolution codes (instantaneous mixing, time-independence) are no longer valid. In addition, the assumption of hydrostatic equilibrium no longer needs to be fulfilled. Early attempts to avoid these assumptions by modeling one-dimensional hydrodynamic flow ([Edwards 1969](#); [Zimmermann 1970](#); [Villere 1976](#); [Wickett 1977](#)) remained inconclusive. The results ranged from a confirmation of the general scenario to a complete disruption of the star.

[Cole & Deupree \(1980, 1981\)](#) performed a two-dimensional hydrodynamic study of the core helium flash. However, their study was limited by the computational resources available at that time to a rather coarse computational grid ( $23 \times 4$  zones), a diffusive first-order difference scheme (weighted donor cell), and a short time evolution ( $10^5$  s compared to the duration of the core helium flash of  $10^{11}$  s from the onset of convection). At the radius of the off-center temperature maximum, they observed a series of thermonuclear runaways where heat transport by convection and conduction was sufficiently efficient to limit the rise in temperature. Each runaway modified the convective flow pattern and generated some inward transport of heat across the off-center temperature inversion. During the simulation, the time interval between runaways continuously shortened, and the maximum temperature steadily increased until it eventually exceeded  $10^9$  K.

[Deupree & Cole \(1983\)](#) and ([Deupree 1984a,b](#)) confirmed these findings using two-dimensional models with an improved angular resolution ( $6^\circ$  instead of  $20^\circ$ ), and three-dimensional simulations (with  $8 \times 8$  angular zones in a  $80^\circ \times 80^\circ$  cone, *i.e.*  $10^\circ$  angular resolution). [Cole et al. \(1985\)](#) performed stellar evolution calculations of the core helium flash using a model for convective

overshooting based on these hydrodynamic simulations. They found that the evolution of the core helium flash was unchanged except for the last week prior to its peak. Furthermore, the possibility of the mixing of core material into the hydrogen shell was suggested by numerical experiments where point source explosions were enforced (Deupree 1984b, 1986; Deupree & Wallace 1987). These results raised the hope that some problems concerning abundance anomalies and mass loss could be solved by understanding the core helium flash.

The results of the hydrodynamic simulations, though varying in details, indicated a dynamic flash that could disrupt the star (Deupree 1984a) or at least lead to a significant loss of the envelope (Cole & Deupree 1981). The simulations were criticized by Iben & Renzini (1984) and Fujimoto et al. (1990) because (i) the radial grid was too coarse, (ii) the gravitational potential was “frozen in” (*i.e.* time-independent), and (iii) because a “closed” outer boundary was used. The last two assumptions tend to underestimate the expansion of the core, and hence overestimate the violence of the flash.

## 1.2. Aims

Since the work of Deupree and Cole (see Sect. 1.1.2), the computational capabilities have grown tremendously and methods to simulate hydrodynamic flow have improved considerably. Thus, the limitations of the early studies concerning the grid resolution and the numerical treatment, which were the main points of critique, meanwhile can be reduced considerably. At the same time, we still have no coherent picture up to what extent and under what circumstances (stellar mass and composition) hydrodynamic core helium flash evolution could differ from canonical stellar evolution calculations. It therefore appears necessary to have a new and fresh look into the dynamics of the core helium flash. Deupree (1996) re-examined himself the problem already more than a decade ago concluding that the flash does not lead to any hydrodynamic event. Quiescent behavior of the core helium flash is also favored by recent three-dimensional simulations (Dearborn et al. 2006; Lattanzio et al. 2006) where the energy transport due to convection, heat conduction, and radiation seems to be always able to transport most of the energy generated during the flash quiescently from the stellar interior to the outer stellar layers, implying no hydrodynamic event, and hence a quasi-hydrostatic evolution.

In the following we will present an investigation of the core helium flash mainly by means of two- and three-dimensional hydrodynamic simulation using state-of-the-art numerical techniques, a detailed equation of state and time-dependent gravitational potential. Using a modified version of the Herakles code (Kifonidis et al. 2003, 2006; Mocák et al. 2008) which is now capable of solving the hydrodynamic equations coupled to nuclear burning and thermal transport in up to three spatial dimensions, we want to deepen our understanding of the flash. Its hydrodynamic evolution in multi-dimensions will provide us with information on the structure and topology of turbulent convection and on the entrainment into convectively stable layers which can give us hints where the one-dimensional canonical calculations may fail. One of our goals is a comparison of two- and three-dimensional hydrodynamic simulations versus predictions made by the mixing length theory (Vitense 1953; Böhm-Vitense 1958), typically adopted for a description of convection in canonical hydrostatic stellar evolutionary calculations.

Few studies of mixing length theory and multi-dimensional hydrodynamic simulations of turbulent convection with nuclear burning deep within a star were performed already (Bazan & Arnett 1998; Kercek et al. 1998, 1999; Asida & Arnett 2000; Herwig et al. 2006; Meakin & Arnett 2006; Dearborn et al. 2006; Arnett et al. 2007; Meakin & Arnett 2007b). This work is inspired by these studies in many aspects.

The thesis is organized as follows. In Sect. 2 we discuss characteristic properties of a helium core at the peak of the flash. In Sect. 3 we describe the input physics for our calculations. Our hydrodynamic code is described briefly in Sect. 4. In Sect. 5, we introduce the stellar models used as input for the calculations. Section 6 deals with one-dimensional hydrodynamic simulations. Section 7 gives a detailed analysis of our two-dimensional simulations. Three-dimensional simulations and the results from a comparison between three-dimensional simulation and two-dimensional simulations with the same angular resolution are discussed in Sect. 8. Finally, a summary is given in Sect. 9.

We note, that the present investigation was instigated by a similar, meanwhile technically obsolete study that was performed by Kurt Achatz ([Achatz 1995](#)) in the context of his diploma thesis. The results of this study have unfortunately never been published.



# 2

## Properties of the System

### 2.1. Regime

Almost 100 % of the stellar core during the core helium flash is composed of helium gas which is completely ionized. For helium particles, the ratio of the binding energy of the innermost electrons  $E_B \sim 24.7 \text{ eV}$  to their microscopic thermal energy is in the whole core very small,

$$\frac{E_B}{k_B T} < 0.01 , \quad (2.1)$$

where  $k_B$  is Boltzmann constant, and  $T$  is the temperature ( $1 \times 10^6 \text{ K} < T < 2 \times 10^8 \text{ K}$ ). The electron density in the core is so high that the gas is partially degenerate. The degeneracy parameter  $\psi$ <sup>1</sup>, in the center of the helium core during the flash at its peak under the convection zone powered by the helium burning is usually greater than 20, but in the convection zone the degeneracy is due to the strong expansion already significantly lifted, and  $\psi < 4$ .

On the other side, the ions can be described as an ideal and non-relativistic Boltzmann gas as the ratio of their Fermi energy  $E_{F,I} \sim 2.24 \times 10^{-12} \text{ erg}$  and the typical thermal energy of ions is small,

$$\frac{E_{F,I}}{k_B T} < 0.01 \quad (2.2)$$

The influence of the Coulomb forces between ions is negligible.

$$\Gamma = \frac{Z^2 e^2 / a}{k_B T} < 1 \quad \text{with} \quad a = \left( \frac{3}{4\pi n_I} \right)^{1/3} \quad (2.3)$$

where  $Z$  is the proton number,  $e$  is the electron charge,  $n_I$  is a number of particles per volume unit ( $\sim 1.5 \times 10^{28} \text{ cm}^{-3}$ ), and  $a$  is the mean distance between the charges.

---

<sup>1</sup>It can be shown that the gas pressure is essentially that of a nondegenerate gas for  $\psi < -2$  (Clayton 1968).

## 2.2. Convection and Turbulence

The helium core in a star near the peak of the core helium flash contains a convection zone (Fig. 1.2). Convection in stars is a dynamic process where gas currents transport energy and mix chemical elements. It appears in regions where small fluctuations in *e.g.* temperature may grow and give rise to macroscopic non-spherical motions. Imagine an initial temperature fluctuation as an element of gas with a temperature  $T$  which is higher than that of the surrounding gas *i.e.* its temperature is higher by  $\delta T > 0$ . In a convection region, the element feels a buoyant force and rises upwards until it cools down sufficiently enough so that gravity can stop the motion and pull it back to its original position. The condition for the existence of convection can be expressed using temperature gradients  $\nabla$  in the following way (Kippenhahn & Weigert 1990; Weiss et al. 2004):

$$\nabla_{\text{surr}} > \nabla_{\text{ele}} + \frac{\varphi}{\delta} \left( \frac{d \ln \mu}{d \ln P} \right)_{\text{surr}} \quad \text{with} \quad \nabla \equiv \frac{d \ln T}{d \ln P} \quad (2.4)$$

where the subscript “surr” refers to the surrounding of the element “ele”;  $\delta \equiv \partial \ln \rho / \partial \ln T$ , and  $\varphi \equiv \partial \ln \rho / \partial \ln \mu$ . The quantities  $P$ ,  $\rho$  and  $\mu$  are the pressure, density and mean molecular weight of the gas, respectively. Assuming the simplified case when the chemical gradient is zero, the condition means that the temperature of the rising element must be dropping slower than the temperature of the surrounding, *i.e.* the element remains less dense than its environment on its path, *i.e.* buoyancy can pull it upwards (Fig. 2.1). When we assume that the element does not exchange energy with its surrounding,  $\nabla_{\text{ele}}$  becomes equal to the adiabatic temperature gradient  $\nabla_{\text{ad}}$  and we get the Schwarzschild criterion, commonly used in canonical stellar evolutionary calculations. In reality, there is always a small exchange of energy between the hotter element and its environment, and therefore  $\nabla_{\text{ele}} > \nabla_{\text{ad}}$ .

In a case, when heavier elements in a star are located under the lighter ones, the chemical gradient  $\nabla_{\mu}$  increases inwards (as the pressure does) and  $\nabla_{\mu} > 0$  ( $\varphi$  and  $\delta$  are both positive). Then, the last term in Eq. 2.4 has a stabilizing effect. This is plausible as the element carries its heavier material upwards into a lighter surrounding.

$\nabla_{\text{surr}}$  is usually positive as both pressure and temperature are decreasing with increasing radius of star. However, at the position of the temperature inversion, that we have in the helium core during the core helium flash,  $\nabla_{\text{surr}}$  becomes negative and the criterion Eq. 2.4 does not hold. Therefore, the temperature inversion acts as an impenetrable reflective mirror for the convective motion.

The most popular theory in stellar evolution that describes transport of energy and mixing due to the convection is the mixing-length theory (Vitense 1953; Böhm-Vitense 1958; Kippenhahn & Weigert 1990; Weiss et al. 2004). The theory assumes that convection consists of blobs that travel over a certain distance, the mixing length  $\lambda$ , before they dissolve into the surrounding gas. Let's consider a convective element or blob with an excess temperature  $\delta T$  over its surrounding gas which is in pressure equilibrium with the ambient gas and rising vertically with a velocity  $v_{\text{MLT}}$  (Fig. 2.1). According to mixing-length theory, the flux of energy transported by the blobs in a convectively unstable region, *i.e.* the convective energy flux  $F_{\text{con}}$ , is given by

$$F_{\text{con}} = \rho v_{\text{MLT}} c_p \delta T, \quad (2.5)$$

where  $\rho$  and  $c_p$  are the density and the heat capacity at constant pressure of the gas, respectively.

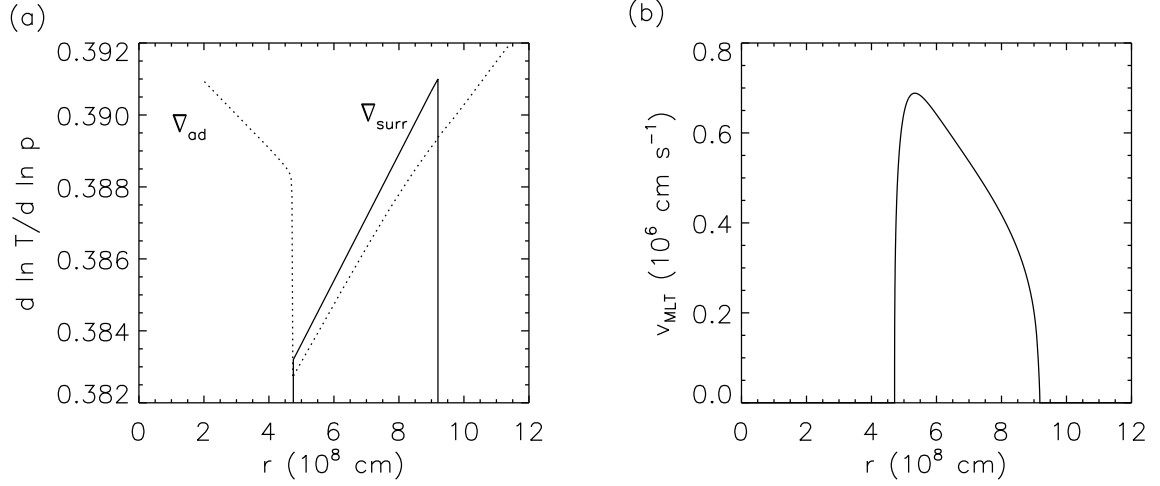


**Figure 2.1.:** (a) The adiabatic temperature gradient  $\nabla_{\text{ad}}$  (dotted) and an actual temperature gradient  $\nabla_{\text{surr}}$  (solid) in a  $1.25 M_{\odot}$  star with a metallicity  $Z=0.02$  at the peak of the core helium flash. The gradient  $\nabla_{\text{surr}}$  exceeds the value of the adiabatic gradient and therefore this region is convectively unstable. (b) Convective velocities  $v_{\text{MLT}}$  in the convectively unstable region within the helium core predicted by the mixing length theory.

The temperature excess  $\delta T$  is determined by the mixing length  $\lambda$ :

$$\frac{\delta T}{T} = (\nabla_{\text{surr}} - \nabla_{\text{ad}}) \frac{1}{H_p} \frac{\lambda}{2}, \quad (2.6)$$

where  $H_p = |p/\partial_r p|$  is the pressure scale height ( $\partial_r = \partial/\partial r$  is a partial derivative with respect to the radius  $r$ ). The mixing length  $\lambda$  is a free parameter. In addition, the theory is a local one, and therefore fails to capture genuine properties of convection which is a non-local phenomenon.

In a convectively stable region, any displaced mass element is pushed back by the buoyancy force. On its way back to its original position, the blob gains momentum and therefore starts to oscillate<sup>2</sup> at around its original position. Assuming, the element is displaced by a distant  $\Delta r$ , has an excess density  $\Delta \rho$  and is in its pressure equilibrium with the surrounding gas ( $\Delta P = 0$ ), one can derive an equation for an acceleration of the element:

$$\frac{\partial^2(\Delta r)}{\partial t^2} = \frac{g\delta}{H_p} \left[ \nabla_{\text{ele}} - \nabla_{\text{surr}} + \frac{\varphi}{\delta} \nabla_{\mu} \right] \Delta r, \quad \text{with} \quad \nabla_{\mu} = \frac{d \ln \mu}{d \ln P}, \quad (2.7)$$

where  $g$  is the gravitational acceleration. Let us assume now that the element, after an initial displacement  $\Delta r_0$ , moves adiabatically ( $\nabla_{\text{ele}} = \nabla_{\text{ad}}$ ) through a convectively stable layer. The element is accelerated back towards its equilibrium position around which it oscillates according to the solution of Eq. 2.7:

$$\Delta r = \Delta r_0 e^{i \omega_{\text{ad}} t} \quad (2.8)$$

The frequency  $\omega_{\text{ad}}$  of this adiabatic oscillations is called Brunt-Väisälä frequency, and is given by

<sup>2</sup>These oscillations are called internal gravity waves (Dalsgaard 2003).

$$\omega_{\text{ad}}^2 = \frac{g\delta}{H_P} \left( \nabla_{\text{ad}} - \nabla_{\text{surr}} + \frac{\varphi}{\delta} \nabla_{\mu} \right) \quad (2.9)$$

The corresponding period is  $\tau_{\text{ad}} = 2\pi/\omega_{\text{ad}}$ . In a convectively unstable region (assuming  $\nabla_{\mu} = 0$ ) Eq. 2.9 gives  $\omega_{\text{ad}}^2 < 0$ , *i.e.*  $\omega_{\text{ad}}$  is imaginary. Thus, the displaced element moves exponentially away from its initial position, instead of oscillating around it.

Nevertheless, the convective motions can also significantly influence regions which are convectively stable according to criterion Eq. 2.4. When a blob hits the boundary between the convectively stable and unstable layers with a sufficiently high momentum, it can overshoot into the stable region leading to additional heat transport and mixing within stars. This is a very common phenomenon in geophysical flows (Fernando 1991). Therefore, there is no reason to believe that it does not occur also in stratified media within stars.

Convection is a form of turbulence, which can be described by the dimensionless Rayleigh number (Landau & Lifshitz 1966), that measures the relative importance of buoyancy and frictional forces, and that also takes into account the effects of heat transport:

$$R_a = \frac{g\alpha c_p \rho^2 |\Delta T| d^3}{K\eta} \quad \text{with} \quad \alpha = -\frac{1}{\rho} \frac{\partial \rho}{\partial T} \Big|_p \quad (2.10)$$

where  $c_p$  is the heat capacity at constant pressure  $p$ ,  $K$  is the thermal transport coefficient,  $\alpha$  is the isobaric expansion coefficient, and  $\eta$  is the viscosity of the gas. The quantities  $d$  and  $\Delta T$  describe the extent of the convection zone and the temperature difference across it. For typical values<sup>3</sup> we get for the convection zone of the helium core Rayleigh numbers  $R_a > 10^{33}$  *i.e.* the region is highly turbulent (Achatz 1995).

Turbulent motion is characterized by random spatial and temporal fluctuations, and by the dimensionless Reynold number  $R_e$  (Landau & Lifshitz 1966). When that number exceeds a certain critical value  $R_{\text{crit}}$ , small fluctuations in the flow are amplified, and the flow eventually becomes turbulent. The critical value of  $R_e$  depends on the exact flow configuration. In gases, the Reynolds number is very high due to their low viscosity. In the convection zone during the flash

$$R_e \sim \frac{v \cdot l \cdot \rho}{\eta} \sim 10^{14} \quad (2.11)$$

where  $l$  and  $v$  are the characteristic length and velocity of the flow, respectively. This confirms our previous statement based on the estimate of the Rayleigh number, that the flow in the convection is turbulent, which leads to complications when trying to simulate this event. Turbulence is a three-dimensional phenomenon involving a large range of dynamical scales. We recall that, in three-dimensional turbulent flow, large structures are unstable and cascade into smaller vortices (as, *e.g.* in smoke plumes from chimneys) down to molecular scales where the kinetic energy of the flow is eventually dissipated into heat.

If  $L$  is the largest scale characterizing a flow and  $l$  the scale where viscous dissipation begins, one has the well known relation:

---

<sup>3</sup>An estimate of  $\eta$  for strongly degenerate and completely ionized helium gas comes from the calculations of Itoh et al. (1987) that imply a value of  $\eta < 4 \times 10^5 \text{ g cm}^{-1} \text{ s}^{-1}$ .

$$\frac{L}{l} \sim R_e^{3/4} \quad (2.12)$$

For example, in the Sun where the Reynolds number  $R_e$  is typically  $10^{12}$ , one obtains  $L/l \sim 10^9$  *i.e.* the dissipation length scale is a billion times smaller than the largest length scale. Therefore, the number of grid points  $N$  that a numerical simulation would require to resolve all the relevant length scales is  $N \sim (\frac{L}{l})^3 \sim R_e^{9/4} \sim 10^{27}$  which is 17 orders of magnitude larger than  $N \sim 10^{10}$ ; the largest resolution computers can handle today (Canuto 2000). To account for turbulence on the numerically unresolved scales, one usually adopts sub-grid scale models *e.g.* by Smagorinsky (1963) which describe the energy transfer from the smallest numerically resolved turbulent elements to those at the dissipation length scale, using various model and flow dependent parameters.

### 2.3. Important Time Scales

A major disadvantage of multidimensional hydrodynamic simulations of stars today is related to the fact, that stars evolve on a nuclear timescale which is typically of the order of  $10^9$  years. But, even with the best supercomputers nowadays, we are not able to cover more than a few days of stellar evolution (Herwig et al. 2006; Meakin & Arnett 2007b; Mocák et al. 2008).

Nevertheless, hydrodynamic simulations are an important tool for studying the evolution of stars. Let us first define three major timescales, which one can associate with nuclear burning and hydrodynamic flow.

- Nuclear timescale  $\tau_{brn}$ : An e-folding time,  $\tau_{brn} = T/\dot{T} \approx c_V T/\dot{\epsilon}_{nuc}$ , where  $\dot{\epsilon}_{nuc}$  is the energy release rate of the nuclear processes,  $T$  is the temperature, and  $c_V$  is the specific heat.
- Sound crossing timescale  $\tau_{hyd}$ : A time, during which a region of a radius  $\delta r$  reacts to any pressure imbalance. Such a reaction occurs with the local sound speed  $c_s$  and therefore the sound crossing time scale is  $\tau_{hyd} = \delta r/c_s$ .
- Convective turnover timescale  $\tau_{cnv}$ : A time, which a convective element needs to cross the convection zone of width  $R_{cnv}$  with a velocity  $v_{cnv}$ , *i.e.*,  $\tau_{cnv} = R_{cnv}/v_{cnv}$ .

When the convective turnover timescale  $\tau_{cnv}$  in a stellar convection zone becomes comparable or smaller than the nuclear burning timescale  $\tau_{brn}$ , the border between quiescent quasi-hydrostatic evolution and an explosion of a star is narrow (an issue which caused a lot of confusion in the past; see Sect. 1.1.2). At this stage convection is losing its ability to transport as much energy as it is produced by nuclear reactions, and the convective layers begin to expand rapidly. Whenever such a situation occurs in stellar evolution, the convective flow should be studied by hydrodynamic simulations, as they are able to correctly follow the reaction of the flow to any pressure imbalance occurring on the sound crossing timescales  $\tau_{hyd}$ .

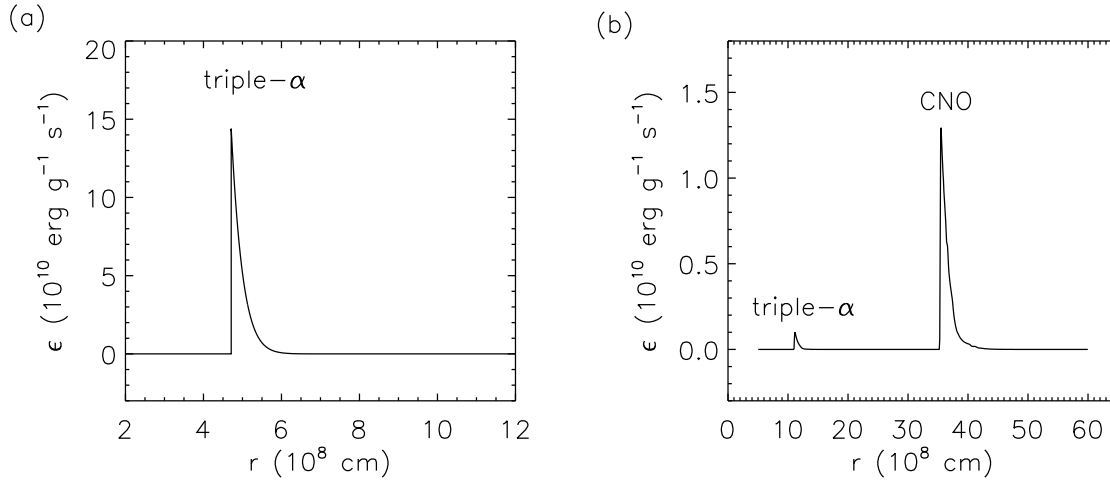
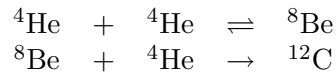


**Figure 2.2.:** Radial profile of the energy generation rate in a  $1.25 M_{\odot}$  star with a metallicity  $Z=0.02$  (a) and a metal-free ( $Z=0$ )  $0.85 M_{\odot}$  star (b) during the core helium flash. In the latter case the energy production rate by the CNO cycle exceeds the energy production rate by triple- $\alpha$  reaction.

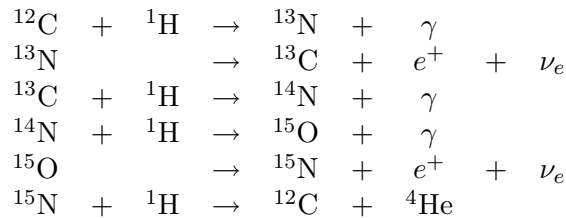
## 2.4. Thermonuclear Reactions

The dominant energy source in stars undergoing the core helium flash is the triple- $\alpha$  reaction (Fig. 2.2) where three  ${}^4\text{He}$  nuclei are fused into one  ${}^{12}\text{C}$  nucleus through the following nuclear chain including the unstable  ${}^8\text{Be}$ <sup>4</sup>:



The reaction rate of these processes  $\langle\sigma v\rangle$ , which is a product of the cross section and the velocity of particles, averaged over distribution of kinetic energy of particles, is extremely sensitive to the temperature of the gas  $\langle\sigma v\rangle_{3\alpha} \propto T^{20..40}$ . Thus, temperature fluctuations may play an important role during the core helium flash.

The situation is different for the extremely metal-poor stars which can experience entrainment of hydrogen into the helium burning regions *i.e.* consequently, the dominant energy source is provided by the CNO cycle:



Although, energy generation rate by the triple- $\alpha$  reaction is still relatively high at the peak of the flash in the metal-poor stars, it is by an order of magnitude smaller than that provided by the CNO cycle (Fig. 2.2).

<sup>4</sup>The unstable nucleus  ${}^8\text{Be}$  decays in  $\sim 10^{-6}$  s

If the gas density is high, the reaction rates of the nuclear processes are influenced by the Coulomb interaction of the charged particles. The charged particles can shield the nuclei and therefore influence their Coulomb potential and lead to an enhancement of the reaction rate. This effect is called screening and can be described by a screening factor  $f$  which depends on the density and the temperature of the gas (see Sect. 4.3).

## 2.5. Neutrinos

Neutrinos  $\nu$  and antineutrinos  $\bar{\nu}$  created in the helium core during the flash leave the star unaffected. They carry energy away from the star, and are responsible for the central temperature inversion and the off-center ignition of the helium at the onset of the core helium flash (Thomas 1967; Demarque & Mengel 1971; Ramadurai 1976). There exist three dominant  $\nu$  processes in stellar interiors (Inman & Ruderman 1964; Reeves 1963):

- Plasma Neutrino Process:  $\text{plasmon} \rightarrow \nu + \bar{\nu}$ . Plasmons are electromagnetic waves in a plasma possessing an excess of energy for a given momentum, which results from the interaction of the photons with the plasma. They are energetically unstable against neutrino-decay mode, whereas a free photon is stable (Clayton 1968).
- Photo Neutrinos Process:  $\gamma + e^- \rightarrow e^- + \nu + \bar{\nu}$ . A photon is converted into a neutrino-antineutrino pair by scattering off an electron. This is a modified form of Compton scattering (Beaudet et al. 1967).
- Pair-Annihilation Process:  $e^+ + e^- \rightarrow \nu + \bar{\nu}$ . Annihilation of electron-positron pairs can lead to the production of neutrino, antineutrino pair instead of the production of two photons. This process is interesting at higher temperatures where the amount of electron-positron pairs increases.

The plasma neutrino process is the most important energy loss during the core helium flash (Ramadurai 1976).

## 2.6. Thermal Transport

We can imagine a thermal transport as a process, which leads to a transfer of heat by radiative and conductive processes, *i.e.* particle collisions (electrons and ions). The energy flux density due to thermal transport  $f_{TH}$  can be expressed in the following form:

$$f_{TH} = -K_{TH} \nabla T = -(K_\gamma + K_{e,i}) \nabla T \propto \frac{1}{\kappa_\gamma} + \frac{1}{\kappa_{e,i}} \propto \frac{1}{\kappa}, \quad (2.13)$$

where  $K_{TH}$  is the total thermal conductivity (in  $\text{erg K}^{-1} \text{cm}^{-1} \text{s}^{-1}$ ). It is the sum of the thermal conductivity due to photons  $K_\gamma$  and particle collisions  $K_{e,i}$ , respectively. The corresponding opacities are  $\kappa_\gamma$  and  $\kappa_{e,i}$  (in  $\text{cm}^2 \text{s}^{-1}$ ), respectively.  $\nabla T$  is the local temperature gradient. There exists a relation between the conductivity  $K$ , velocity  $v$ , and the mean free path of particles  $\lambda$ :

$$K_{\gamma,e,i} \propto v_{\gamma,e,i} \cdot \lambda_{\gamma,e,i}. \quad (2.14)$$

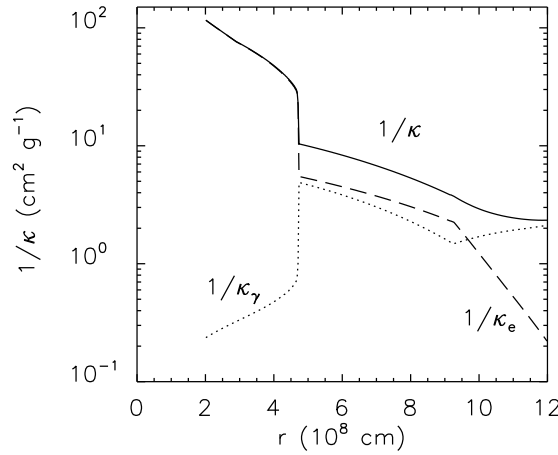


**Figure 2.3.:** Radial profiles of the inverse opacities due to radiation  $1/\kappa_\gamma$  (dotted) and electrons  $1/\kappa_e$  (dashed), respectively, and of the inverse of the total opacity *i.e.*  $1/\kappa = 1/\kappa_\gamma + 1/\kappa_e$  (solid) in the helium core of a  $1.25 M_\odot$  star with a metallicity  $Z=0.02$  during the core helium flash at its peak.

It tells us that in non-degenerate matter, the transport due to radiation dominates, as the speed  $v_\gamma$  and the mean free path  $\lambda_\gamma$  of photons are much higher than those of massive particles in the gas. The situation is different in electron degenerate matter where the electrons can have very high velocities and their collisions become rather unlikely leading to an increase of their mean free path  $\lambda_e$ . Therefore, in this regime, the radiative opacity  $\kappa_\gamma$  exceeds the value of  $\kappa_e$  considerably, *i.e.* thermal transport due to electron conduction dominates the thermal transport.

In the helium core at the peak of the flash one encounters both regimes (Fig. 2.3). The electron degeneracy is almost completely lifted at the top of the helium core and heat conduction due to electrons is small. On the other hand, the center of the helium core is still highly degenerate. Therefore, we need to take both contributions into account in our calculations.

## 2.7. Geometry

The computational grid for the hydrodynamic simulations of the core helium flash must contain the whole convection zone as the typical length scales of convective motions are roughly comparable to the width of the convection zone. As we simulate only a fraction of a star, which is a sphere, to simplify calculations at boundaries of the computational grid, it is appropriate to perform the simulations in spherical polar coordinates  $(r, \theta, \phi)$  where  $r$  is the radius,  $\theta \in [0^\circ, 180^\circ]$  the polar angle, and  $\phi \in [0^\circ, 360^\circ]$  the azimuthal angle.



# 3

## Input Physics

### 3.1. Evolutionary Equations

The hydrodynamic and thermonuclear evolution of the core helium flash was computed by solving the governing set of fluid dynamic equations in spherical coordinates on an Eulerian grid. Using vector notation, these equations have the form,

$$\frac{\partial \mathbf{U}}{\partial t} + \nabla \mathbf{F} = \mathbf{S} \quad (3.1)$$

with the state vector  $\mathbf{U}$

$$\mathbf{U} \equiv \begin{pmatrix} \rho \\ \rho \mathbf{v} \\ \rho e \\ \rho X_i \end{pmatrix} \quad (3.2)$$

the flux vector  $\mathbf{F}$

$$\mathbf{F} \equiv \begin{pmatrix} \rho \mathbf{v} \\ \rho \mathbf{v} \mathbf{v} \\ (\rho e + p) \mathbf{v} + f_{cond} \\ \rho X_i \mathbf{v} \end{pmatrix} \quad (3.3)$$

and the source vector  $\mathbf{S}$

$$\mathbf{S} \equiv \begin{pmatrix} 0 \\ -\rho \nabla \Phi \\ -\rho \mathbf{v} \cdot \nabla \Phi + \rho \dot{\epsilon}_{nuc} \\ \rho \dot{X}_i \end{pmatrix} \quad (3.4)$$

with  $i = 1, \dots, N_{\text{nuc}}$ , where  $N_{\text{nuc}}$  is the number of nuclear species considered in the nuclear reaction network, and  $\rho$ ,  $p$ ,  $\mathbf{v}$ , and  $\Phi$  are the density, pressure, velocity, and gravitational potential, respectively. The term  $f_{\text{cond}}$  describes energy transport by thermal conduction (see Sect. 3.5), and  $\dot{\epsilon}_{\text{nuc}}$  and the  $\dot{X}_i$  are the nuclear energy generation rate and the change in the mass fraction of species  $i$  due to nuclear reactions, respectively (see Sect. 3.3). The total energy density  $\rho e = \rho \varepsilon + \rho \mathbf{v} \mathbf{v} / 2$ , where  $e$  is the specific total energy and  $\varepsilon$  is the specific internal energy.

### 3.2. Equation of State

The equation of state employed in our hydrodynamic code includes contributions due to radiation, ions, electrons, and positrons. The total pressure and energy density is therefore given by

$$\begin{aligned} P &= P_\gamma + P_{\text{ion}} + P_e + P_p \\ \rho e &= E_\gamma + E_{\text{ion}} + E_e + E_p \end{aligned} \quad (3.5)$$

where

$$\begin{aligned} P_\gamma &= \frac{a}{3} T^4 \\ E_\gamma &= \frac{3}{\rho} P_{\text{rad}} \end{aligned}$$

is the radiation pressure and energy density of a photon gas of temperature  $T$ ,  $a$  is the universal radiation constant,

$$\begin{aligned} P_{\text{ion}} &= \sum_i \Re \frac{\rho X_i}{A_i} T = \Re \rho T \sum_i Y_i \\ E_{\text{ion}} &= \frac{3}{2} \Re \rho T \sum_i Y_i = \frac{3}{2} \frac{P_{\text{ion}}}{\rho} \end{aligned}$$

is the pressure and energy density of a non-relativistic Boltzmann gas of density  $\rho$  which consists of a set of ions of abundance  $Y_i = X_i/A_i$  (where  $X_i$  and  $A_i$  are the mass fraction and the atomic mass number of species  $i$ , respectively).

The pressure of an arbitrarily degenerate and relativistic electron-positron gas  $P_e + P_p$  is based on table interpolation of the Helmholtz free energy (Timmes & Swesty 2000).

### 3.3. Nuclear Burning

The energy generation rate by nuclear burning is given by

$$\dot{\epsilon}_{\text{nuc}} = \sum_i \frac{\Delta m_i c^2}{m_u} \dot{Y}_i, \quad (3.6)$$

where

$$\Delta m_i = M_i - A_i m_u \quad (3.7)$$

is the mass excess of a nucleus of mass  $M_i$ , and  $m_u$  is the atomic mass unit.

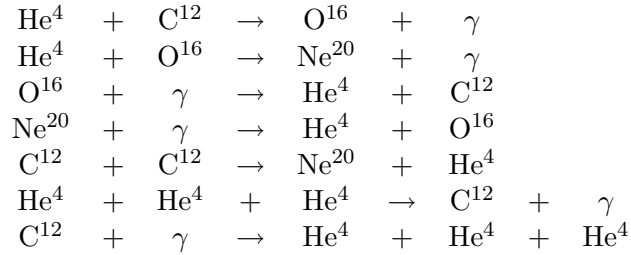
Abundance changes are described in our simulations by a nuclear reaction network consisting of the four  $\alpha$ -nuclei  ${}^4\text{He}$ ,  ${}^{12}\text{C}$ ,  ${}^{16}\text{O}$ , and  ${}^{20}\text{Ne}$ , coupled by seven reactions (including the triple- $\alpha$  reaction). We used the reaction rate library of Thielemann (private communication), which provides the product of the Avogadro number  $N_A$  and the velocity averaged cross section  $\langle\sigma v\rangle$  in terms of the fit formula

$$N_A\langle\sigma v\rangle = \sum_{l=1}^{n_l} \exp \left[ c_{1l} + c_{2l}T^{-1} + c_{3l}T^{-1/3} + c_{4l}T^{1/3} + c_{5l}T + c_{6l}T^{5/3} + c_{7l}\ln T \right], \quad (3.8)$$

with rate dependent coefficients  $c_{il}$  ( $1 \leq i \leq 7$ ). Up to three sets of coefficients (*i.e.*  $1 \leq n_l \leq 3$ ) are used. The total reaction rate due to all one-body, two-body, and three-body interactions has the form (Müller 1998):

$$\begin{aligned} \dot{Y}_i = & \sum_j c_i \lambda_j Y_j + \sum_{j,k} c_i(j,k) \rho N_A \langle\sigma v\rangle_{j,k} Y_j Y_k \\ & + \sum_{j,k,l} c_i(j,k,l) \rho^2 N_A^2 \langle\sigma v\rangle_{j,k,l} Y_j Y_k Y_l \end{aligned} \quad (3.9)$$

where the weight factors  $c_i$  prevent multiple counts in the sums. The following nuclear reactions were considered:

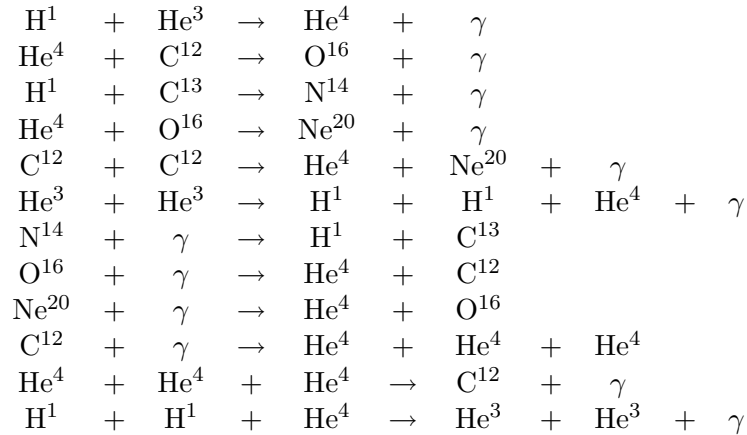


Mathematically, this produces a nuclear reaction network consisting of four non-linear first-order differential equations of the form given by Eq. (3.9) and a temperature equation

$$\frac{\partial T}{\partial t} = \dot{\varepsilon}_{nuc} \frac{\partial T}{\partial \varepsilon}, \quad (3.10)$$

where  $\varepsilon$  is the specific internal energy.

Abundance changes due to CNO-cycle are described in our simulations by a nuclear reaction network consisting of the eight nuclei, namely  ${}^1\text{H}$ ,  ${}^3\text{He}$ ,  ${}^4\text{He}$ ,  ${}^{12}\text{C}$ ,  ${}^{13}\text{C}$ ,  ${}^{14}\text{N}$ ,  ${}^{16}\text{O}$  and  ${}^{20}\text{Ne}$ , coupled by the following twelve reactions:



In both networks, the effects of electron screening were included according to [Dewitt et al. \(1973\)](#) for the triple- $\alpha$  reaction rate.

### 3.4. Neutrino Emission

The evolutionary time covered by our hydrodynamic simulations is too short for neutrino cooling to be of importance. The neutrino losses computed from the analytic fits of [Itoh et al. \(1996\)](#) provide a cooling rate  $\dot{\epsilon} < 10^2 \text{ erg g}^{-1} \text{ s}^{-1}$ , or a corresponding decrease in the maximum temperature by  $|\Delta T| < 10^{-1} \text{ K}$  during the longest simulations that we performed. Hence, cooling by neutrinos was neglected.

### 3.5. Thermal Transport

The energy flux density due to thermal transport is given by

$$f_{\text{cond}} = -K_{\text{cond}} \nabla T, \quad (3.11)$$

where  $K_{\text{cond}}$  is the total conductivity ( $\text{erg K}^{-1} \text{ cm}^{-1} \text{ s}^{-1}$ ) and  $\nabla T$  the temperature gradient.

In the helium core, which is partially degenerate, thermal transport due to both radiative diffusion and electron conduction is important, while heat transport by ions is negligible, *i.e.*

$$K_{\text{cond}} = K_{\gamma} + K_e. \quad (3.12)$$

The radiative conductivity is given by

$$K_{\gamma} = \frac{4ac}{3} \frac{T^3}{\kappa_{\gamma} \rho}, \quad (3.13)$$

where  $\kappa$ ,  $a$ , and  $c$  are the Rosseland mean of the opacity, the radiation constant, and the speed of light, respectively. For the opacity, we use a formula proposed by [Iben \(1975\)](#), which is based on the work of [Cox & Stewart \(1970a,b\)](#). It takes into account the radiative opacity due to Thomson scattering, free-free (Kramers opacity), bound-bound, and bound-free transitions (see *e.g.* [Weiss et al. \(2004\)](#)).

- Thomson scattering is a process where an electrodynamic wave interacts with a charged particle. The electric and magnetic components of the wave exert a Lorentz force on the particle and accelerate it, making the particle to oscillate. The oscillating particle then emits radiation *i.e.* the energy is absorbed from the incident wave by the particle and re-emitted as electromagnetic radiation in different direction. In case of the scattering of free electrons, the Thomson electron scattering opacity can be expressed as

$$\kappa_e = \sigma_0 n_e / \rho, \quad (3.14)$$

where  $\sigma_0 = (8\pi/3)(e^2/m_e c^2)$  is the Thomson scattering cross section;  $e$  and  $m_e$  is electron charge and mass, respectively.

- Free-free transitions result when a free electron passes an ion during its thermal motion. The system then absorbs and emits radiation. The free-free opacity

$$\kappa_{ff} \propto \frac{\rho}{T^{3.5}} \quad (3.15)$$

and is called Kramers opacity.

- Bound-bound transitions and bound-free transitions are very rare in the helium core since the gas is almost completely ionized. The opacity which could result from these transition is therefore negligible.

The total opacity is given by the sum of all contributions,  $\kappa_\gamma = \kappa_e + \kappa_{ff}$ , due to interaction of photons with particles.

For the thermal transport by electron conduction, we consider contributions due to electron-ion and electron-electron collisions. The thermal conductivity  $K_e$  of degenerate electrons in a gas is described in detail in work by [Yakovlev & Urpin \(1980\)](#) and [Potekhin et al. \(1997\)](#).



# 4

## Code

The numerical simulations were performed with a modified version of the hydrodynamic code Herakles (Kifonidis et al. 2003, 2006), which is a descendant of the code Prometheus developed by Bruce Fryxell and Ewald Müller (Müller et al. 1991; Fryxell et al. 1991). The hydrodynamic equations were integrated to second order accuracy in space and time using the dimensional splitting approach of Strang (1968), the PPM reconstruction scheme (Colella & Woodward 1984), and a Riemann solver for real gases according to Colella & Glaz (1984). The evolution of the chemical species was described by a set of additional continuity equations (Plewa & Müller 1999). Source terms in the evolutionary equations due to self-gravity and nuclear burning were treated by means of operator splitting. Every source term was computed separately, and its effect was accounted for at the end of the integration step. The viscosity tensor was not taken into account explicitly, since the solution of the Euler equations with the PPM scheme corresponds to the use of a sub-grid scale model that reproduces the solution of the Navier-Stokes equations reasonably well (Sitine et al. 2000; Meakin & Arnett 2007b). Thermal transport was treated in a time-explicit fashion when integrating the evolutionary equations. Self-gravity was implemented according to Müller & Steinmetz (1995), while the gravitational potential was approximated by a one-dimensional Newtonian potential derived from the spherically averaged mass distribution. The nuclear network was solved with the semi-implicit Bader-Deuffhard method that utilizes the Richardson extrapolation approach and sub-stepping techniques (Bader & Deuffhard 1983; Press et al. 1992) allowing for long effective timesteps.

In Herakles, a program cycle for multi-dimensional simulations consists of two hydrodynamic timesteps and proceeds as follows:

1. The hydrodynamic equations are integrated in  $r$ -direction ( $r$ -sweep) including the effects of heat conduction. The time averaged gravitational forces are computed, and the momentum and the total energy are updated to account for the gravitational source terms. Subsequently, the equation of state is called to update the thermodynamic state due to the change of the total energy.
2. Step (1) are repeated in  $\theta$ -direction ( $\theta$ -sweep).
3. Step (1) are repeated in  $\phi$ -direction ( $\phi$ -sweep).

4. The nuclear network is solved in all zones with significant nuclear burning ( $T > 10^8 \text{K}$ ). Subsequently, the equation of state is called to update the pressure and the temperature.
5. In the subsequent timestep the order of Step (1), (2) and (3) is reversed to guarantee second-order accuracy of the time integration, and Step (4) is repeated with the updated quantities.
6. The size of the timestep for the next cycle is determined.

For one-dimensional simulations, Step (2),(3) and Step (5) are omitted. For two-dimensional simulation, Step (3) is omitted.

The two- and three-dimensional simulations had to be initially perturbed explicitly to trigger convection, because an initially exactly spherically symmetric model remains that way forever when evolved in spherical polar coordinates with our code. We imposed a random flow field with a maximum (absolute) velocity of  $10 \text{ cm s}^{-1}$ , and random density perturbations with  $\Delta\rho/\rho \leq 10^{-2}$ .

## 4.1. Hydrodynamics

The hydrodynamic equations (Eq. 3.1)<sup>1</sup> were integrated by the piecewise parabolic method (PPM) of Colella & Woodward (1984).

### 4.1.1. Piecewise Parabolic Method

Following Colella & Woodward (1984), we discuss the principles of PPM using the one-dimensional Euler equations in conservative form:

$$\frac{\partial \mathbf{U}}{\partial t} + \frac{\partial(A\mathbf{F})}{\partial V} + \frac{\partial \mathbf{H}}{\partial r} = 0 \quad (4.1)$$

where

$$\mathbf{U} = \begin{pmatrix} \rho \\ \rho u \\ \rho e \end{pmatrix} \quad \mathbf{F}(\mathbf{U}) = \begin{pmatrix} \rho u \\ \rho u^2 \\ \rho u e + u p \end{pmatrix} \quad \mathbf{H}(\mathbf{U}) = \begin{pmatrix} 0 \\ p \\ 0 \end{pmatrix} \quad (4.2)$$

$u$  is velocity,  $V(r) = r^{\alpha+1}/(\alpha+1)$  is a volume coordinate and  $A(r) = r^\alpha$ , where  $\alpha = 0,1,2$  depending on whether there is planar, cylindrical or spherical symmetry, respectively.

The scheme consist of the following major steps (Fig. 4.1):

1. We discretize the state variable  $\mathbf{U}$  on a numerical grid and assign to it a parabolic function  $\mathbf{a}(\zeta)$  which has the following properties:
  - Let  $\zeta_{j+1/2}$  be the boundary between the  $j$ th and the  $j+1$ st grid zone on the computational grid and assume that we know  $a_j^n$ , the average value of the solution between

---

<sup>1</sup>The complete set of hydrodynamical equations in the spherical coordinates is in the Appendix A.1



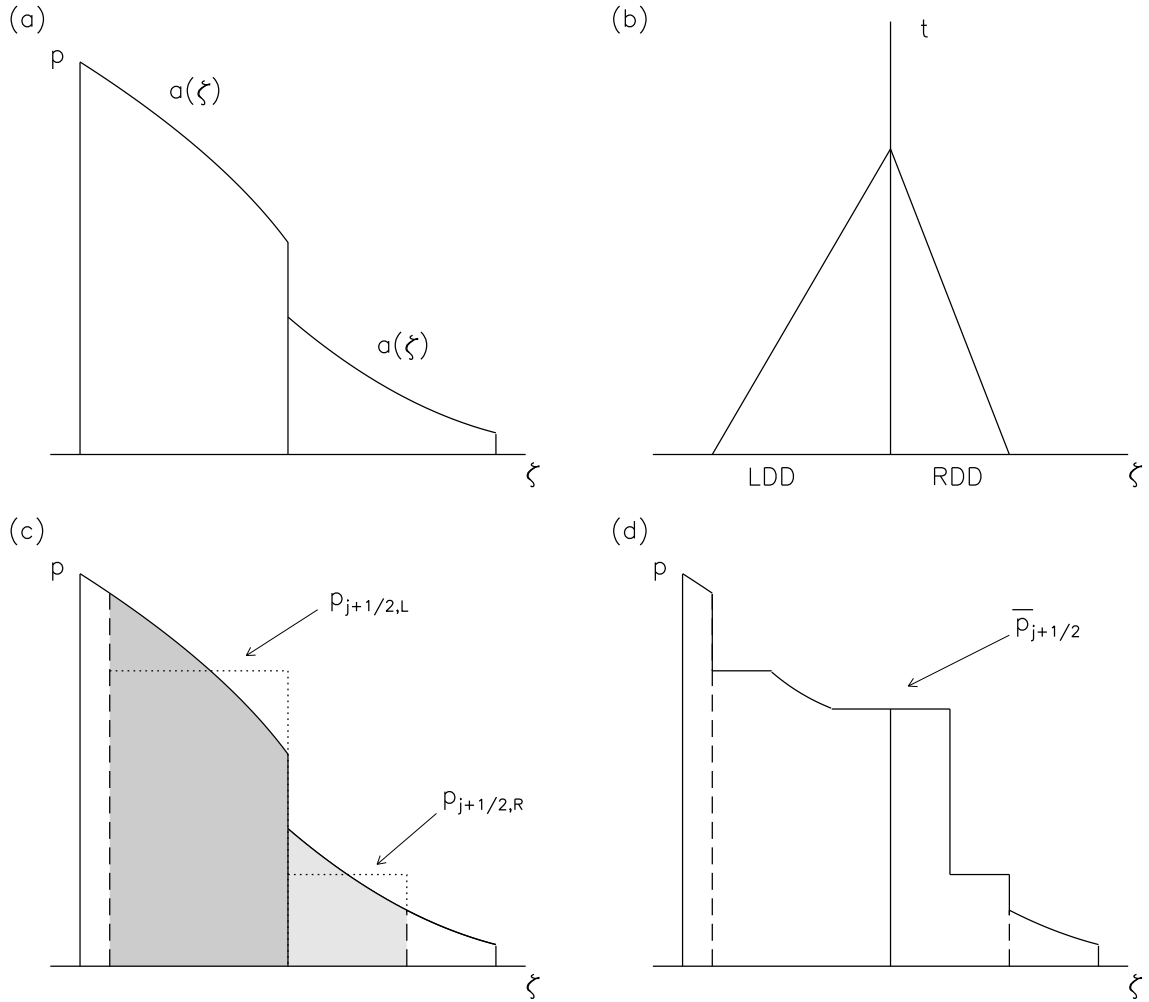


**Figure 4.1.:** Computation of numerical fluxes with PPM. (a) Piecewise parabolic reconstruction of initial data. (b) Left and right domain of dependence (LDD and RDD, respectively) for a given interface is computed by tracing back the characteristics which are the solid inclined lines (c) The interpolated distribution of each variable (*e.g.* pressure  $p$ ) within each domain of dependence is replaced by its averaged value ( $p_{j+1/2,L}$  and  $p_{j+1/2,R}$ ). (d) The interaction of the two averaged states adjacent to the interface is described by a solution of Riemann's shock tube problem indicated here. The nonlinear waves moving away from the interface reach the edges of the averaged domains at the end of the timestep. At the position of the interface we get the new effective value of  $\bar{p}_{j+1/2}$ .

$\zeta_{j+1/2}$  and  $\zeta_{j-1/2}$  at time  $t^n$ . The average of the parabolic function over a zone  $j$  at timestep  $t^n$  which we will call  $a_j^n(\zeta, t^n)$  has to be equal to

$$\frac{1}{\Delta\zeta_j} \int_{\zeta_{j-1/2}}^{\zeta_{j+1/2}} a(\zeta, t^n) d\zeta = a_j^n \quad (4.3)$$

where  $\Delta\zeta = \zeta_{j+1/2} - \zeta_{j-1/2}$ .

This shows, how PPM differs from traditional finite difference techniques. While the latter describe variable at discrete gridpoints, PPM uses zone averages  $a_j^n$  *i.e.* PPM belongs to the class of finite-volume methods.

- $\mathbf{a}(\zeta)$  is monotone within grid zones (*i.e.* no additional extrema appear there). In case that the zone contains a local extremum, the reconstructed function is set to be constant.
  - In case of smooth flow  $\mathbf{a}(\zeta)$  is continuous.
2. We determine the domain of dependence<sup>2</sup> for each zone interface for every timestep  $\Delta t = t^{n+1} - t^n$  by tracing the paths of sound waves (the characteristics) arriving at the interface at the end of the timestep.
  3. Then we determine, our effective left and right state  $\bar{\mathbf{U}}$  for the following solution of the Riemann problem at every zone interface, by averaging over the domain of dependence (predictor step).
  4. We solve a Riemann shock tube problem<sup>3</sup> according to [Colella & Glaz \(1984\)](#) and compute the numerical flux  $F_{i+1/2}$  and  $F_{i-1/2}$  at the zone interfaces.
  5. The solution at the next time level  $t^{n+1}$  is obtained by (corrector step):

$$\mathbf{U}_j^{n+1} = \mathbf{U}_j^n + \Delta t \left( \frac{A_{j-1/2} \mathbf{F}(\bar{\mathbf{U}}_{j-1/2}) - A_{j+1/2} \mathbf{F}(\bar{\mathbf{U}}_{j+1/2})}{\Delta V_j} + \frac{\mathbf{H}(\bar{\mathbf{U}}_{j-1/2}) - \mathbf{H}(\bar{\mathbf{U}}_{j+1/2})}{\Delta r_j} \right) \quad (4.4)$$

where  $A_{j+1/2} = A(r_{j+1/2})$

PPM involves the solution of Riemann problems which allows one to adequately treat the non-linear nature of the waves, *i.e.* it provides highly accurate numerical solutions that can involve shocks, discontinuities, or large gradients. The accuracy of the whole scheme is of 2nd order in space and time, and it possesses a small numerical diffusion. In the vicinity of sharp gradients, the scheme is only 1st order accurate. PPM is a numerical technique that was developed for modeling astrophysical fluid flows with shocks, and its validity in the subsonic flow regime, typical for stellar convection (*e.g.* during the core helium flash) with low Mach numbers ( $M \sim 0.01$ ), has been questioned. ([Schneider et al. 1999](#); [Tukel 1999](#); [Almgren et al. 2006](#)). However, a recent study by [Meakin & Arnett \(2007a\)](#) based on a direct comparison of anelastic ([Kuhlen et al. 2003](#)) and fully compressible simulations performed with PPM shows that at Mach numbers down to  $10^{-2}$ , PPM can capture the properties of convective flows well.

<sup>2</sup>An interval within the grid zone which is able to influence the solution at  $t^{n+1}$

<sup>3</sup>A Riemann problem is an initial value problem with piecewise constant initial conditions which resemble a situation in a tube with two containers filled with a gas of different properties (*e.g.* density, pressure etc.) separated by a membrane.

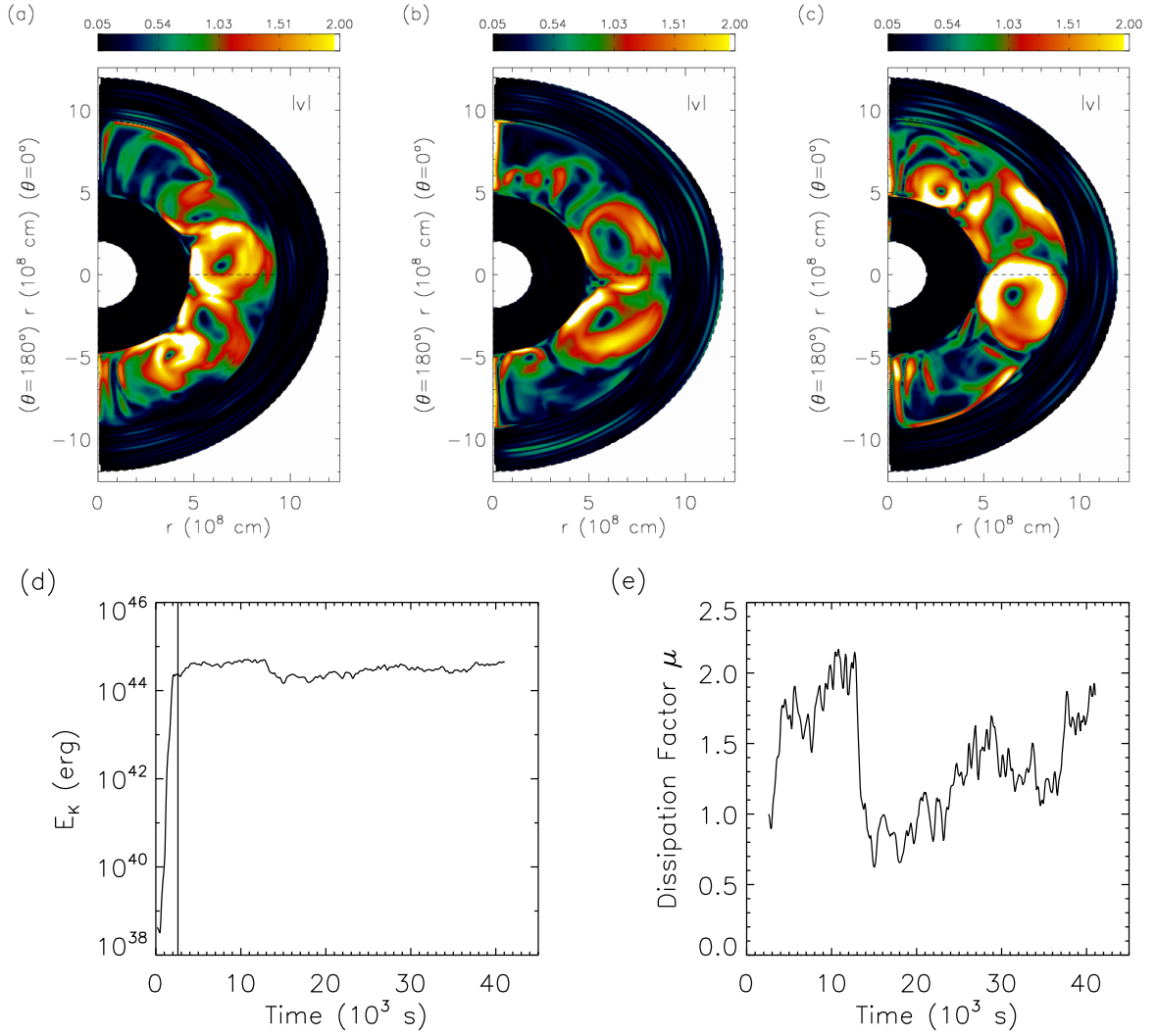


**Figure 4.2.:** *Upper panels:* Snapshots of the spatial distribution of the velocity modulus  $|v|$  (in units of  $10^6$  cm s $^{-1}$ ) from a two-dimensional simulation of the core helium flash not sustained by nuclear burning at 8000 s (a), 24400 s (b), and 40400 s (c), respectively. *Lower panels:* Temporal evolution of the total kinetic energy  $E_K$  (d), and the dissipation factor  $\mu$  (e). The vertical line denotes the reference time  $t_0$ .

It turns out, that numerical schemes like PPM can lead to fast artificial dissipation of kinetic energy in simulations of subsonic flows (Mach numbers  $< 0.1$ ) (Miczek 2008). As we expect the convective flow during the core helium flash to be subsonic ( $M \sim 0.01$ ), we studied how fast the kinetic energy is dissipated in hydrodynamic simulations of the convective flow in the helium core during the flash which is not sustained by nuclear burning (details of the corresponding simulation hefl.2d.2 where nuclear burning was included are given in Sect. 7). We define a dissipation factor for kinetic energy as  $\mu = E_{kin}(t_0)/E_{kin}(t)$ , where  $E_{kin}(t_0)$  and  $E_{kin}(t)$  are total kinetic energies at time  $t_0$  and at a later time  $t$ , respectively. Ideally, the dissipation factor should remain close to 1 throughout the flash simulation, as the convective flow will be partially supported by the hot bottom of the convection zone at the temperature maximum.

Figure 4.2 shows that the dissipation of kinetic energy is not serious. The total kinetic energy of the two-dimensional convective flow does not decrease rapidly, as the dissipation factor  $\mu$  stays close to or above 1. The typical vortex structure is visible even at  $t \sim 40400$  s, *i.e.* after roughly 30 convective turnover times (see Sect. 2.3).

### 4.1.2. Courant-Friedrich-Levy Condition

PPM is an explicit scheme which causes a limit on the size of the timestep for numerical stability. The timestep has to obey the Courant-Friedrich-Levy condition *i.e.* no information can spread over a larger distance than the size of a grid cell within one timestep

$$\Delta t \leq \Delta t_{CFL} = \min_k \left\{ \left( \sum_{i=1}^d \frac{v_i(k)}{\Delta x_i(k)} + c(k) \sqrt{\sum_{i=1}^d \frac{1}{\Delta x_i^2(k)}} \right)^{-1} \right\} \quad (4.5)$$

where the search of the minimum has to extend over all grid zones  $k = 1 \dots N$  ( $N$  is a number of all grid zones). The parameter  $d$  is the number of considered dimensions,  $\Delta x_i(k)$  is the size of a grid cell  $k$ ,  $v_i(k)$  is a local speed of flow and  $c(k)$  is a local sound speed.

### 4.1.3. Double Mach Reflection of a Strong Shock

To test the hydrodynamic solver of the Herakles code we simulated the the double mach reflection of a strong shock in Cartesian geometry (Fig. 4.3). It consists of a Mach 10 shock in a gas extending from the top to the bottom of the grid which initially makes a  $60^\circ$  angle with a reflecting wall coincident with the x-axis at  $x=1/6$  cm. The left-hand boundary (at  $x = 0$  cm) is assigned with the values for the initial post-shock flow and at the right-hand boundary ( $x = 3$  cm) all gradient are set equal to zero. The values along the top boundary are set to describe the exact motion of the initial Mach 10 shock. The bottom boundary is reflective and set from  $x = 0$  cm to  $x = 1/6$  cm, to the values of the initial post-shock state. A detailed description of the problem can be found in [Woodward & Colella \(1984\)](#).

The density structure at  $t = 0.2$  s agrees very well the structure described by [Woodward & Colella \(1984\)](#). The flow has a complicated structure consisting of several shocks colliding with each other, namely the incident shock, a curved reflected shock and the two Mach stems (or waves) connecting the intersection points (Fig. 4.3). The density jumps clearly mark the shock boundaries.

## 4.2. Nuclear Reactions

In order to take into account nuclear burning in our calculations, we have to solve a nuclear network, which consists of 1st order nonlinear differential equations describing the change in temperature due to the amount of energy released by nuclear burning resulting from element transmutation.

$$\dot{Y}_i - F(Y_i, T) = 0 \quad (4.6a)$$

$$\dot{T} - H(Y_i, T) = 0 \quad (4.6b)$$

where  $\dot{Y}_i$  is the abundance change of  $i$ -th element,  $F$  is the right hand side of Eq. 3.9, and  $H$  the right hand side of the Eq. 3.10. This system is stiff, *i.e.* standard numerical techniques fail as very different timescales have to be treated. Therefore, we solve the nuclear reaction network with the semi-implicit Bader-Deuffhard method ([Bader & Deuffhard 1983](#); [Press et al. 1992](#)) which uses small time substeps to integrate the set of equations up to a desired accuracy.

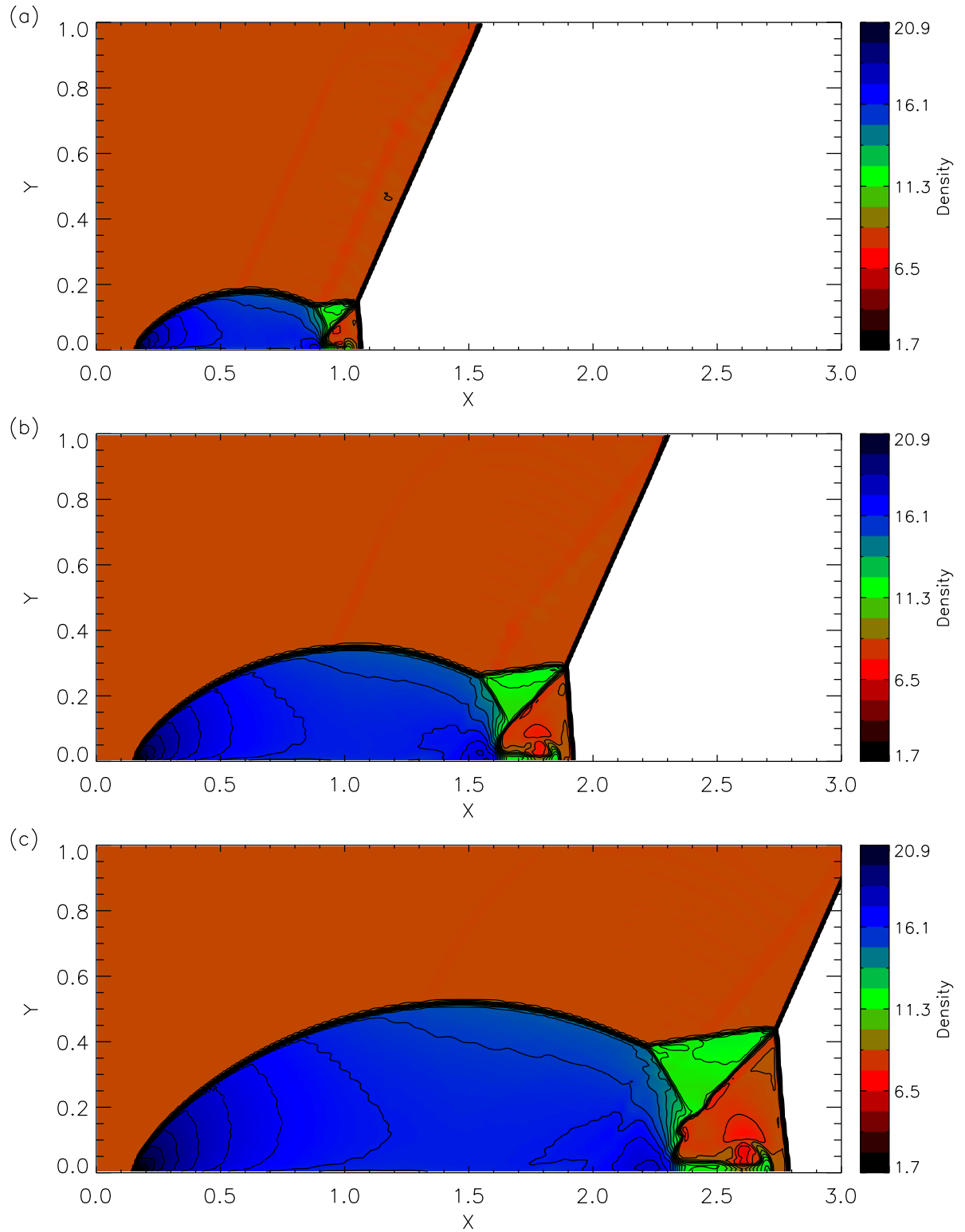


**Figure 4.3.:** Density (in  $\text{g cm}^{-3}$ ) contour plots of the flow resulting from the double Mach reflection of a Mach 10 shock from a wall at (a) 0.06 s (b) 0.12 (c)  $t = 0.2 \text{ s}$  computed on a two-dimensional Cartesian grid with  $480 \times 120$  zones. The number of contours is 30, and they span a density range from 1.7 to  $20.9 \text{ g cm}^{-3}$ . The white region to the right has a density of  $1.4 \text{ g cm}^{-3}$ .

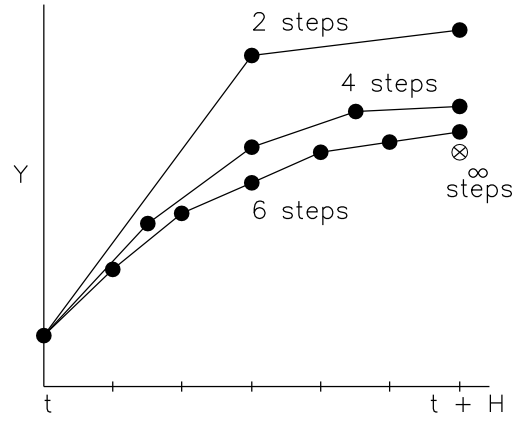


**Figure 4.4.:** Illustration of the Richardson extrapolation. The large interval  $H$  over which the integration is performed is divided into substeps (2,4,6 etc.) until the desired accuracy of solution  $Y$  is achieved when extrapolating to infinitely fine substeps  $h \rightarrow 0$  (crossed circle).

### Bader-Deuffhard Scheme

It is a numerical scheme for the integration of ordinary differential equations which returns high accuracy solutions with minimal computational efforts (Press et al. 1992). The basic principle of the scheme, *i.e.* the Richardson extrapolation, is demonstrated in the Figure 4.4. We seek for a solution  $Y$  at time  $t + H$ , where  $H$  is a timestep over which we need to integrate the equations. A single timestep which takes us from  $t$  to  $t + H$  is a grand leap consisting of smaller substeps  $h$  at which the solution of the equations is calculated. A more accurate solution at time  $t + H$  can be obtained by larger number of substeps. The timestep  $H$  is computed several times with increasing number of substeps, which allows one to construct a series of solutions at time  $t + H$  as a function of the size of the substeps. Such a series can be extrapolated to the limit when the size of the substeps is zero ( $h \rightarrow 0$ ), and the solution is supposed to have high accuracy.

There is always an upper limit for the timestep  $H$  and we are forced to reduce  $H$  rather than further subdivide it more finely, as the extrapolation to the limit  $h \rightarrow 0$  is not possible. The scheme has therefore subroutines which adapt the stepsize  $H$  to match a prescribed bound on the accuracy of the integration.

All serial subroutines of the Bader-Deuffhard integrator can be found in the Numerical Recipes in Fortran by Press et al. (1992). For the Herakles code the subroutines were vectorized by Konstantinos Kifonidis.

### Alternative Numerical Scheme

In order to test our solver of the nuclear reaction network based on the Bader-Deuffhard scheme (see the next Sect. 4.2.1) we used an approach suggested by Müller (1986) using the implicit Euler-backward discretization of the nuclear reaction network:

$$Y_i^{n+1} - Y_i^n - \Delta t \cdot F(Y_j^{n+1}, T^{n+1}) = 0 \quad (4.7a)$$

$$\epsilon_i^{n+1} - \epsilon_i^n - \Delta t \cdot H(Y_j^{n+1}, T^{n+1}) = 0 \quad (4.7b)$$

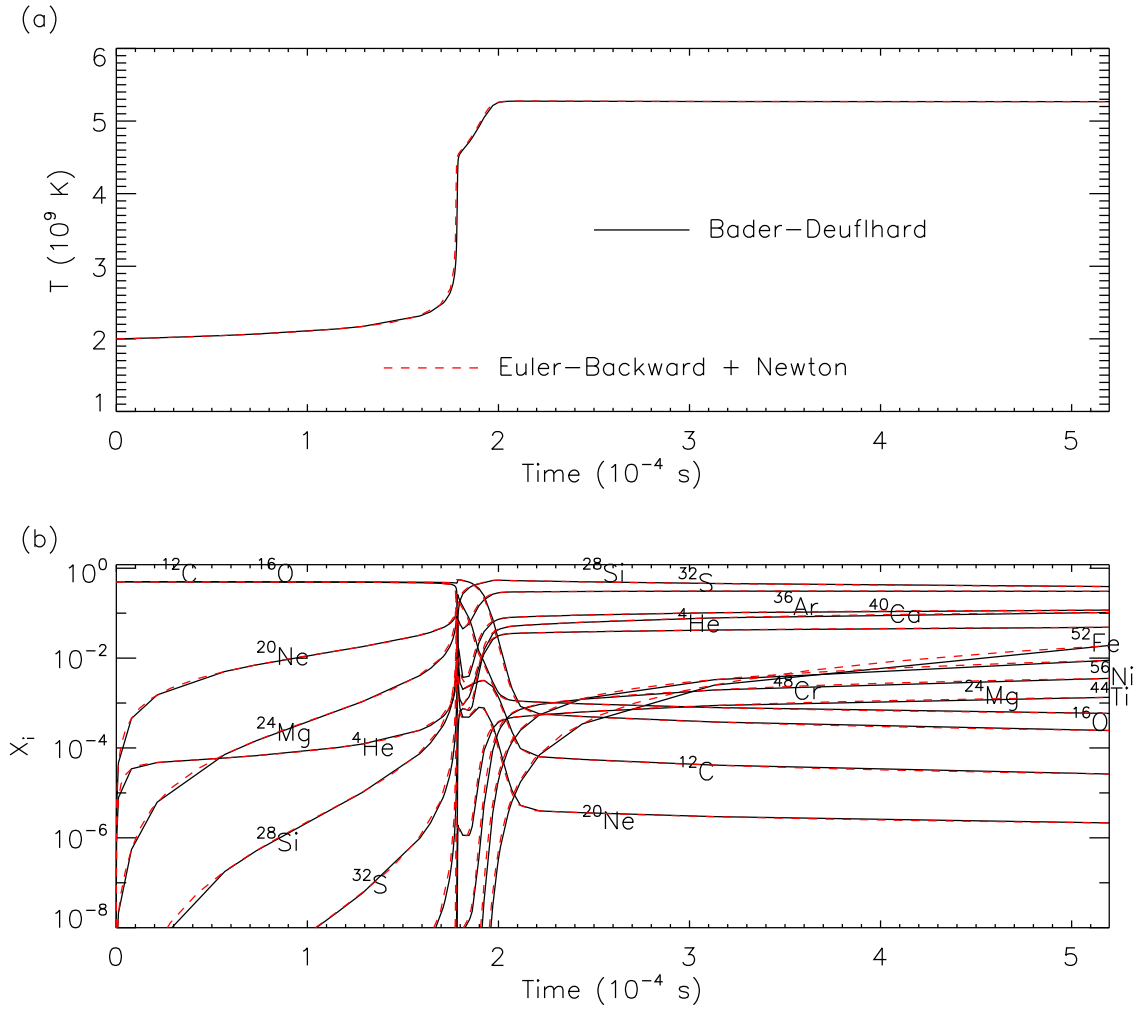


**Figure 4.5.:** Temporal evolution of temperature  $T$  (a) and mass fractions  $X_i$  (b) in one-zone burning computed with the Euler-backward plus Newton scheme (red-dashed) and with the Bader-Deuffhard scheme (black). The initial density is  $\rho = 1 \times 10^7 \text{ g cm}^{-3}$ , initial temperature is  $T = 2 \times 10^9 \text{ K}$  and the initial composition is  $X(^{12}\text{C})=0.5$  and  $X(^{16}\text{O})=0.5$ .

where  $i = 1 \dots M$ ,  $j = 1 \dots M$  and  $M$  is the number of species.  $F$  and  $H$  are nonlinear functions of the arguments (Eq. 3.9 and Eq. 3.6, respectively). The internal energy is a known function of abundances  $Y_i$  and temperature  $T$  via the equation of state (see Sect. 3.2) and therefore the above equations are a nonlinear system for the  $M + 1$  unknown variables  $Y_i^{n+1}$  and  $T^{n+1}$ . The whole system is solved by Newton scheme in which abundances and temperature are updated together.

#### 4.2.1. One-Zone Nuclear Burning

We performed several calculations of nuclear reaction network build up from 13  $\alpha$  nuclei (from  $^4\text{He}$  up to  $^{56}\text{Ni}$ ). We tried to simulate a homogeneous region of constant density with a certain initial composition and temperature. Evolution of chemical species from one of such simulations is shown in the Fig. 4.5.

We computed composition evolution for several homogeneous regions having density within the range from  $1 \times 10^7 \text{ g cm}^{-3}$  to  $1 \times 10^{10} \text{ g cm}^{-3}$  and temperature within the range from  $1 \times 10^9 \text{ K}$

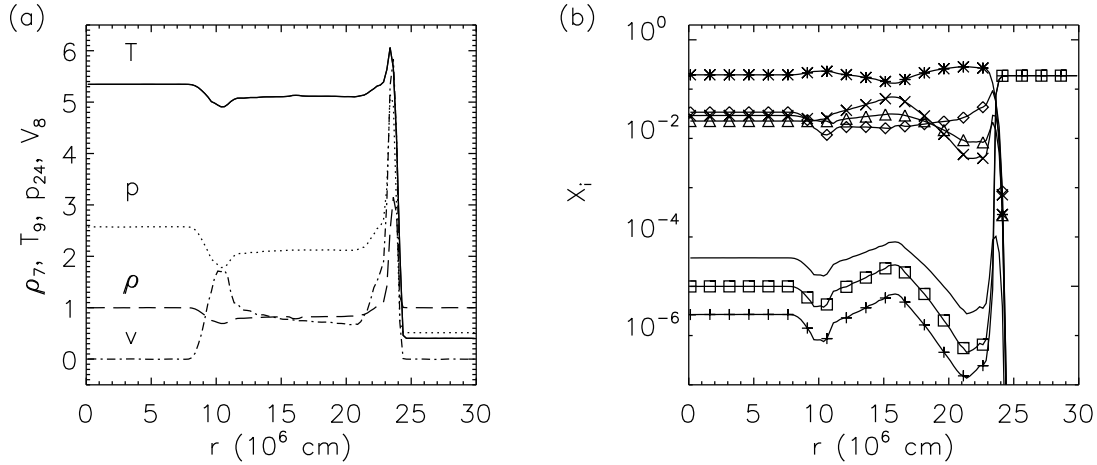


**Figure 4.6.:** A structure of the spherical detonation wave at  $t = 13$  ms computed on a cylindrical grid with  $120 \times 45$  zones ( $45^\circ > \theta > 135^\circ$ ). (a) Angular averaged distribution of temperature  $T_9$  (in  $10^9$  K), pressure  $p_{24}$  (in  $10^{24}$  dyn cm $^{-2}$ ), density  $\rho_7$  (in  $10^7$  g cm $^{-3}$ ) and velocity  $v_8$  (in  $10^8$  cm s $^{-1}$ ). (b) Angular averaged mass fraction profiles of  $^4\text{He}$  ( $\diamond$ ),  $^{12}\text{C}$  (+),  $^{16}\text{O}$  ( $\square$ ),  $^{24}\text{Mg}$  (no symbol),  $^{28}\text{Si}$  ( $\times$ ),  $^{40}\text{Ca}$  ( $\triangle$ ) and  $^{56}\text{Ni}$  (\*).

to  $2 \times 10^{10}$  K. To check the correctness of our implementation of the Bader-Deuffhard scheme, all calculations were performed by both, the Bader-Deuffhard method and by the semi-implicit Euler backward method with a Newton scheme.

Considering the temporal evolution of the mass fraction and temperature, the relative difference between the schemes is better than 1 %. Our experience with the Bader-Deuffhard scheme is such that in comparison to the approach by Müller (1986), it is faster under moderate conditions (*i.e.*  $\rho \sim 10^7$  g cm $^{-3}$  and  $T \sim 10^9$  K). At more extreme conditions with higher temperatures or densities, the schemes are roughly equally fast.

#### 4.2.2. White Dwarf Detonation Problem

In order to check our coupling of the nuclear solver to our hydrodynamic solver (Sect. 4.1) we attempted to compute a detonation problem in a white dwarf star.

The white dwarf problem is about calculating of spherical detonation in a homogeneous star with density  $\rho = 10^7$  g cm $^{-3}$ . Its inner part up to a radius of  $1.5 \times 10^7$  cm is heated to a temperature of  $2 \times 10^9$  K. The surrounding envelope is kept cold at a temperature  $T = 4 \times 10^8$  K. The composition is constant across the whole star and consists of an equal mass of  $^{12}\text{C}$  and  $^{16}\text{O}$ .

The results from our simulation (performed on a cylindrical grid) are depicted in the Fig. 4.6 and compared with those of a similar computation performed with the Prometheus code (Müller et al. 1991; Fryxell et al. 1991) by Ewald Müller and Matthias Steinmetz. The agreement between both calculations is better than 2%, although there is a minor difference in the position of the detonation front which reaches a radius  $r \sim 2.5 \times 10^7$  cm already at 13 ms using our code, whereas in the other simulation it reaches the same position a bit later at 15 ms.

Clearly, one can recognize that the detonation front is followed by  $^{56}\text{Ni}$ , and  $^{28}\text{Si}$  -  $^{40}\text{Ca}$  rich layer with mass fraction at around  $10^{-1}$  and  $10^{-2}$ , respectively. The hot central region has a very low  $^{12}\text{C}$  and  $^{16}\text{O}$  mass fraction at around  $10^{-6}$  and  $10^{-5}$ , respectively. The latter numbers fit well those obtained by the Prometheus code, within a relative discrepancy less than a few



percent. We suspect that our different approach for solving the nuclear reaction network could lead under such extreme conditions to differences of this order.

### 4.3. Screening

At higher densities each nucleus tends to attract neighboring electrons and form a negative charge cloud around it, which shields its Coulomb barrier (screening) and increases the rate of thermonuclear reactions. To determine the enhancement effect, one usually computes a screening factor and multiplies it with a given reaction rate of two charges  $Z_1$ ,  $Z_2$  which participate in the reaction. For densities at around  $10^5 \text{ g cm}^{-3}$  (weak screening regime) which are typical for the core helium flash simulations, the screening factor

$$f = \exp \frac{Z_1 Z_2 e^2}{\lambda_D k_B T} \quad (4.8)$$

where  $\lambda_D$  is Debye-length. The Debye-length is a distance beyond which the positive charge is shielded by the surrounding cloud of negative charges *i.e.* the radius of the charged cloud.

[Dewitt et al. \(1973\)](#) give the following expression for weak screening:

$$f = \exp[\Lambda_{12} + \Lambda_{12}^2(\ln \Lambda_{12} + 0.8364)] \quad \text{with} \quad \Lambda_{12} = \frac{Z_1 Z_2 e^2}{\lambda_D k_B T} . \quad (4.9)$$

In our simulations, we implemented the screening using a modified version of public subroutine written by Frank Timmes <sup>4</sup>. The subroutine calculates screening factors of nuclear reaction rates based on the calculations of [Graboske et al. \(1973\)](#); [Alastuey & Jancovici \(1978\)](#) and [Itoh et al. \(1979\)](#). Considering that mainly the triple- $\alpha$  reaction contributes to the energy generation during the flash, we were calculating screening factors only for this reaction, assuming the weak screening regimes. There is almost no difference in nuclear energy generation when assuming screening of all nuclear reactions involved in our calculations. This simplification saved us almost 20 % of total computational time per computed model. The screening factors for the included reactions during core helium flash varies between 2 and 26 (for the triple- $\alpha$  reaction rate is  $f \sim 2.5$ ).

### 4.4. Neutrinos

Neutrino losses were implemented as a sink term  $\varepsilon_\nu$  in the temperature equation of the nuclear reaction network

$$\frac{\partial T}{\partial t} = \dot{\varepsilon} \frac{\partial T}{\partial \varepsilon} \quad \text{where} \quad \varepsilon = \varepsilon_{nuc} - \varepsilon_\nu \quad (4.10)$$

$\varepsilon_\nu$  was calculated with a modified subroutine of Frank Timmes <sup>3</sup>. It computes neutrino losses using the analytic fits of [Itoh et al. \(1996\)](#) that include plasma neutrino, photoneutrino and Bremsstrahlung neutrino processes  $[e^- + (z, a) \rightarrow e^- + (z, a) + \nu + \bar{\nu}, n + n \rightarrow n + n + \nu + \bar{\nu}, n + p \rightarrow n + p + \nu + \bar{\nu}]$ .

<sup>4</sup>[http://cococubed.asu.edu/code\\_pages/codes.shtml](http://cococubed.asu.edu/code_pages/codes.shtml)

## 4.5. Gravitation

We computed effects of gravity using approach by [Müller & Steinmetz \(1995\)](#). Since our models of the core helium flash are non-rotating and do not show large-scale deviation from sphericity, we used the one-dimensional Newtonian gravitational potential

$$\Phi = G \frac{M(r)}{r} \quad (4.11)$$

where  $M(r)$  is the angle averaged mass distribution.

To account for gravity effects during integration by PPM scheme over a single timestep  $\Delta t = t^{n+1} - t^n$ , the following four steps are performed:

1. A modification of the left and right velocity state of the Riemann problem ( $\bar{u}_{i,R}$  and  $\bar{u}_{i,L}$ , respectively) is performed, using the time-centered prediction of gravitational acceleration  $\nabla \Phi_i^{n+1/2}$  according to the following relations

$$\bar{u}_{i,R} \rightarrow \bar{u}_{i,R} - \frac{\Delta t}{2} (\nabla \Phi_i^{n+1/2})_R \quad (4.12)$$

$$\bar{u}_{i,L} \rightarrow \bar{u}_{i,L} - \frac{\Delta t}{2} (\nabla \Phi_i^{n+1/2})_L \quad (4.13)$$

2. The calculation by PPM scheme continues by solving the Riemann problem with the modified left and right states (Step 1).
3. At the end of the integration at  $t^{n+1}$ , new values are obtained for velocity  $\tilde{\mathbf{v}}_i^{n+1}$ , specific total energy  $\tilde{e}_i^{n+1}$  and gravitational potential  $\tilde{\Phi}_i^{n+1}$
4. The velocity and the total energy are corrected via

$$\mathbf{v}_i^{n+1} = \tilde{\mathbf{v}}_i^{n+1} - \frac{\Delta t}{2} (\nabla \Phi_i^n + \nabla \tilde{\Phi}_i^{n+1}) \quad (4.14)$$

$$e_i^{n+1} = \tilde{e}_i^{n+1} - \frac{\Delta t}{2} (\mathbf{v}_i^n \nabla \Phi_i^n + \mathbf{v}_i^{n+1} \nabla \tilde{\Phi}_i^{n+1}) \quad (4.15)$$

### 4.5.1. Polytropic Star

In order to test this implementation of gravity we were inspired by [Swesty & Myra \(2006\)](#). We choose a polytrope with an index  $n = 1$ , which corresponds to polytropic equation of state with an adiabatic index  $\gamma = 2$ . Using a solution of the Lane-Emden equation, we constructed a polytropic star according to the analytical solution ([Chandrasekhar 1967](#)).

$$\rho(\xi) = \rho_c \frac{\sin \xi}{\xi} \quad , \quad (4.16)$$

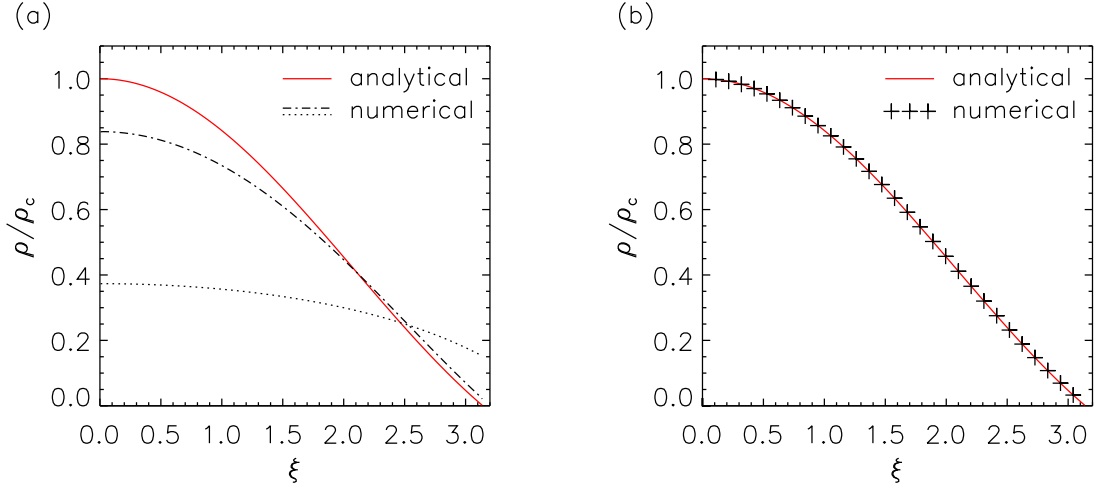


**Figure 4.7.:** The (normalized) density profile of the polytrope with gravity switched off (a) after 0.01 (dash-dotted) and 0.5 of sound crossing timescale (dotted), respectively and (b) with gravity switched on after 135 sound crossing timescales (crosses). The red solid line represents the analytical profile of the polytrope.

where  $\rho_c$  is the central density, and  $\xi$  is a radial coordinate defined such that the radius,

$$r = \beta\xi \quad (4.17)$$

and

$$\beta = \left( \frac{(n+1)K}{4\pi G} \rho_c^{(1/n)-1} \right)^{1/2}, \quad (4.18)$$

The quantity  $K$  is a polytropic constant. For  $n = 1$ ,  $\beta$  is independent of  $\rho_c$ . For practical reasons we set  $\rho_c = 1 \text{ g cm}^{-3}$ , and choose  $K = 2\pi G$ , such that  $\beta = 1$ . Thus, the density varies between 0 and  $1 \text{ g cm}^{-3}$ , and the radius from 0 to  $\pi$  centimeters.

Our simulations show (Fig. 4.7) that without gravity, the initial analytical density stratification quickly becomes very shallow because of the fast expansion of the star. When gravity is switched on, the polytropic density distribution keeps its initial shape even after 135 sound crossing timescales (see Sect. 2.3). The relative difference with the analytical profile is less than 0.1 %.

## 4.6. Thermal Transport

For taking into account the energy transport by conduction and radiation (Sect. 3.5) we used the thermal transport coefficient obtained with the modified version of the subroutine written by Frank Timmes<sup>5</sup>. Temperature gradient was discretized by the first order Euler scheme. The thermal energy flux is subtracted from the energy flux of the hydrodynamical flow.

<sup>5</sup>[http://cococubed.asu.edu/code\\_pages/codes.shtml](http://cococubed.asu.edu/code_pages/codes.shtml)

## 4.7. Performance and Parallelization

The code was designed to perform reasonably on different computer systems, including massively parallel ones with vector processors. The computational kernels are fully vectorized and allow the vector length to be adjusted to the particular memory architecture of the system to be used. This allows for optimal performance on both vector and superscalar, cache-based machines.

We tested the code on the IBM p690, IBM p575, IBM Power6 System supercomputers and on the supercomputer ALTIX 4700 with cc-NUMA architecture which requires special treatment of the initialization and data scatter for parallel computing.

The current version of the code is parallelized with OpenMP. Its scaling properties on the SGI ALTIX 4700 machine of the Leibniz Rechenzentrum<sup>6</sup> are listed in Tab. 4.1. The achieved performance is satisfactory which allowed us to compute a set of multidimensional hydrodynamical core helium flash models with the highest resolution ever done.

**Table 4.1.:** The scaling behavior of the code HERAKLES on the SGI's ALTIX 4700 platform<sup>5</sup>. The various table entries are: number of processors nProc, speedup with a given number of processors of the full code SpeedUp (total), of the hydrodynamical part of the code SpeedUp (hydro), and of the nuclear network solver SpeedUp (nuclear), respectively. Performed on domain with  $400 \times 180 \times 360$  grid zones.

nProc	SpeedUp (total)	SpeedUp (hydro)	SpeedUp (nuclear)
1	1.	1.	1.
8	7.8	7.95	7.6
32	25.6	28.7	24.
64	42.	50.	38.
128	43.	80.	34.5

---

<sup>6</sup>[www.lrz.de](http://www.lrz.de)

# 5

## Initial Stellar Models

Hydrodynamic simulation of a star is an initial value problem and therefore it requires initial conditions which provide the thermodynamic structure *e.g.* an initial stellar model computed by a stellar evolutionary code. Stellar evolution calculations are based on the numerical solution of one-dimensional stellar evolution equations. Within a star they describe hydrostatic equilibrium, energy conservation, energy transport and changes of chemical composition due to nuclear reactions and mixing of elements ([Kippenhahn et al. 1967](#); [Kippenhahn & Weigert 1990](#)). Multi-dimensional phenomena are described by phenomenological theories like *e.g.* mixing length theory ([Vitense 1953](#); [Böhm-Vitense 1958](#); [Kippenhahn & Weigert 1990](#); [Weiss et al. 2004](#)).

### 5.1. General Remarks

Stellar evolutionary models contain information about the whole stellar structure from the center of the star up to its surface. Since only the helium core of the model (without its very central part) is of interest to us, we consider only initial data of the models from and up to a certain radius of a star, and interpolate all relevant quantities (*e.g.* density, temperature, composition) onto our Eulerian computational grid using polynomial interpolation ([Press et al. 1992](#)). Due to interpolation errors and subtle differences in the input physics, the interpolated model is no longer in perfect hydrostatic equilibrium. To balance perfectly also the gravitational and pressure forces in the interpolated model, we use an iterative procedure in the first hydrodynamic timestep (see next Sect. [5.2](#)). The process produces a small temperature decrease with respect to the temperature profile of the original model (*e.g.* Fig. [5.1](#)). Depending on the radial resolution of the Eulerian grid, the differences do not exceed a few percent. The resulting changes in density and pressure profiles are negligible due to the strong electron degeneracy of the gas. The main cause of the slight destabilization of the mapped initial stellar model is the use of different equations of state in our hydrodynamic and stellar evolutionary code.

## 5.2. Stabilization

The stabilization subroutine consists of iterative procedure whereby one tries to reconstruct hydrostatic equilibrium in the mapped stellar model using the equation of state implemented in the hydrodynamic code. It is computing the difference  $\Delta p$  between the pressure gradient computed for a given radial density profile according to the equation of hydrostatic equilibrium and the pressure gradient  $\nabla p$ , which we get by solving the Euler momentum equation. The equation of the hydrostatic equilibrium is

$$\nabla p = -\rho g \quad (5.1)$$

The stabilization algorithm consists of the following steps:

1. The pressure gradient  $\nabla p$  is computed by our PPM solver and the following Eq. 5.2

$$\frac{d}{dr}\Delta p = (\nabla p - \rho g) \quad (5.2)$$

is integrated along the radial direction. The product of the right hand side is multiplied by a factor, typically having a value  $\sim 10^{-3}$  in order to allow the equation of state to converge to a new temperature (Step 3) for a new value of the pressure (Step 2).

2. The correction  $\Delta p$  to the original pressure  $p_i^0$  for every grid cell  $i$  is applied and a new pressure  $p_i$  is obtained.

$$p_i = p_i^0 + \Delta p \quad (5.3)$$

3. The equation of state is called in order to update temperature and the internal energy.
4. The deviation from hydrostatic equilibrium (Eq. 5.4) is computed

$$\frac{\nabla p + \rho g}{\nabla p - \rho g} \quad (5.4)$$

and if it is less than a certain value (typically  $\sim 10^{-5}$ ), that we choose at the beginning, the iteration is stopped. If the criterion is not fulfilled, the algorithm returns to the Step 1, with the new (corrected) pressure  $p_i$ , which is now closer to the equilibrium pressure, than the original one  $p_i^0$  and the whole stabilization process is repeated again.

## 5.3. The Models

For our hydrodynamic simulations we used four initial stellar evolution models (Tab. 5.1). All initial models are partially electron degenerate. Whereas the region beneath the temperature maximum of all models is strongly electron degenerate (degeneracy parameter  $\psi \sim 20$ ), the degeneracy at and above the temperature maximum is already significantly reduced due to

**Table 5.1.:** Some properties of the initial models: Total mass  $M$ , stellar population, metal content  $Z$ , mass  $M_{He}$  and radius  $R_{He}$  of the helium core ( $X(^4He) > 0.98$ ), nuclear energy production in the helium core  $L_{He}$ , temperature maximum  $T_{max}$ , radius  $r_{max}$  and density  $\rho_{max}$  at the temperature maximum.

Model	$M$ [ $M_{\odot}$ ]	Pop.	$Z$	$M_{He}$ [ $M_{\odot}$ ]	$R_{He}$ [ $10^9$ cm]	$L_{He}$ [ $10^9 L_{\odot}$ ]	$T_{max}$ [ $10^8$ K]	$r_{max}$ [ $10^8$ cm]	$\rho_{max}$ [ $10^5$ g cm $^{-3}$ ]
M	1.25	I	0.02	0.47	1.91	1.03	1.70	4.71	3.44
DM	0.85	II	0.001	0.48	1.6	3.4	1.91	4.9	2.15
JW	1.49	I	0.02	0.47	2.65	0.5	2.01	7.7	0.67
SC	0.85	III	0.00	0.5	5.45	0.004	2.04	11.	0.08

strong expansion. In the convection zone, the degeneracy parameter  $\psi$  remains almost constant which is a result of an almost adiabatic temperature gradient<sup>1</sup>. The gradient is also responsible for an almost constant entropy in the convection zone. Every model was modified slightly by our stabilization procedure to retain the hydrostatic equilibrium in our hydrodynamic code.

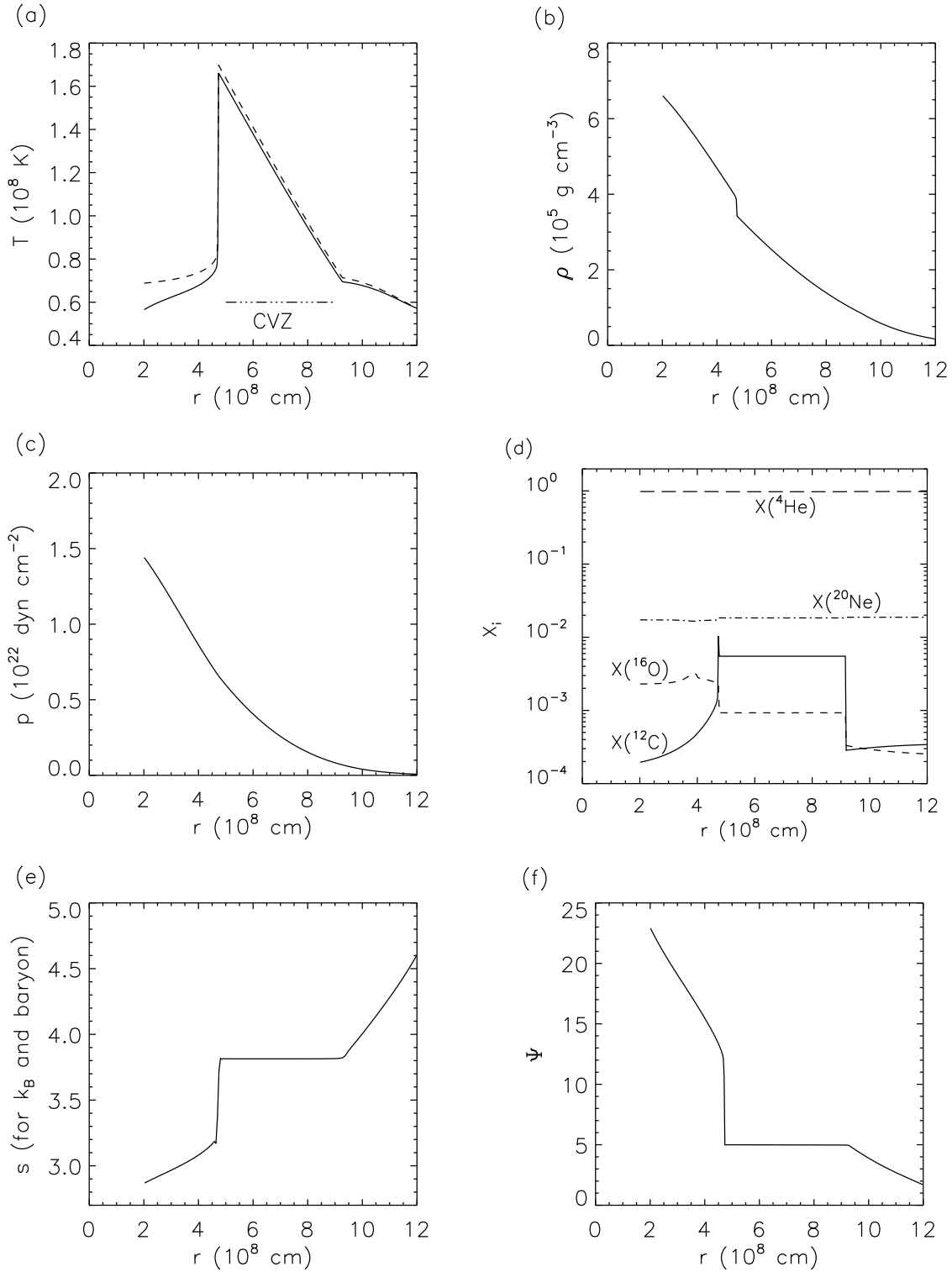
### 5.3.1. Model M: Mass = 1.25 $M_{\odot}$ and $Z = 0.02$

Table 5.1 summarizes some properties of our initial model M, which was obtained from stellar evolutionary calculations with the “Garstec” code (Weiss & Schlattl 2000, 2007). It corresponds to a Pop I star with a mass of 1.25  $M_{\odot}$  and a metallicity  $Z = 0.02$  at the peak of the core helium flash ( $L_{He} \sim 10^9 L_{\odot}$ ), computed with the hydrostatic stellar evolution code. During this violent episode, the star is located at the tip of the red giant branch in the H-R diagram (Fig. 1.1), hence being a red giant consisting of a small central helium core with a radius of  $\sim 1.9 \times 10^9$  cm, surrounded by a hydrogen burning shell and a huge convective envelope with a radius of  $\sim 10^{13}$  cm. Figure 5.1 shows the temperature distribution inside the helium core, which is characterized by an off-center temperature maximum  $T_{max}$ , from where the temperature steeply drops towards smaller radii and follows a superadiabatic<sup>2</sup> gradient towards larger radii (convection zone). The radius  $r_{max}$  of the temperature maximum coincides with the bottom of the convection zone. The almost discontinuous temperature stratification near  $T_{max}$  (temperature inversion), where the temperature rises from  $7 \times 10^7$  K to  $1.7 \times 10^8$  K, results from an interplay between neutrino cooling and heating by nuclear burning. Figure 5.1 also shows the density and pressure stratification of the model. One recognizes that the temperature inversion is correlated with a drop in density. A detailed view reveals that the steep increase in temperature corresponds to a decrease in density by 11%, an increase in the ion pressure by 70%, and a drop in the electron pressure by 9%, respectively. Even at the peak of the core helium flash, the helium core is strongly degenerate: compared with the electron pressure, the ion pressure is lower by a factor of 6, while the radiation pressure is smaller by almost 3 orders of magnitude.

The stellar model contains the chemical species  $^1H$ ,  $^3He$ ,  $^4He$ ,  $^{12}C$ ,  $^{13}C$ ,  $^{14}N$ ,  $^{15}N$ ,  $^{16}O$ ,  $^{17}O$ ,  $^{24}Mg$ , and  $^{28}Si$ . However, as we are not interested in the detailed chemical evolution of the star, it is therefore unnecessary to consider all of these species in our hydrodynamic simulations, since the triple- $\alpha$  reaction dominates the energy production rate during the core helium flash. In our hydrodynamic simulations, we therefore adopt only the abundances of  $^4He$ ,  $^{12}C$ , and  $^{16}O$ . The remaining composition is assumed to be adequately represented by a gas with a mean molecular weight equal to that of  $^{20}Ne$  (Fig. 5.1).

<sup>1</sup>In the convection zone holds the relation  $T \propto \rho^{\gamma-1}$  with the adiabatic exponent  $\gamma \sim 5/3$ . Since  $\rho T^{-3/2} = f(\psi)$ , is the  $\psi$  constant.

<sup>2</sup>The superadiabatic gradient  $\nabla$  is defined by the condition  $\nabla > \nabla_{ad}$  (see Sect. 2.2).



**Figure 5.1.:** The initial internal structure of the model M as a function of radius. (a) Original temperature  $T$  (dashed) and temperature after mapping and stabilizing the model (solid) used as initial condition in the hydrodynamic simulations. CVZ marks the convection zone. (b) Density  $\rho$ , (c) Pressure  $p$ , (d) Chemical composition  $X_i$  (e) Entropy  $s$ , and (f) Degeneracy parameter  $\Psi$ .



### 5.3.2. Model DM: Mass = 0.85 $M_{\odot}$ and Z = 0.001

This initial model (Tab. 5.1, Fig. 5.2) was computed by Demarque & Mengel (1971), (sequence G in their paper), and represents a 0.85  $M_{\odot}$  Pop II star with a metallicity  $Z=0.001$  at the peak of the core helium flash. It was further modified for hydrodynamic simulations by Cole & Deupree (1980) to guarantee hydrostatic equilibrium with respect to the physics included in their models. This model also we used for our hydrodynamic simulations. As expected, the model is characterized by an off-center temperature maximum  $T_{max}$ . The composition of the model is assumed to be constant throughout the whole star:  $X(^4\text{He}) = 0.975$ ,  $X(^{12}\text{C}) = 6.25 \times 10^{-3}$ ,  $X(^{16}\text{O}) = 5 \times 10^{-4}$ , the rest being  $^{20}\text{Ne}$ .

### 5.3.3. Model JW: Mass = 1.49 $M_{\odot}$ and Z = 0.02

This initial model (Tab. 5.1, Fig. 5.2) was computed by Josef Wagenhuber with the stellar evolution code “Garstec” (Weiss & Schlattl 2000, 2007). It represents a metal-rich Pop I star with a mass of 1.49  $M_{\odot}$  at the peak of a not very violent core helium flash; helium luminosity  $L_{He} \sim 5.6 \times 10^7 L_{\odot}$ . Due to the low energy production, it would take relatively long to reach a stable convection within our hydrodynamic simulations. Therefore, the model was recomputed with suppressed convective mixing in the early phases of the flash. It led to an increased energy production and a higher temperature maximum at the peak of the flash (Wagenhuber 1996; Achatz 1995). Since it is not necessary to consider all species included in the original stellar model, as the triple- $\alpha$  reaction dominates the energy production, we used for our hydrodynamic simulations only abundances of  $^4\text{He}$ ,  $^{12}\text{C}$ , and  $^{16}\text{O}$  and the remaining is assumed to be  $^{20}\text{Ne}$ .

### 5.3.4. Model SC: Mass = 0.85 $M_{\odot}$ and Z = 0.0

This initial model (Tab. 5.1, Fig. 5.3) was computed by Simon W. Campbell using the Monash/Mount Stromlo STAR code *i.e.* MONSTAR code (Campbell & Lattanzio 2008; Wood & Zarro 1981). It corresponds to a metal-free Pop III star with a mass of 0.85  $M_{\odot}$  at a peak of a rather peculiar core helium flash that is typical for extremely metal-poor stars. It commences by an off-center ignition of helium in a relatively dense environment under degenerate conditions, and results in a fast growing convection zone powered by helium burning that relatively quickly reaches the surrounding hydrogen shell (Fujimoto et al. 1990). This suddenly causes mixing of protons down into the hot helium convection zone (Fig. 5.3), and leads to rapid nuclear burning via the CNO cycle: the dual core flash (Campbell & Lattanzio 2008). This event has also been refereed to as helium flash induced mixing (Schlattl et al. 2001; Cassisi et al. 2003; Weiss et al. 2004), and helium flash-driven deep mixing (Suda et al. 2004). The CNO burning leads to an increase of the temperature inside the helium-burning driven convection zone, and causes its splitting into two: one still powered by the helium burning and a second one by the CNO cycle (Fig. 2.2). The energy production rate by helium burning is by almost an order of magnitude lower at around the peak of the dual core flash than the production by the CNO cycle. For our hydrodynamic simulations we adopted exactly mass fractions of  $^1\text{H}$ ,  $^3\text{He}$ ,  $^4\text{He}$ ,  $^{12}\text{C}$ ,  $^{14}\text{N}$ ,  $^{16}\text{O}$ . In addition we assumed an equilibrium CNO mass fraction of  $^{13}\text{C}$  equal to  $X(^{12}\text{C})/3.5$  in the hydrogen rich region. The remaining composition is assumed to be  $^{20}\text{Ne}$ . Incorporating of these species does not allow for complete CNO nuclear chain because  $^{13}\text{N}$  and  $^{15}\text{O}$  is missing. We neglected this elements intentionally, as consideration of more species makes simulations more computationally demanding. The neglect of  $^{13}\text{N}$  and  $^{15}\text{O}$  resulted in a reduced energy generation rate in the region of injected hydrogen by 30 % compared to the original stellar model.

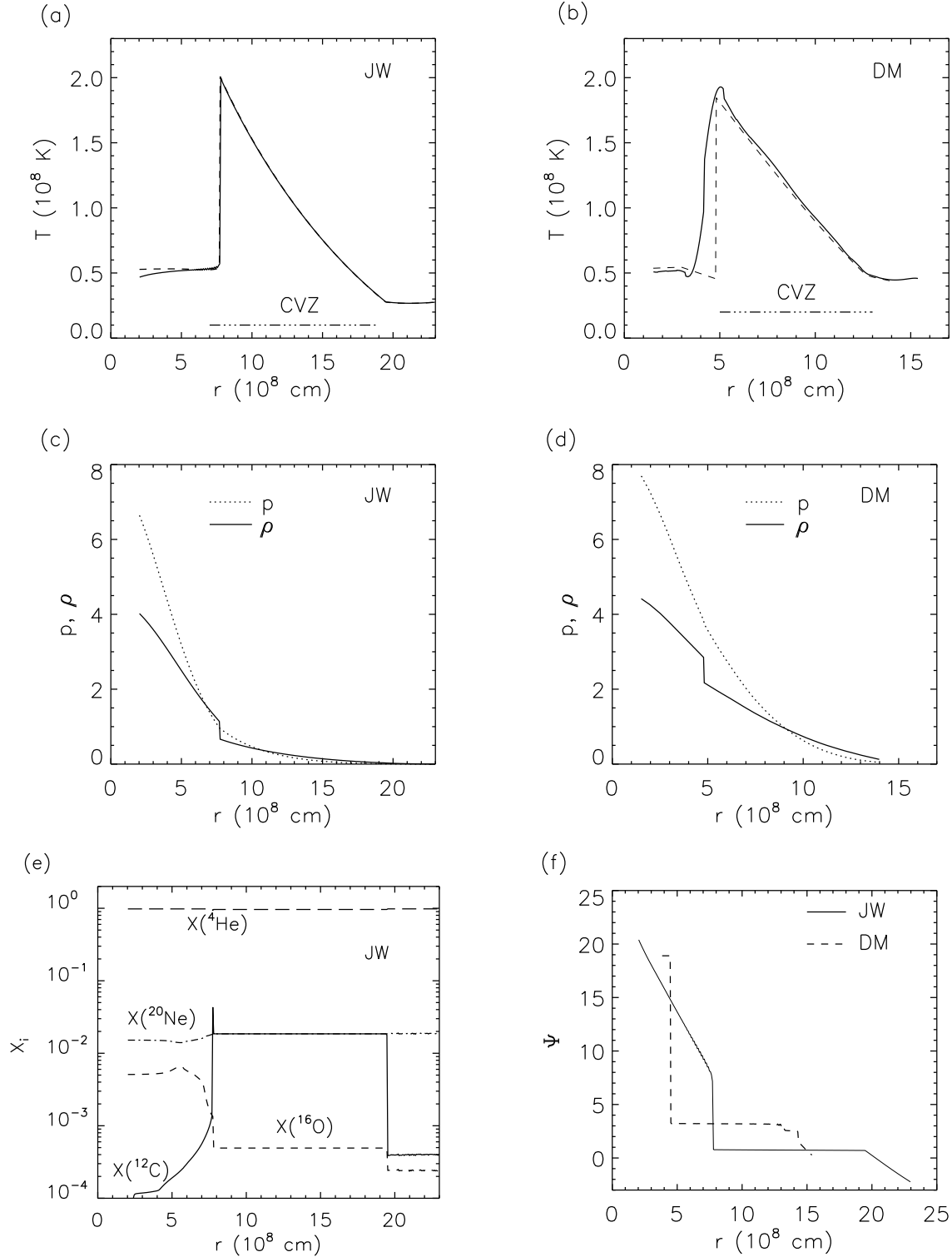


**Figure 5.2.:** The initial internal structure of the model DM and JW as a function of radius. (a), (b) Original temperature  $T$  (dashed) and temperature after mapping and stabilizing the model (solid) used as initial condition in the hydrodynamic simulations. CVZ marks the convection zone. (c), (d) Pressure  $p$  (in  $10^{22}$  dyn  $\text{cm}^{-2}$ ) and density  $\rho$  (in  $10^5$  g  $\text{cm}^{-3}$ ) in JW and DM (e) Chemical composition  $X_i$  in JW. (f) Degeneracy parameter  $\Psi$  in JW (solid) and DM (dashed).

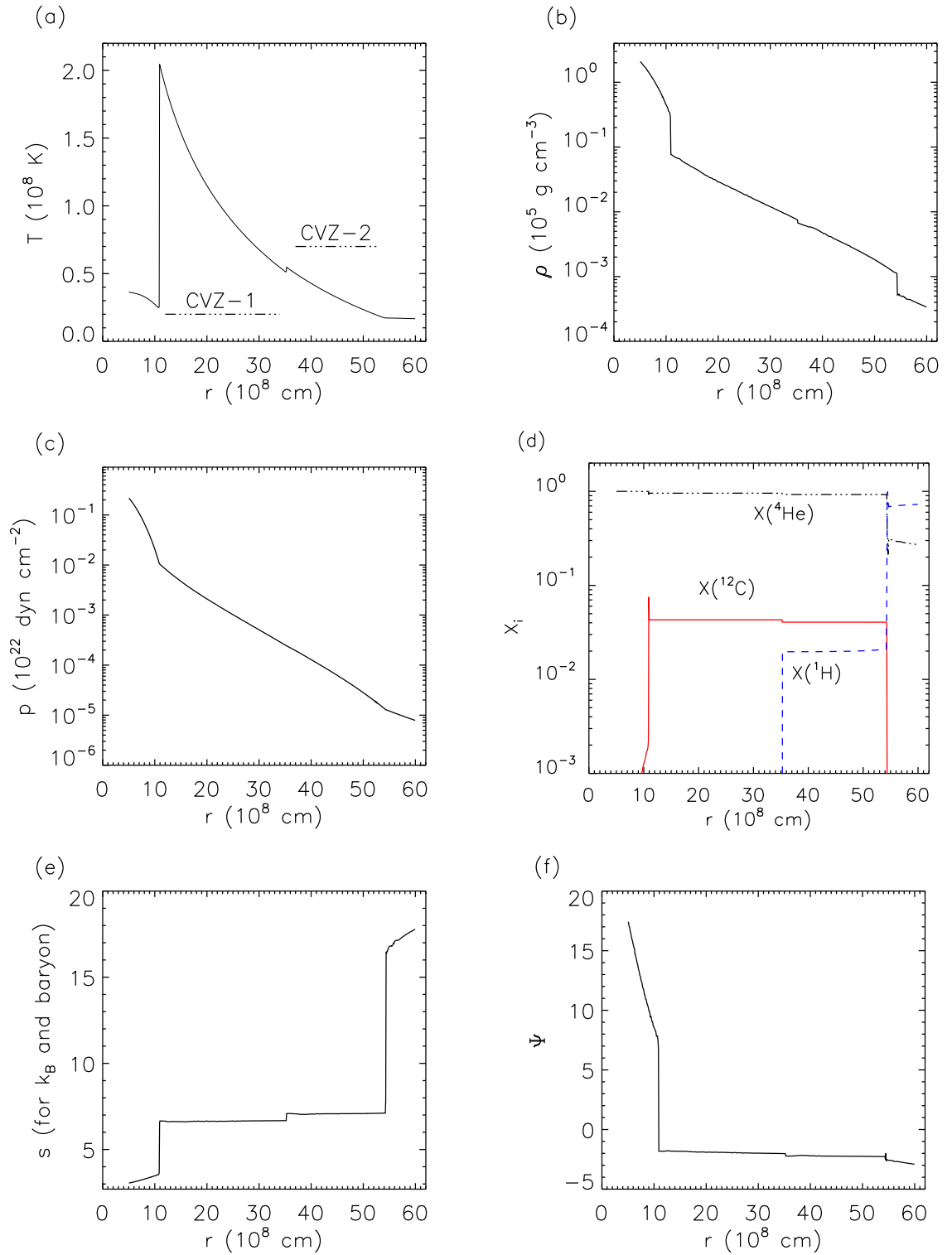


**Figure 5.3.:** The initial internal structure of the model SC as a function of radius. (a) Temperature  $T$  (solid) used as initial condition in the hydrodynamic simulations. CVZ marks the convection zone. (b) Density  $\rho$ , (c) Pressure  $p$ , (d) Chemical composition  $X_i$  (e) Entropy  $s$ , and (f) Degeneracy parameter  $\Psi$ .



# 6

## One-Dimensional Hydrodynamic Simulations

We performed several one-dimensional simulations using model M, which differed only in their grid resolution (see Table 6.1), to assess, whether a thermonuclear runaway could be avoided without a convective flow which can spontaneously appear only in two- and three-dimensional simulations.

### 6.1. Temporal Evolution

**Table 6.1.:** Some properties of the 1D simulations: number of radial grid points ( $N_r$ ), radial resolution ( $\Delta r$  in  $10^6$ cm), time up to the thermonuclear runaway,  $t_{trn}$ , and maximum evolution time  $t_{max}$  (both in s).

run	$N_r$	$\Delta r$	$t_{trn}$	$t_{max}$
hefl.1d.1	180	5.55	40 700	42 500
hefl.1d.2	270	3.77	14 600	16 250
hefl.1d.3	360	2.77	12 300	15 600

Figure 6.1 demonstrates that heat conduction and adiabatic expansion alone (*i.e.* no convection) fail to keep the model in hydrostatic equilibrium, *i.e.* one-dimensional hydrodynamic simulations result in a thermonuclear runaway. Initially, the maximum temperature increases only slowly, but starts to rise rapidly after a time  $t_{trn}$  (Table 6.1) up to a value  $T \sim 10^9$  K. For instance, from the temperature evolution of model hefl.1d.3, one can determine that a local hot spot with a temperature of  $2.3 \times 10^8$  K will runaway after about 80 s (Fig. 6.1). The time at which the runaway is triggered depends on the grid resolution, being longer in models with lower resolution (Fig. 6.1). In every case, a thermonuclear flame with  $T \sim 10^9$  K eventually forms and propagates outwards with subsonic velocity depending on the grid resolution. The layers passed by the flame expand *i.e.* pressure and density drops there (Fig. 6.1). A similar behavior was also observed in our one-dimensional simulations based on the initial models DM and JW. Since our two- and three- dimensional simulations, with convection triggering spontaneously, do not show such a behavior, we refrain from further discussion of the one-dimensional simulations.

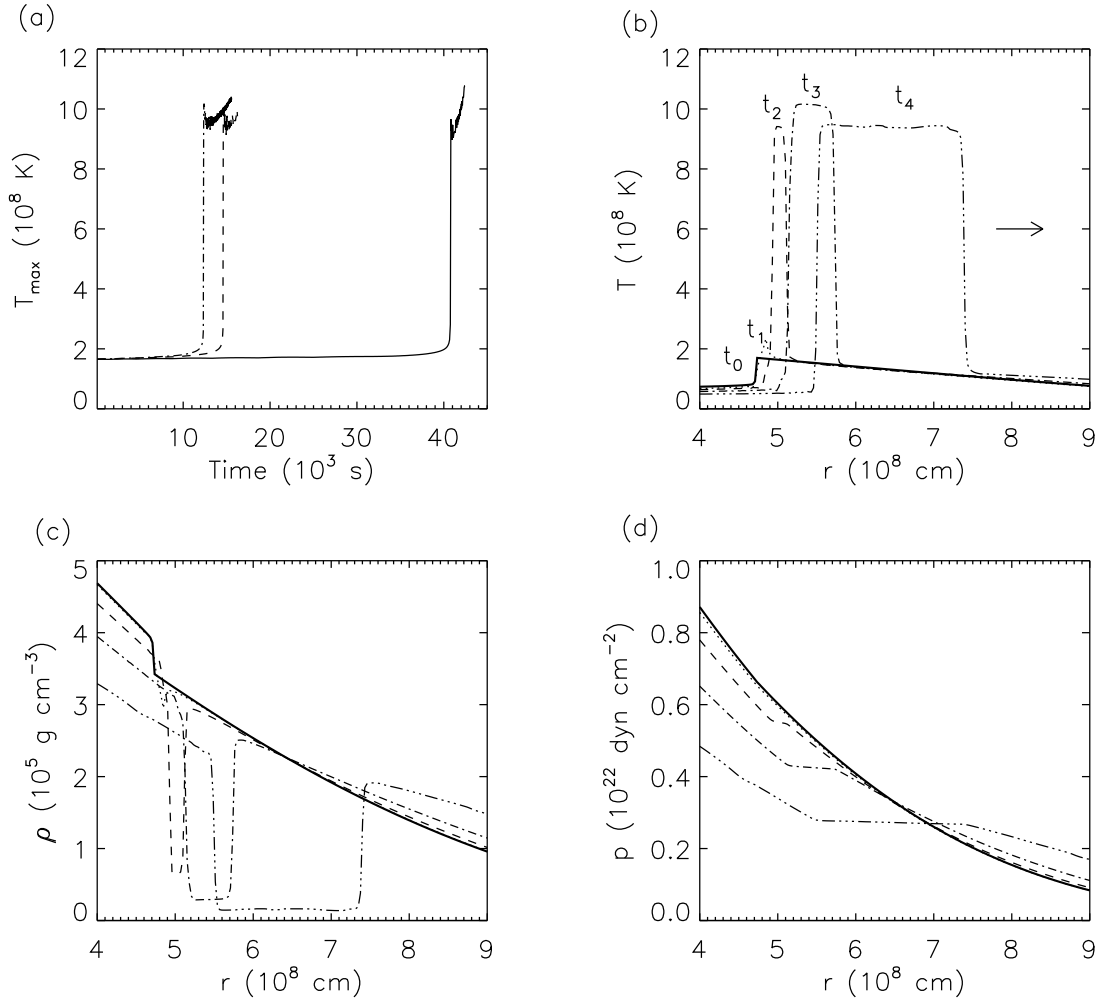


**Figure 6.1.:** (a) Evolution of the temperature maximum  $T_{max}$  in the one-dimensional models hefl.1d.1 (solid), hefl.1d.2 (dashed), and hefl.1d.3 (dash-dotted), respectively. Temperature  $T$  (b), density  $\rho$  (c) and pressure (d) stratification in the helium core of model hefl.1d.3 during the runaway at  $t_1 = 12\,270$  s (dotted),  $t_2 = 12\,352$  s (dashed),  $t_3 = 12\,392$  s (dash-dotted), and  $t_4 = 12\,762$  s (dash-dot-dotted), respectively. The solid line corresponds to the initial model ( $t_0$ ), and the arrow indicates the direction of the flame propagation.

# 7

## Two-Dimensional Hydrodynamic Simulations

In Table 7.1, we summarize some characteristic parameters of our two-dimensional (*i.e.* axisymmetric) simulations which are based on model M.

**Table 7.1.:** Some properties of the 2D simulations: number of grid points in radial ( $N_r$ ) and angular ( $N_\theta$ ) direction, radial ( $\Delta r$  in  $10^6$ cm) and angular grid resolution ( $\Delta\theta$ ), characteristic length scale  $l_c$  of the flow (in  $10^8$ cm), characteristic r.m.s velocity  $v_c$  of the flow (in  $10^6$  cm s $^{-1}$ ) averaged over the width of the convection zone  $R \sim l_c$ , Reynolds number  $R_n$  associated with the numerical viscosity of our code (Porter & Woodward 1994), damping timescale due to the numerical viscosity  $t_n$ , typical convective turnover time  $t_o = 2R/v_c$ , and maximum evolution time  $t_{max}$  (in s), respectively.

run	$N_r \times N_\theta$	$\Delta r$	$\Delta\theta$	$l_c$	$v_c$	$R_n$	$t_n$	$t_o$	$t_{max}$
hefl.2d.1	180×90	5.55	2°	4.7	1.29	1 900	11 000	730	30 000
hefl.2d.2	270×180	3.70	1°	4.7	1.79	8 900	36 000	525	30 000
hefl.2d.3	360×240	2.77	0.75°	4.7	1.84	21 000	83 000	510	130 000

We first discuss in some detail one specific simulation hefl.2d.3, which serves as a standard to which we compare the results of our other simulations. Thereafter, we discuss some general properties of all 2D simulations. Every simulation covered approximately  $3 \times 10^4$  s ( $\sim 8$  hrs) of the evolution near the peak of the core helium flash except of hefl.2d.3 which covered roughly 36 hrs. They were performed on an equidistant spherical grid encompassing 95% of the helium core mass ( $X(^4\text{He}) > 0.98$ ) except for a central region with a radius of  $r = 2 \times 10^8$  cm, which was removed in order to allow the use of longer timesteps. This radius is sufficiently smaller than the radius of the temperature inversion ( $r \sim 5 \times 10^8$  cm) and therefore its presence does not influence the convection zone. The used boundary conditions are in all directions reflective.

### 7.1. Temporal Evolution

After the beginning of the simulation, the initial velocity perturbations started to grow in a narrow layer just outside the temperature maximum ( $r \sim 5 \times 10^8$  cm), *i.e.* in the region heated

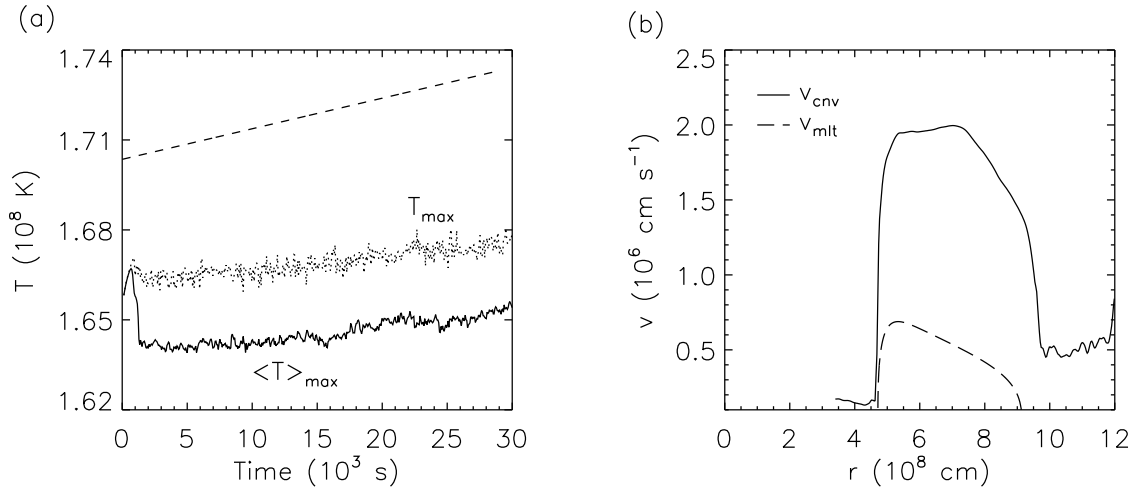


**Figure 7.1.:** (a) Temporal evolution of the horizontally averaged temperature maximum  $\langle T \rangle_{max}$  (solid), and of the global temperature maximum  $T_{max}$  (dotted) in model hefl.2d.3. The dashed line corresponds to the temporal evolution of the maximum temperature in the stellar evolutionary calculations of the model M. (b) The r.m.s convection velocity  $v_{cnv}$  in simulation hefl.2d.3 averaged over 6 000 s (solid) versus the convection velocity predicted by the mixing length theory  $v_{mlt}$  (dashed).

by nuclear burning. Later on at  $t \sim 800$  s, several hot bubbles appeared (Fig. 7.2, Fig. 7.3), which rose upwards with maximum velocities of  $\sim 4 \times 10^6$  cm s $^{-1}$ . They were typically about 0.2% hotter than the angular-averaged temperature at a given radius. The  $^4\text{He}$  mass fraction of all hot bubbles was about 0.4% less than the corresponding angular-averaged value, since helium was depleted in the bubbles by the triple  $\alpha$  reaction. Consequently,  $^{12}\text{C}$  and  $^{16}\text{O}$  (produced in helium burning) were enhanced by  $\sim 0.7\%$  in the bubbles.

During the first 700 s of the evolution, the off-center maximum mean temperature  $\langle T \rangle_{max}$  rose at a rate of  $\sim 1000$  K s $^{-1}$ , until it reached a value  $\sim 1.67 \times 10^8$  K. At this moment, from the region at the  $\langle T \rangle_{max}$ , the bubbles emerged and caused its decrease by  $\sim 2.6 \times 10^6$  K in just 570 s corresponding to a temperature drop rate of 4540 K s $^{-1}$  (Fig. 7.1). This phase marked the onset of convection (Fig. 7.2, Fig. 7.3), where a fraction of the thermonuclear energy released via helium burning started to be transported efficiently away from the burning regions by mass flow, thereby inhibiting a thermonuclear runaway.

As soon as the bubbles had formed, they rose upwards and started to interact and merge, *i.e.* the convective layer began to grow in radius. About  $\sim 1300$  s after the start of the simulation, the entire convection zone was covered by an almost stationary flow pattern of almost constant total kinetic energy roughly equal to  $10^{45}$  erg. At this time, vortices dominated the flow pattern. They extended across the entire convective region (width  $R \sim 2.2 H_p$ ), and were of approximately similar angular size, one vortex covering about 40 degrees (diameter  $\sim 5 \times 10^8$  cm). Usually we found about four such vortices with two dominant up-flows of hot gas at both  $\theta \sim 60^\circ$  and  $\theta \sim 120^\circ$  (see, *e.g.* Fig. 7.2). These large vortices were rather stable, surviving until the end of our simulations. Typical convective flow velocities were  $v_{cnv} \sim 1.8 \times 10^6$  cm s $^{-1}$ , well below the local sound speed  $c_s \sim 1.7 \times 10^8$  cm s $^{-1}$ , *i.e.* a vortex required about 500 s for one rotation. The persistence of vortices is not typical for turbulent convection and their dominance was a consequence of the imposed axial symmetry.

The Mach number  $M$  of the convective flow was  $\sim 0.01$ . Is PPM suited for this type of subsonic flow? This question, which is beyond the scope of the present study, needs to be investigated. It is known that the artificial viscosity of standard Riemann solver methods exhibit an incorrect



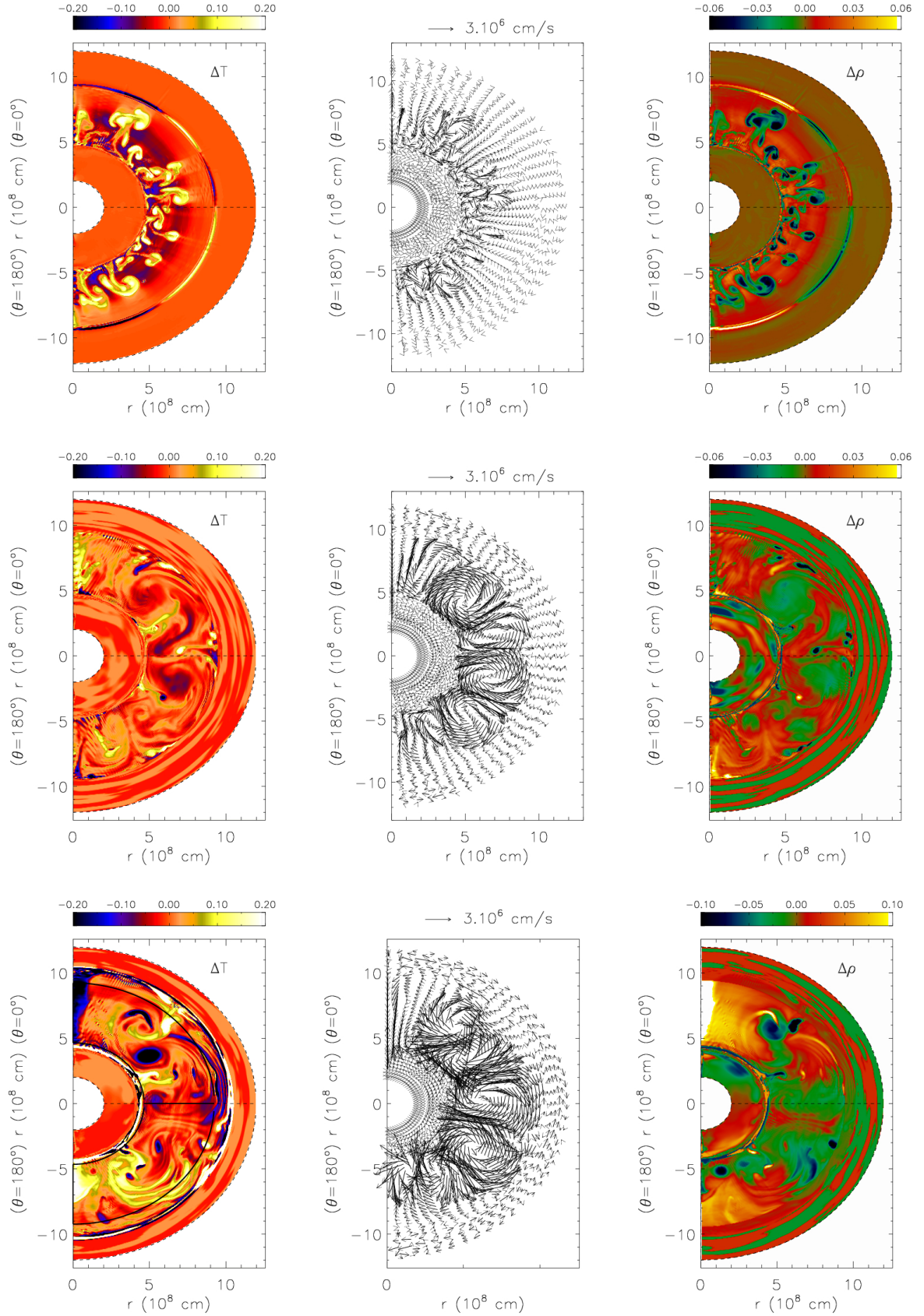


**Figure 7.2.:** Snapshots of the onset of convection at 1020 s (upper panels), and of the evolved convection (lower panels) in model hefl.2d.3 at 29 000 s (middle panels) and 120 000 s (bottom panels), showing the temperature contrast  $\Delta T = 100 \times (T - \langle T \rangle_\theta) / \langle T \rangle_\theta$  (left panels), the velocity field (middle panels), and the density contrast  $\Delta \rho = 100 \times (\rho - \langle \rho \rangle_\theta) / \langle \rho \rangle_\theta$  (right panels), respectively.  $\langle \rangle_\theta$  denotes a horizontal average at a given radius.

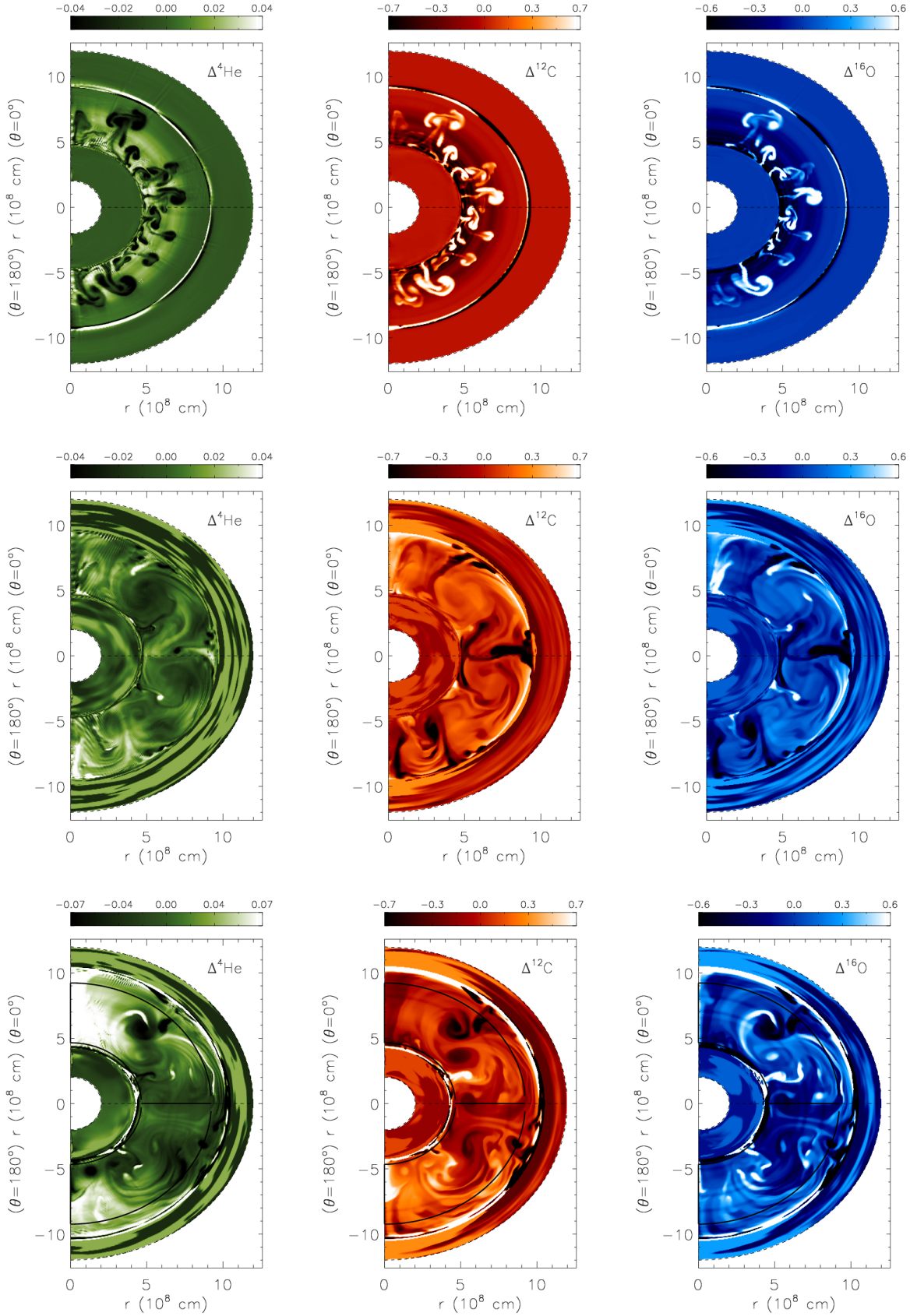


**Figure 7.3.:** Snapshots of the onset of convection at 1020 s (upper panels), and of the evolved convection (lower panels) in model hefl.2d.3 at 29 000 s (middle panels) and 120 000 s (bottom panels), showing the helium  ${}^4\text{He}$  contrast  $\Delta^4\text{He} = 100 \times ({}^4\text{He} - \langle {}^4\text{He} \rangle_\theta) / \langle {}^4\text{He} \rangle_\theta$  (left panels), the carbon  ${}^{12}\text{C}$  contrast  $\Delta^{12}\text{C} = 100 \times ({}^{12}\text{C} - \langle {}^{12}\text{C} \rangle_\theta) / \langle {}^{12}\text{C} \rangle_\theta$  (middle panels), and the oxygen  ${}^{16}\text{O}$  contrast  $\Delta^{16}\text{O} = 100 \times ({}^{16}\text{O} - \langle {}^{16}\text{O} \rangle_\theta) / \langle {}^{16}\text{O} \rangle_\theta$  (right panels), respectively.  $\langle \rangle_\theta$  denotes a horizontal average at a given radius.

scaling with the flow Mach number as  $M \rightarrow 0$  (Tukel 1999), *i.e.* the inherent artificial viscosity of PPM may be too high for simulating flows at low Mach numbers (*e.g.*  $M \sim 0.01$ ) adequately.

However, Meakin & Arnett (2007a) demonstrated that the PPM method operates well even at these low Mach numbers.

Energy transport by convection within the vortices is concentrated into a few narrow upward drafts, compensated partially, but only to a small extent, by down-flows. The vortices transport energy mostly along their outer edges. Matter in their centers does not interact at all with the regions of dominant nuclear energy production.

The horizontally averaged value of the maximum temperature, barring some additional temperature fluctuations due to convection, increased slightly following the onset of convection during the entire subsequent evolution at an approximate rate  $40 \text{ K s}^{-1}$  (see Fig. 7.1).

This rate appears to be about 60 % lower than the rate measured in the stellar evolutionary calculations ( $\sim 100 \text{ K s}^{-1}$ ): this could be the result of either an initially lower value of the temperature maximum, after the stabilization phase, at the beginning of the simulation (see Sect. 5.2), or more dynamic convective motion, since the mean convective velocities  $v_{cnv}$  exceed the velocities predicted by mixing length theory,  $v_{mlt}$ , on average by a factor of four (Fig. 7.1).

Convection distributes the energy in such a way that the temperature gradient  $\nabla$  never exceeds  $\nabla_{ad}$  significantly. Although, the value of  $\nabla$  established at the beginning of the simulation deviates slightly after some time from the gradient at later times, it remains close to the adiabatic temperature gradient  $\nabla_{ad}$  (the relative difference being less than 1%). In this respect, there is no indication of any significant deviation from the situation obtained in stellar evolutionary calculations.

The apparent spike in the initial  $^{12}\text{C}$  distribution at the location of the temperature maximum (Fig. 5.1) is a result of a non-instantaneous treatment of the convective mixing in stellar evolutionary calculations. It turns out that a non-instantaneous treatment of mixing is not required during the core helium flash since simulation hefl.2d.3 indicate that the spike is smeared out immediately after convection commences. This implies that the assumption of instantaneous mixing is a good approximation locally, despite the strong temperature dependence of the energy production rate.

## 7.2. Energy Fluxes

Figure 7.4 (a,b,c,d) displays the individual contributions of various energy fluxes, time-averaged over almost 12 convective turnover times (see Table 7.1), *i.e.* only the average effect of convection should be apparent. The derivation of these quantities is explained in Appendix A.2. All energy fluxes,  $F$ , describe the amount of energy transported per unit of time across a sphere of a given radius.

Most of the nuclear energy production in the convection zone occurs in a relatively narrow shell about the location of the temperature maximum. This energy is transported away by both convection and thermal transport due to heat conduction and radiation. The convective (or enthalpy) flux,  $F_C$ , varies from  $-0.2 \times 10^{42} \text{ erg s}^{-1}$  up to  $1.6 \times 10^{42} \text{ erg s}^{-1}$ . The kinetic flux,  $F_K$ , reaches a value of at most  $1 \times 10^{42} \text{ erg s}^{-1}$ , and is mostly positive in the convection zone, *i.e.* the motion has a predominantly upward direction. This implies that the fast, narrow, upwardly directed streams dominate over the slower and broader downward flows. The ratio of the extreme values of  $F_C$  and  $F_K$  is almost 2:1, *i.e.* nuclear energy is stored predominantly in the internal energy of the rising hot gas. Both convective and kinetic energy flux transport

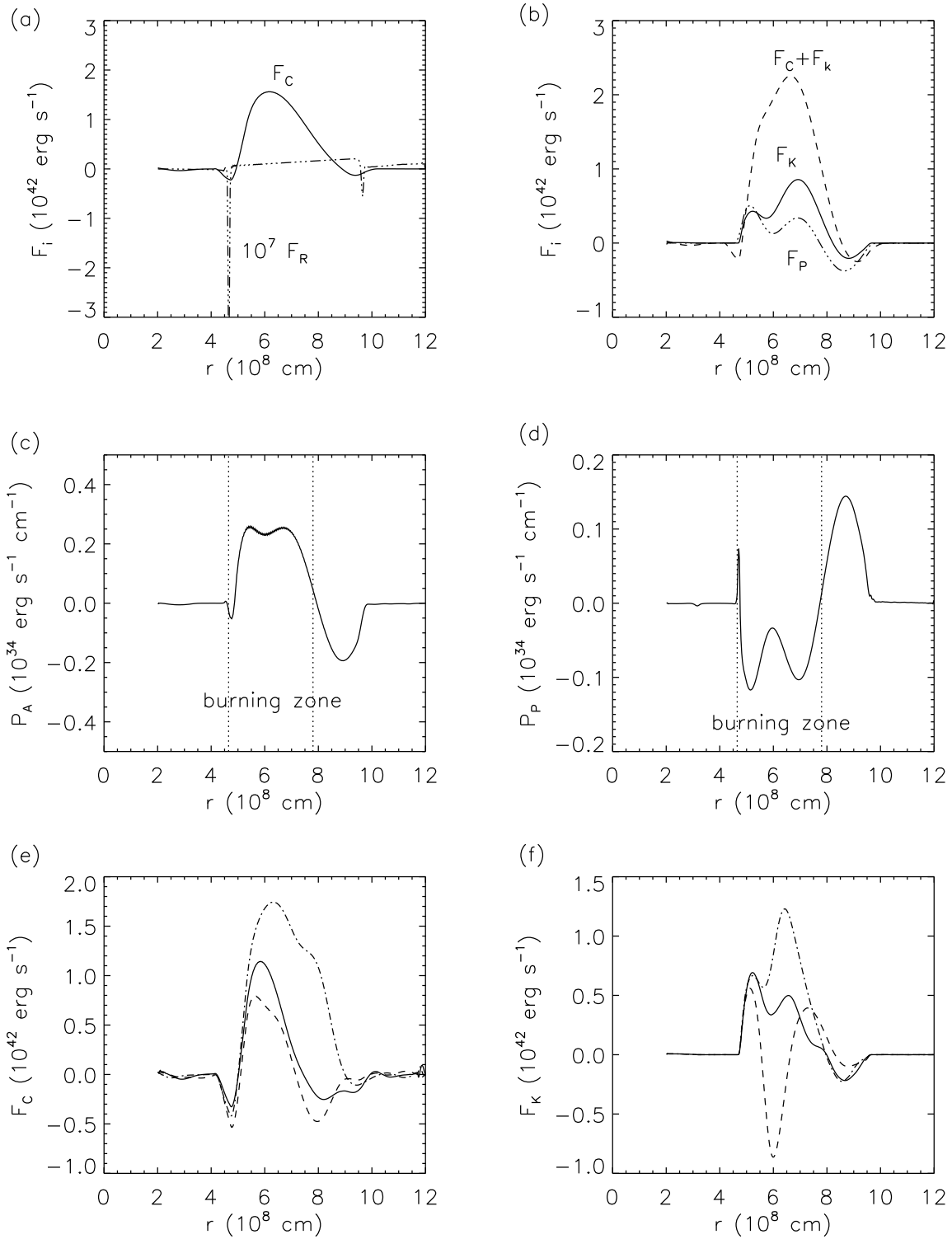


**Figure 7.4.:** Snapshots of various energy fluxes and source terms in model hefl.2d.3 (time averaged over 6 000 s or almost 12 convective turnover times, from  $t = 18\,000$  s to  $t = 24\,000$  s): (a) convective flux  $F_C$  (solid), and the energy flux due to the thermal transport  $F_R$  (dash-dotted); (b) kinetic flux  $F_K$  (solid), acoustic flux  $F_P$  (dash-dot-dotted), and sum of the kinetic and convective flux  $F_C + F_K$  (dashed); (c) source terms due to work done by buoyancy forces  $P_A$ , and (d) due to volume changes  $P_P$ . The vertical lines enclose the nuclear burning zone ( $T > 10^8$  K). Temporal evolution of the convective flux  $F_C$  (e) and kinetic flux  $F_K$  (f) where the snapshots were averaged over 200 s and at around  $t_1 = 19\,300$  s (solid),  $t_2 = 19\,500$  s (dashed) and  $t_3 = 19\,700$  s (dashed-dotted).



more than 90% of the generated nuclear energy upward through the convection zone, the value is dropping to zero towards its border. Part of the heat released in the nuclear processes is in fact transported downwards towards the inner edge of the temperature inversion. Almost none of the nuclear energy reaches the surface of the helium core, either by convection or by conduction, *i.e.* all the energy released is deposited within the core causing its expansion. Energy transport due to heat conduction and radiation is everywhere negligible compared with other contributions. The viscous flux,  $F_V$ , is negligible as well, and losses due to friction, influence only the dynamics significantly close to the borders of the convection zone (Achatz 1995).

The distribution of the kinetic and convective flux is during a single turnover of a vortex changing significantly (Fig. 7.4: e,f) due to the appearance of new hot streams of gas (Muthsam et al. 1995).

For completeness, we also consider the flux and source terms of the kinetic energy (see Appendix A.2), which allow us an additional insight into the operation of convection. The radial profile of the source term  $P_A$ , corresponding to the work done by buoyancy forces, indicates that the vertical convective flows are accelerated due to their density fluctuations in the entire region of dominant nuclear burning (burning zone) above  $T_{max}$ . Corresponding pressure fluctuations (causing expansion due to a pressure excess, respectively compression due to a pressure deficit) powered by the volume work  $P_P$  show that the gas within the burning region expands, which effectively again implies that an acceleration occurs. Due to the importance of  $P_P$  in the convection zone, the acoustic flux  $F_P$ , which transports pressure fluctuations, reaches a value comparable to that of the kinetic flux  $F_K$ , its value being negligible elsewhere.

### 7.3. Turbulent Entrainment

Turbulent entrainment (Fernando 1991; Meakin & Arnett 2007b), commonly referred to as overshooting, is a hydrodynamic process that permits mixing and heating in regions that are convectively stable according to the Schwarzschild or Ledoux criterion. Turbulent entrainment, *i.e.* penetration beyond the formal convective boundaries, occurs at both edges of the convection zone, and is driven by down-flows and up-flows. We study the entrainment by monitoring the temperature changes and the  $^{12}\text{C}$  concentration at the (formal) edges of the convection zone.  $^{12}\text{C}$  is the most suitable element for investigating the extent of convective mixing, because at the beginning of the simulations, it is mostly absent outside the convection zone, and therefore can be enhanced there only due to turbulent entrainment.

At  $t = 30\,000\text{ s}$  during simulation hefl.2d.3, the temperature inversion is located at  $r = 4.65 \times 10^8\text{ cm}$  (Fig. 7.5). It is therefore about 70 km closer to the center of the star than it was at the beginning of the simulation ( $4.72 \times 10^8\text{ cm}$ ). Its shape remains almost unchanged and discontinuous during the whole simulation, and its propagation speed<sup>1</sup> can be estimated from the heating rate  $\delta T/\delta t \sim 2760\text{ K s}^{-1}$  and the local gradient  $\delta T/\delta r \sim 12\text{ K cm}^{-1}$  at the steepest point of the inversion:

$$v \simeq -(\delta T/\delta t) / (\delta T/\delta r) \sim -2.3\text{ m s}^{-1} \quad (7.1)$$

This speed is significantly higher than the propagation speed due to heat conduction alone. We note that the energy flux carried by the heat conduction is seven orders of magnitude smaller than the energy flux carried by the convection. Assuming that the convective energy flux at the position of the temperature inversion ( $F_c \sim 0.2 \times 10^{42}\text{ erg s}^{-1}$ ) is used up completely to heat the layers beneath the temperature inversion, a typical heating rate of  $\dot{T} = \dot{E}/C_{inv} \sim 1250\text{ K s}^{-1}$

<sup>1</sup>The speed at which convective boundaries move due to turbulent entrainment is called entrainment rate.

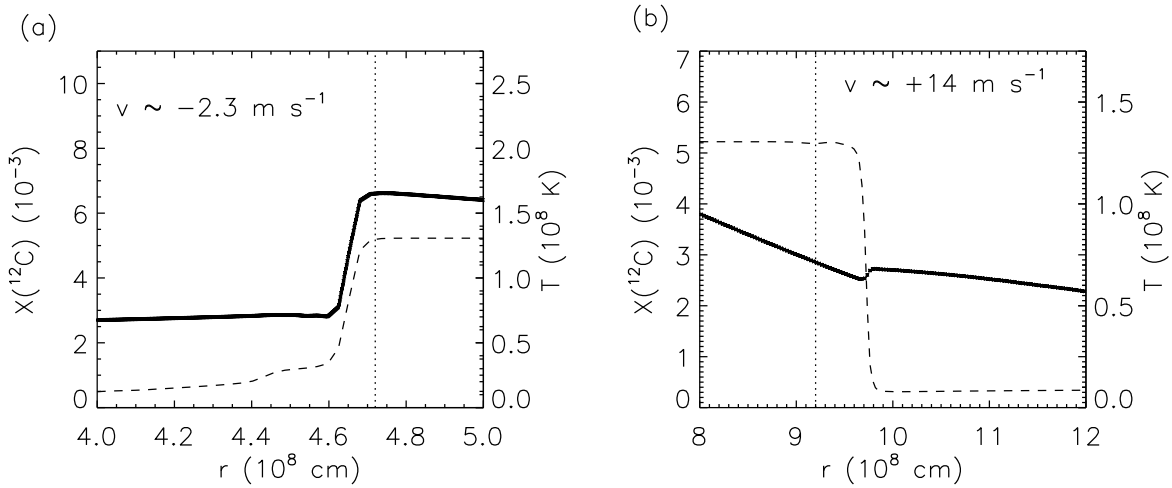


**Figure 7.5.:** Angular averaged  $^{12}\text{C}$  distribution (dashed) and temperature stratification (thick) at the inner (a) and outer edge (b) of the convection zone in model hefl.2d.3 at  $t = 30000 \text{ s}$ . The vertical dotted lines mark the initial boundaries of the convection zone at  $t = 0 \text{ s}$  determined by the Schwarzschild criterion.

can be derived, which is by roughly 50 % lower than the value inferred from the simulation.  $C_{inv}$ , the heat capacity of the layers including the temperature inversion is  $\sim 1.6 \times 10^{38} \text{ erg K}^{-1}$ .

This implies that turbulent entrainment leads to a strong heating of the inner neutrino-cooled center of the star that occurs on timescales relatively short compared with stellar evolutionary timescales. This heating was studied by both [Deupree & Cole \(1983\)](#) and [Cole et al. \(1985\)](#), who derived qualitatively similar results.

Assuming that the estimated propagation speed of the temperature inversion remains constant, it would reach the center of the helium core and lift the electron degeneracy there within 24 days. This scenario would exclude the occurrence of mini-flashes after the main core helium flash, which are observed in stellar evolutionary calculations (Fig. 1.1).

[Sweigart & Gross \(1978\)](#) found that in stars with higher mass and helium abundance, the flash occurs closer to their center, which implies that in these stars can the temperature inversion reach the center of the helium core due to the turbulent entrainment even faster.

We also found that turbulent entrainment influenced the outer boundary of the convection zone. In the initial model, this boundary was located at  $r = 9.2 \times 10^8 \text{ cm}$  and corresponded to a discontinuous change in the distribution of elements (Fig. 5.1), which is in stellar evolutionary models a consequence of the assumption of the instantaneous mixing. In these models, all species in the convectively unstable region are mixed instantaneously across the entire convection zone, while the regions that are assumed to be convectively stable do not experience any mixing at all.

The distribution of  $^{12}\text{C}$  at  $t = 30\,000 \text{ s}$  is depicted in Fig. 7.5. Compared with that of the initial model, there is a clear shift of the carbon discontinuity, at the outer edge of the convection zone, to a larger radius ( $r = 9.7 \times 10^8 \text{ cm}$ ). In hydrodynamic simulations, the gas overshoots naturally from the convectively unstable to the formally convectively stable region because of its inertia. At the boundaries of the convection zone, the overshooting appears to destroy the stability, according to the Schwarzschild criterion, transforming the originally convectively stable region into a convectively unstable one. This allows the boundary to propagate further when a subsequent load of gas will try to overshoot at a later time. We estimated that the propagation

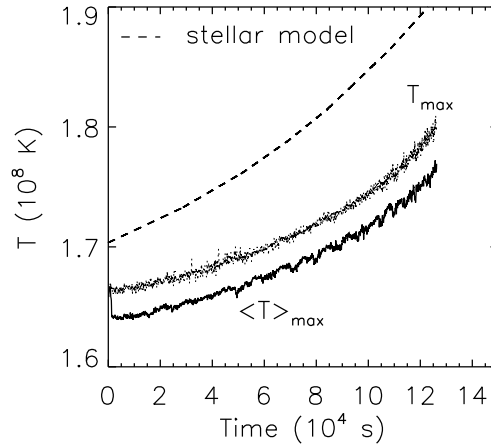


**Figure 7.6.:** Temporal evolution of the horizontally averaged temperature maximum  $\langle T \rangle_{max}$  (solid), and of the global temperature maximum  $T_{max}$  (solid thin) in the long-term 2D model hefl.2d.3. The dashed line corresponds to the temporal evolution of the maximum temperature in the stellar evolutionary calculation.

speed of the outer boundary of the convection zone is about  $14 \text{ m s}^{-1}$ . With a propagation speed of this magnitude, the convection zone would reach the hydrogen-rich layers surrounding the helium core (Fig. 1.2) at a radius  $r = 1.9 \times 10^9 \text{ cm}$  and trigger a hydrogen injection flash (Schlattl et al. 2001) within 10 days. Hydrodynamic phenomena expected due to the extra hydrogen mixing into the helium burning shell via this extended convection zone could alter the structure of the star significantly. Additional nucleosynthesis could also be triggered because hydrogen entrainment will result in a production of neutrons and possibly also in a production of s-process elements.

The hydrogen injection flash in Pop I stars is in contradiction with the canonical stellar evolutionary calculations where stars fail to inject hydrogen to the helium core during the core helium flash, unless their metallicity is close to zero (Fujimoto et al. 1990).

## 7.4. Long-Term Evolution

In the following we describe the long-term evolution of model hefl.2d.3, whose early evolution was discussed in detail in previous Sect. 7.1, 7.2, 7.3.

The model is characterized by a very dynamic flow involving typical convective velocities of  $\sim 1.8 \times 10^6 \text{ cm s}^{-1}$ . Our long-term hydrodynamic simulation of this model covering 36 hrs (see Fig. 7.6) has revealed that the global and angle-averaged maximum temperatures continue to rise at the initial rate of  $40 \text{ K s}^{-1}$  that is 60% lower than the rate predicted by stellar evolutionary calculations. As a consequence, the typical convective velocities increase by about 50% and reach a level of  $2.8 \times 10^6 \text{ cm s}^{-1}$  at the end of the simulation (Fig. 7.7).

Hydrodynamic simulations of convection driven by nuclear burning covering several convective turnover times show a rapid growth of the convection zone due to the turbulent entrainment (Meakin & Arnett 2007b). An analysis of our simulations based on a tracing of the radial position of the convective boundaries (defined by the condition  $X(^{12}\text{C}) = 2 \times 10^{-3}$ ; see Sect. 7.3), shows a similar behavior. Turbulent motion near the upper edge of the convection zone pumps material into the convectively stable layer at an entrainment rate of  $14 \text{ m s}^{-1}$  without any significant

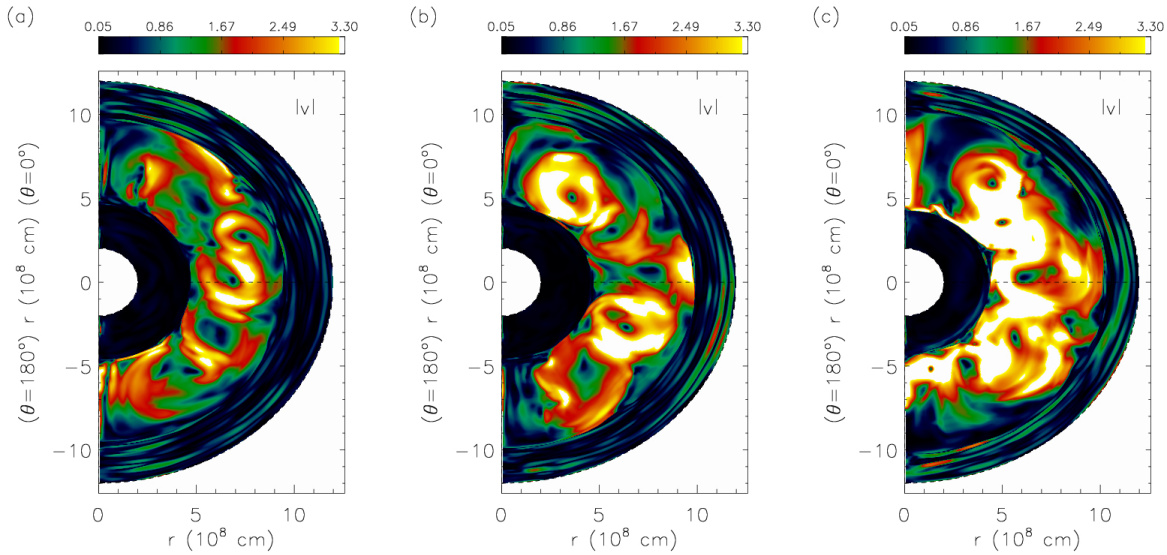


**Figure 7.7.:** Snapshots of the spatial distribution of the velocity modulus  $|v|$  (in units of  $10^6 \text{ cm s}^{-1}$ ) for the 2D model *hefl.2d.3* at 24 000 s (a), 60 000 s (b), and 120 000 s (c), respectively.

slowdown over the whole duration of the simulation (Fig. 7.8) covering  $\sim 130\,000$  s (or more than 250 convective turnover timescales). The entrainment rate at the inner convective boundary is about a factor of six smaller ( $2.3 \text{ m s}^{-1}$ ) slightly increasing during the second half of the simulation ( $t > 60\,000$ ; see Fig. 7.8). These entrainment rates have to be considered as upper limits because of the imposed axisymmetry which leads to exaggerated convective velocities and large filling factors for the penetrating plumes. The turbulent entrainment causes a growth of the convection zone on a dynamic timescale, in agreement with the hydrodynamic models of oxygen shell burning of Meakin & Arnett (2007b).

Both interfaces at the edges of the convection zone remain sharp during the whole length of the simulation (Fig. 7.8). The entrainment is correlated with a decrease of the temperature at the outer edge of the convection zone due to the decreasing entropy (Fig. 7.8). At the inner edge of the convection zone the entrainment leads to heating of the cold region at  $r < 4.72 \times 10^8 \text{ cm}$  that is cooled by neutrinos (Fig. 7.8). Contrary to the finding of Asida & Arnett (2000), the heating does not penetrate deeper into the star than the mixing of  $^{12}\text{C}$  and the other nuclear ashes.

Due to the growth of the convection zone and due to nuclear burning the mean  $^{12}\text{C}$ ,  $^4\text{He}$ , and  $^{16}\text{O}$  mass fractions change in the convection zone at rates listed in Table 7.2. The mean value of the  $^{12}\text{C}$  mass fraction in the convection zone decreases at a rate of  $-7.4 \times 10^{-9} \text{ s}^{-1}$  until  $t = 40\,000$  to a value of  $X(^{12}\text{C}) = 5.2 \times 10^{-3}$ . Then it begins to increase again at roughly the same (absolute) rate  $+7.7 \times 10^{-9} \text{ s}^{-1}$ . The  $^{12}\text{C}$  mass fraction decreases, because the volume of the convection zone grows initially almost discontinuously due to the sudden start of the entrainment. Hence, nuclear reactions are for a start unable to produce enough carbon to compensate for the volume increase. At  $t \sim 110\,000$  s the  $^{12}\text{C}$  mass fraction has risen again to its initial value of  $X(^{12}\text{C}) = 5.5 \times 10^{-3}$ , and at the end of the simulation at  $t = 130\,000$  s the  $^{12}\text{C}$  mass fraction is  $5.9 \times 10^{-3}$ , a value that is 7% higher than the initial one.

The mean  $^{16}\text{O}$  mass fraction shows a similar trend as that of  $^{12}\text{C}$  as its production depends directly on the  $^{12}\text{C}$  mass fraction. The mass fraction of  $^4\text{He}$  rises within the first 40 000 s because convection is dredging up fresh  $^4\text{He}$  from the convectively stable layers. Later in the evolution the mass fraction of  $^4\text{He}$  decreases at rate  $7.85 \times 10^{-9} \text{ s}^{-1}$ , as it is being constantly burned.



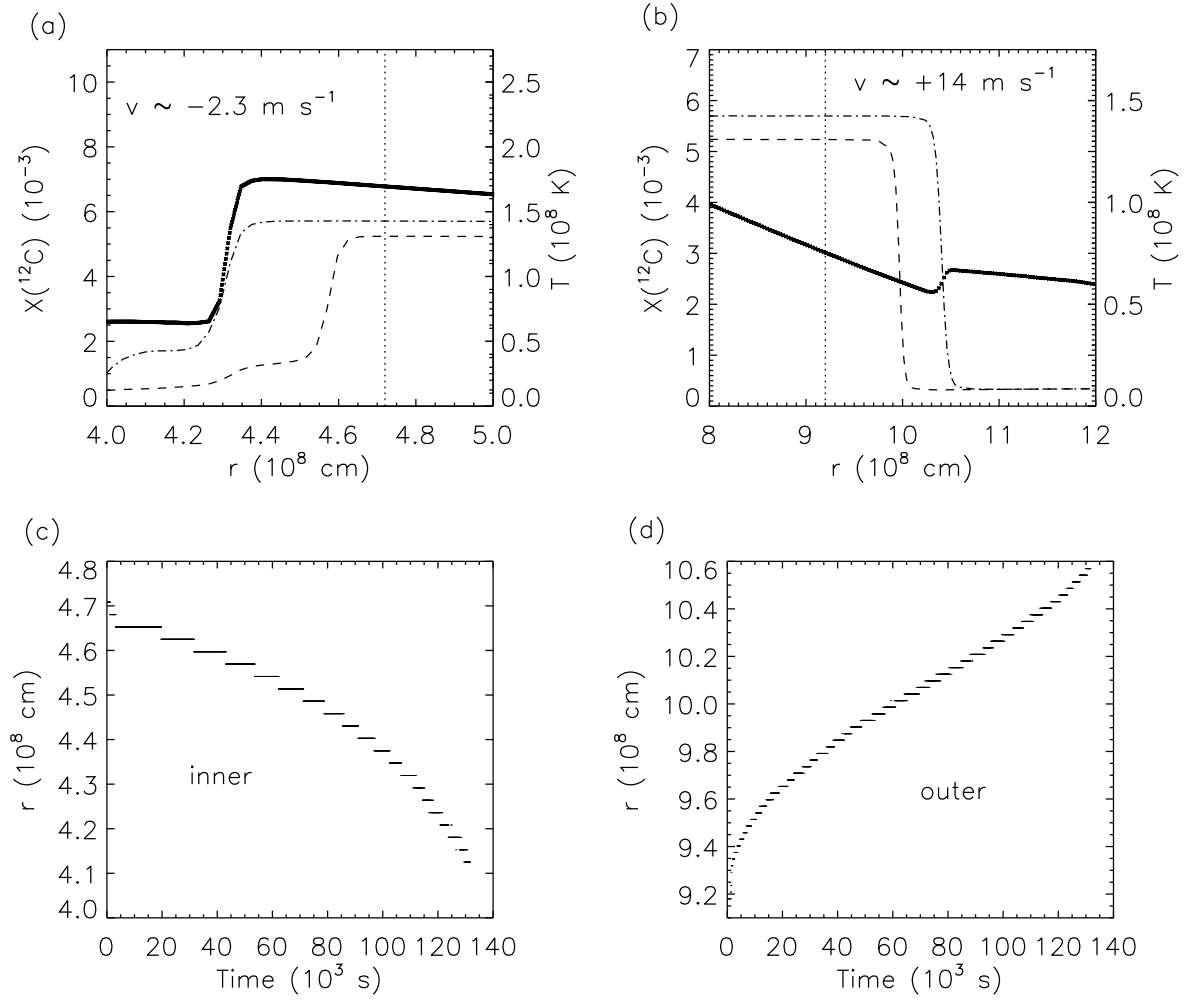


**Figure 7.8.:** *Upper panels:* Angular averaged  $^{12}\text{C}$  mass fraction as a function of radius near the inner (a) and outer edge (b) of the convection zone in the long-term 2D model hefl.2d.3 at  $t = 60\,000$  s (dashed) and  $t = 120\,000$  s (dash-dotted), respectively, and temperature stratification (thick) at  $t = 120\,000$  s. The vertical dotted lines mark the boundaries of the convection zone at  $t = 0$  s. *Bottom panels:* Temporal evolution of the position of the inner (c) and outer (d) edge of the convection zone in model hefl.2d.3, respectively.

**Table 7.2.:** Approximate rates at which the mean mass fractions of  $^4\text{He}$ ,  $^{12}\text{C}$ , and  $^{16}\text{O}$  evolve in the long-term 2D model hefl.2d.3 in the convection zone within the first  $40\,000$  s ( $R_i$ ; in units of  $10^{-9}$ ), and within the time interval  $40\,000$  s to  $130\,000$  s ( $R_f$ ; in units of  $10^{-9}$ ), respectively. The quantities  $X_i$  and  $X_f$  give the initial ( $t = 0$  s) and final ( $t = 130\,000$  s) mass fraction of  $^4\text{He}$  and mass fractions of  $^{12}\text{C}$ , and  $^{16}\text{O}$  abundances (in units of  $10^{-3}$ ), respectively.

element	$R_i$	$R_f$	$X_i$	$X_f$
$^4\text{He}$	+7.74	-7.85	0.975	0.974
$^{12}\text{C}$	-7.41	+7.71	5.502	5.918
$^{16}\text{O}$	-0.58	+1.13	0.927	1.008

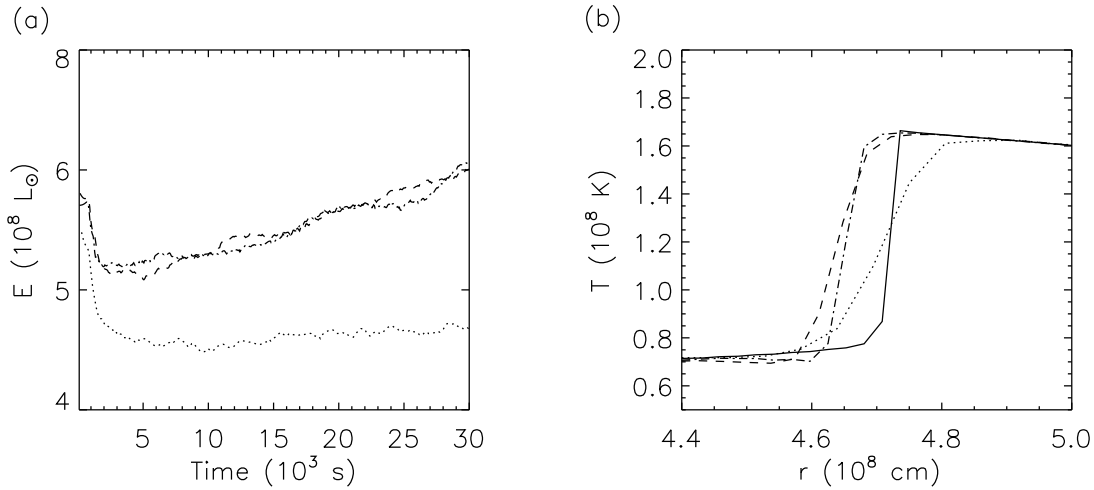


**Figure 7.9.:** (a) Evolution of the total energy production rate in solar luminosity  $L_\odot$  for models hefl.2d.1 (dotted), hefl.2d.2 (dashed), and hefl.2d.3 (dash-dotted), respectively. (b) Mean temperature distribution near the temperature inversion for models hefl.2d.1 (dotted), hefl.2d.2 (dashed), and hefl.2d.3 (dash-dotted) at a  $t = 30\,000$  s, respectively. The initial distribution is shown by the solid line.

## 7.5. Simulations with Different Resolution

We found only minor differences between the properties of model hefl.2d.3 and those of the corresponding models computed with a different grid resolution.

First, the initial mapping process generated different interpolation errors for different grid resolutions. However, the major source of discrepancy in this phase of the calculation was the stabilization itself. The iterative procedure that we used to retain the model in hydrostatic equilibrium (see Sect. 5.2) tends to decrease the temperature stronger in models of lower resolution.

Another source of discrepancy was caused by numerical diffusion, which is obviously stronger in models of lower resolution. Therefore, model hefl.2d.1 suffered more from numerical diffusion than either model hefl.2d.2 or hefl.2d.3, which is evident from Fig. 7.9. The temperature inversion, that is almost discontinuous at the beginning, is smoothed out faster in model hefl.2d.1. We note, that the temperature inversion is situated at smaller radii in models of higher resolution, since the typical flow velocities are higher in better resolved models (Table 7.1), *i.e.* the turbulent entrainment is more effective, and the temperature inversion propagates at higher speed.

Nevertheless, models hefl.2d.2 and hefl.2d.3 appear to be well resolved as differences between them are minor. The temporal evolution in their total nuclear energy production rates, for instance, are in almost perfect agreement (Fig. 7.9). The temperature fluctuations in the two-dimensional models are suppressed stronger in models of higher resolution. More intense temperature fluctuations observed in models which we calculated with grid resolutions even lower than that of the model hefl.2d.1, did not lead to an explosion.

## 7.6. Other Two-Dimensional Simulations

In order to assess the validity of our previous conclusions we performed a set of hydrodynamical simulations based on the initial models of different stars (Sect. 5, Tab. 5.1). The models are the same as those used in past by Cole & Deupree (1981) (model DM) and by Kurt Achatz (Achatz

**Table 7.3.:** Some properties of the 2D simulations based on initial model DM: number of grid points in radial ( $N_r$ ) and angular ( $N_\theta$ ) direction, radial ( $\Delta r$  in  $10^6$ cm) and angular grid resolution ( $\Delta\theta$ ), characteristic length scale  $l_c$  of the flow (in  $10^8$ cm), characteristic r.m.s velocity  $v_c$  of the flow (in  $10^6$  cm s $^{-1}$ ) averaged over the width of the convection zone  $R \sim l_c$ , Reynolds number  $R_n$  associated with the numerical viscosity of our code (Porter & Woodward 1994), damping timescale due to the numerical viscosity  $t_n$ , typical convective turnover time  $t_o = 2R/v_c$ , and maximum evolution time  $t_{max}$  (in s), respectively.

run	$N_r \times N_\theta$	$\Delta r$	$\Delta\theta$	$l_c$	$v_c$	$R_n$	$t_n$	$t_o$	$t_{max}$
hefl.2d.dm1	180×90	7.68	2°	8.7	5.05	11 500	25 100	344	47 800
hefl.2d.dm2	270×180	5.13	1°	8.7	5.56	42 600	84 400	313	38 800

1995) (model JW). Model SC belongs to a special category of models, atypical for the canonical core helium flash (Campbell & Lattanzio 2008).

All simulations were performed on equidistant spherical grid where the central part was removed to avoid the CFL restriction near the origin of the grid. To avoid possible numerical biases at the vicinity of the temperature inversion, the radius of the removed central part was chosen to be always smaller than that of the temperature inversion.

### 7.6.1. Model DM

In Table 7.3, we summarize some characteristic parameters of our two-dimensional simulations which are based on model DM. The simulations covered 48 000 s and 39 000 s, respectively. The grid covers a region, that in radius ranges from  $1.5 \times 10^8$  cm till  $1.5 \times 10^9$  cm and encompasses the convection zone which is roughly 3.3 pressure and 1.8 density scale heights wide. The inner boundary is located by  $3.5 \times 10^8$  cm beneath the temperature inversion, that is located at radius  $\sim 4.1 \times 10^8$  cm. The applied boundary conditions are always reflective. We will describe here only model hefl.2d.dm2 that has the highest resolution. The differences to model hefl.2d.dm1 having a lower resolution are minor.

The qualitative temporal evolution is similar to that of model hefl.2d.3 (Sect. 7.1). During the initial phase, temperature fluctuations grow mainly around the temperature maximum. Convection sets in at  $\sim 200$  s, and is characterized by the appearance of several hot bubbles being roughly by 1 % hotter than their environment (Fig. 7.10), and having  $^{12}\text{C}$  and  $^{16}\text{O}$  underabundant (Fig. 7.11) due to triple- $\alpha$  burning. After the onset of convection the model is characterized by a stable subsonic flow with typical velocities of around  $5 \times 10^6$  cm s $^{-1}$  (sound speed  $c_s \sim 1.7 \times 10^8$  cm s $^{-1}$ ). Therefore, one vortex which has typically radius equal to the height of the convection zone ( $\sim 8.7 \times 10^8$  cm) needs about 350 s for one rotation. This values are in good agreement with those obtained from models with lower resolution in the work of Achatz (1995).

During this phase, the maximum temperature rises steadily at an almost constant rate of 300 K s $^{-1}$  until the end of the simulation ( $t = 48\,000$  s) without any indications for thermonuclear runaway. In contradiction to the hydrodynamic simulations of Cole & Deupree (1980, 1981) based on the same initial model, we did not observe any thermal pulses which were characterized in their models by a steep increase of maximum temperature, *e.g.* at  $t = 26\,000$  s and at  $38\,000$  s from  $1.8 \times 10^8$  K up to  $2.1 \times 10^8$  K and back within roughly 5000 s intervals.

The energy fluxes in the convection zone (Fig. 7.12) have show a similar radial dependence than those in the model hefl.2d.3, *i.e.* the kinetic and convective flux are mostly positive implying fast and hot updrafts that dominate the transport of energy. The work done by buoyancy is positive,

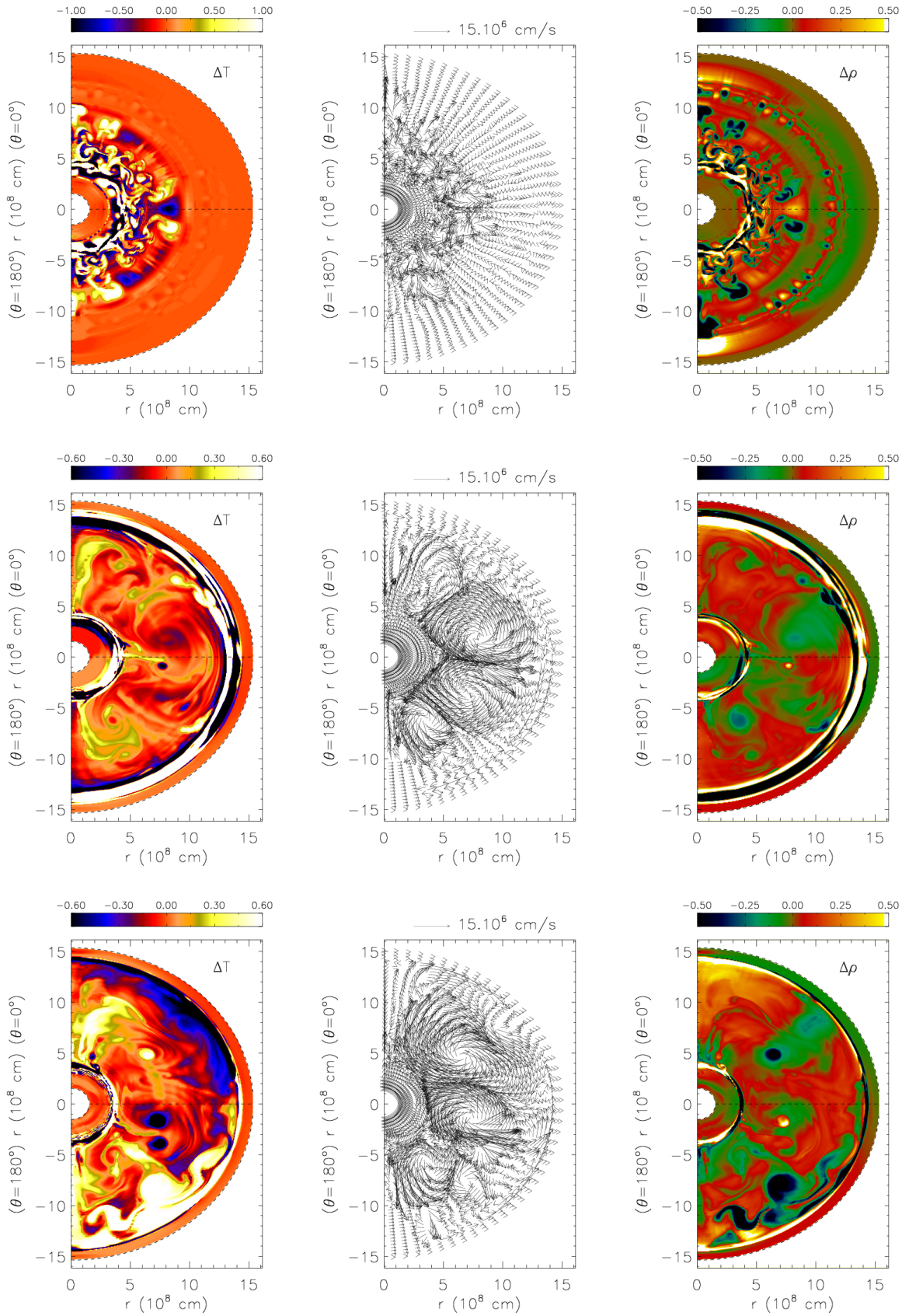


**Figure 7.10.:** Snapshots of the onset of convection at 220 s (upper panels), and of the evolved convection (lower panels) in model hefl.2d.dm2 at 540 s (middle panels) and 26 700 s (bottom panels), showing the temperature contrast  $\Delta T = 100 \times (T - \langle T \rangle_\theta) / \langle T \rangle_\theta$  (left panels), the velocity field (middle panels), and the density contrast  $\Delta \rho = 100 \times (\rho - \langle \rho \rangle_\theta) / \langle \rho \rangle_\theta$  (right panels), respectively.  $\langle \rangle_\theta$  denotes a horizontal average at a given radius.

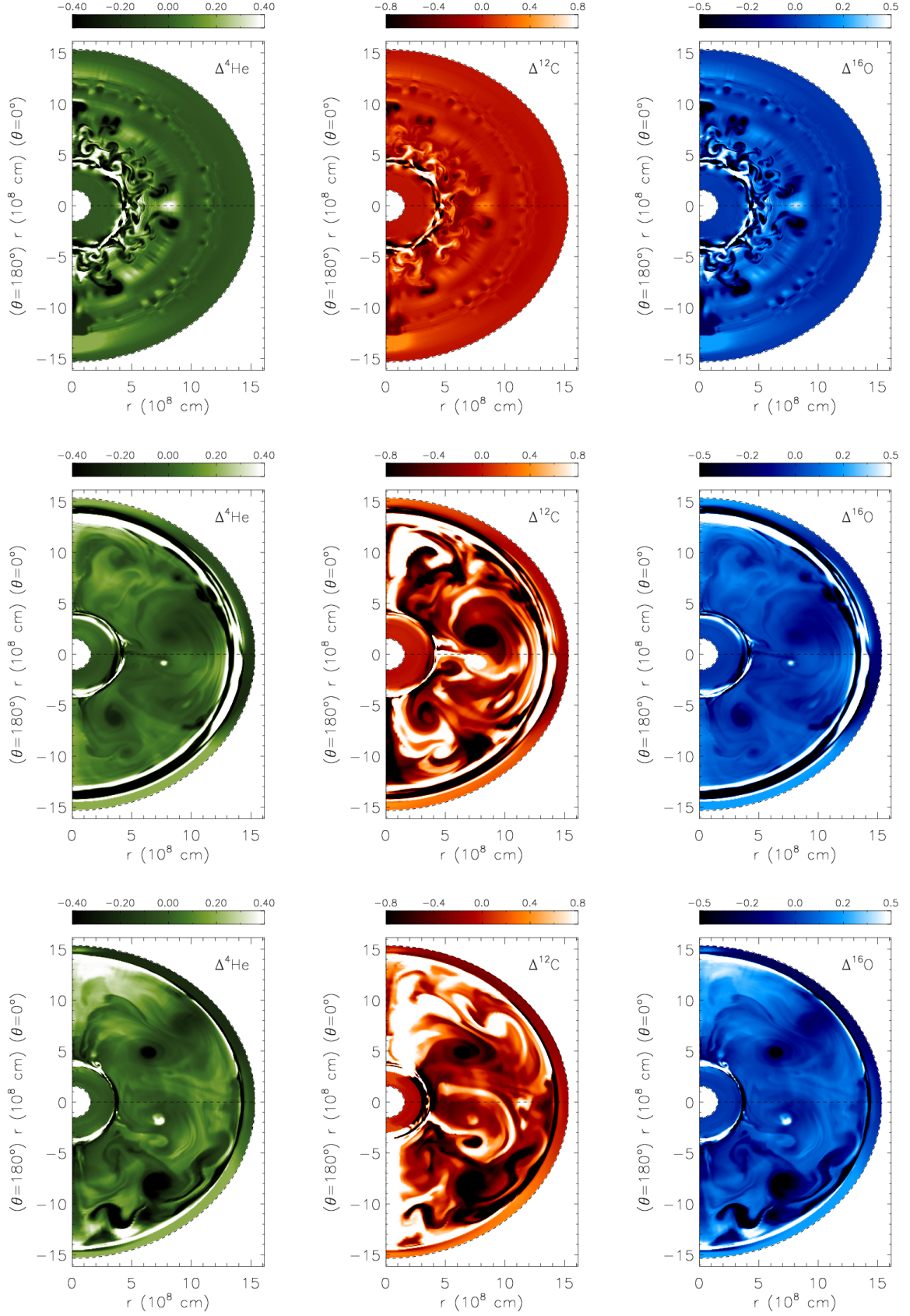


**Figure 7.11.:** Snapshots of the onset of convection at 220 s (upper panels), and of the evolved convection (lower panels) in model hefl.2d.dm2 at 540 s (middle panels) and 26 700 s (bottom panels), showing the helium  ${}^4\text{He}$  contrast  $\Delta^4\text{He} = 100 \times ({}^4\text{He} - \langle {}^4\text{He} \rangle_\theta) / \langle {}^4\text{He} \rangle_\theta$  (left panels), the carbon  ${}^{12}\text{C}$  contrast  $\Delta^{12}\text{C} = 100 \times ({}^{12}\text{C} - \langle {}^{12}\text{C} \rangle_\theta) / \langle {}^{12}\text{C} \rangle_\theta$  (middle panels), and the oxygen  ${}^{16}\text{O}$  contrast  $\Delta^{16}\text{O} = 100 \times ({}^{16}\text{O} - \langle {}^{16}\text{O} \rangle_\theta) / \langle {}^{16}\text{O} \rangle_\theta$  (right panels), respectively.  $\langle \rangle_\theta$  denotes a horizontal average at a given radius.



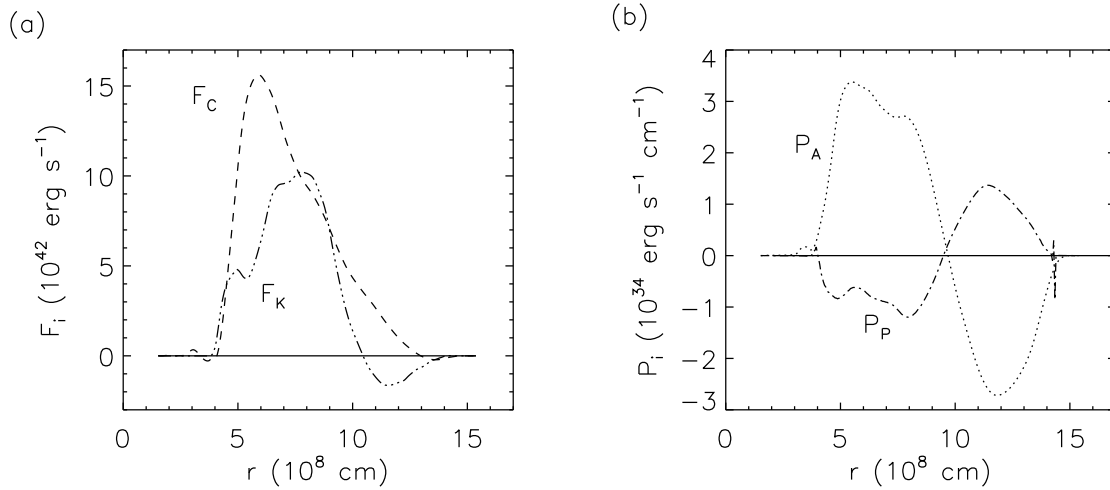


**Figure 7.12.:** Snapshots of various energy fluxes and source terms in model hefl.2d.dm2 (time averaged over 10000 s or almost 32 convective turnover times, from  $t = 13000$  s to  $t = 23000$  s): (a) convective flux  $F_C$  (dashed), and the kinetic energy flux (dash-dotted); (b) source terms due to work done by buoyancy forces  $P_A$  (dotted), and due to volume changes  $P_P$  (dash-dotted).

and the work done by expansion negative in most of the convection zone, *i.e.* the convective elements are accelerated along most of their path across the convection zone. Snapshots of the convective flow (Fig. 7.10, Fig. 7.11) show that it is more irregular and not as stable as the pattern seen for instance in the simulation hefl.2d.3 based on the model M.

The speed of the temperature inversion due to the turbulent entrainment is in a good agreement with the work of Achatz (1995). It can be estimated from the heating rate  $\delta T/\delta t \sim 7100$  K  $s^{-1}$  and the local gradient  $\delta T/\delta r \sim 4.8$  K  $cm^{-1}$  at the steepest point of inversion:  $v \simeq -(\delta T/\delta t) / (\delta T/\delta r) \sim 14.8$  m  $s^{-1}$ .

The energy generation rate in this model is the highest of all models we computed. At the position of the temperature maximum, the energy generation rate is 7 times higher than in model hefl.2d.3 and 8 times higher than in model hefl.2d.jw2 described in the next Sect. 7.6.2. The rate agrees very well with that of Achatz (1995).

### 7.6.2. Model JW

In Table 7.4, we summarize some characteristic parameters of our two-dimensional simulations which are based on model JW. The simulations covered 9000 s and were computed on a grid that spans from  $2 \times 10^8$  cm to  $2.3 \times 10^9$  cm and covers the convection zone which is 6 pressure and 3 density scale heights wide. The applied boundary conditions are reflective. In the following we describe only model hefl.2d.jw2, that has the highest grid resolution.

Convection starts at  $\sim 1000$  s and soon after it relaxes into a stable pattern characterized by a few upstreams or sometimes by only one major upstream of hot gas (Fig. 7.13, Fig. 7.14). The temperature maximum drops until around 2500 s at a rate  $1700$  K  $s^{-1}$  and staying almost constant afterward. After 4000 s, the temperature maximum is dropping again at the rate of  $700$  K  $s^{-1}$ .

The temperature inversion gets only smeared during the simulation and practically does not move further to the center as observed for instance in model hefl.2d.3. It implies that this model

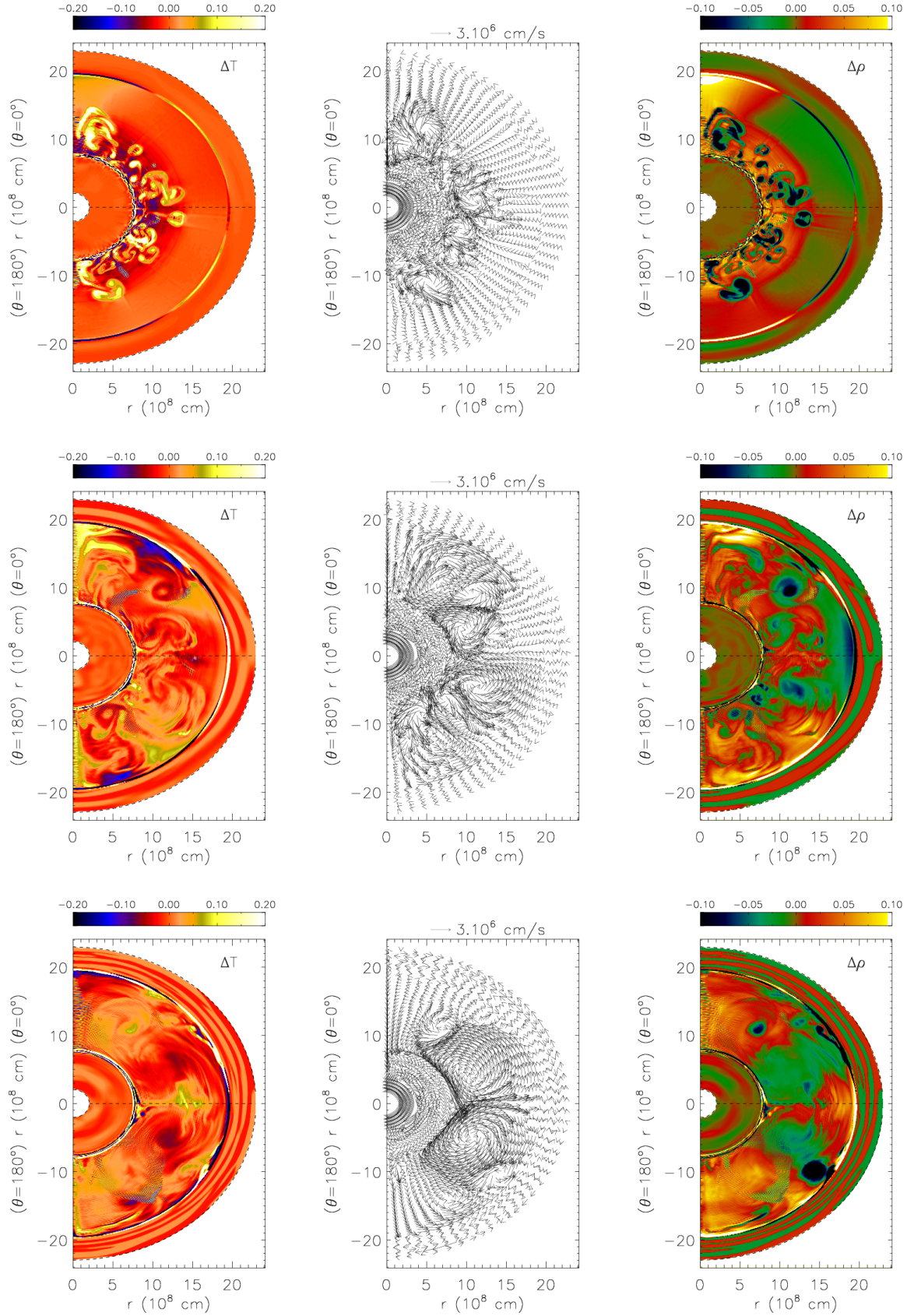


**Figure 7.13.:** Snapshots of the onset of convection at 1 200 s (upper panels), and of the evolved convection (lower panels) in model hefl.2d.jw2 at 1 900 s (middle panels) and 6 600 s (bottom panels), showing the temperature contrast  $\Delta T = 100 \times (T - \langle T \rangle_\theta) / \langle T \rangle_\theta$  (left panels), the velocity field (middle panels), and the density contrast  $\Delta \rho = 100 \times (\rho - \langle \rho \rangle_\theta) / \langle \rho \rangle_\theta$  (right panels), respectively.  $\langle \rangle_\theta$  denotes a horizontal average at a given radius.

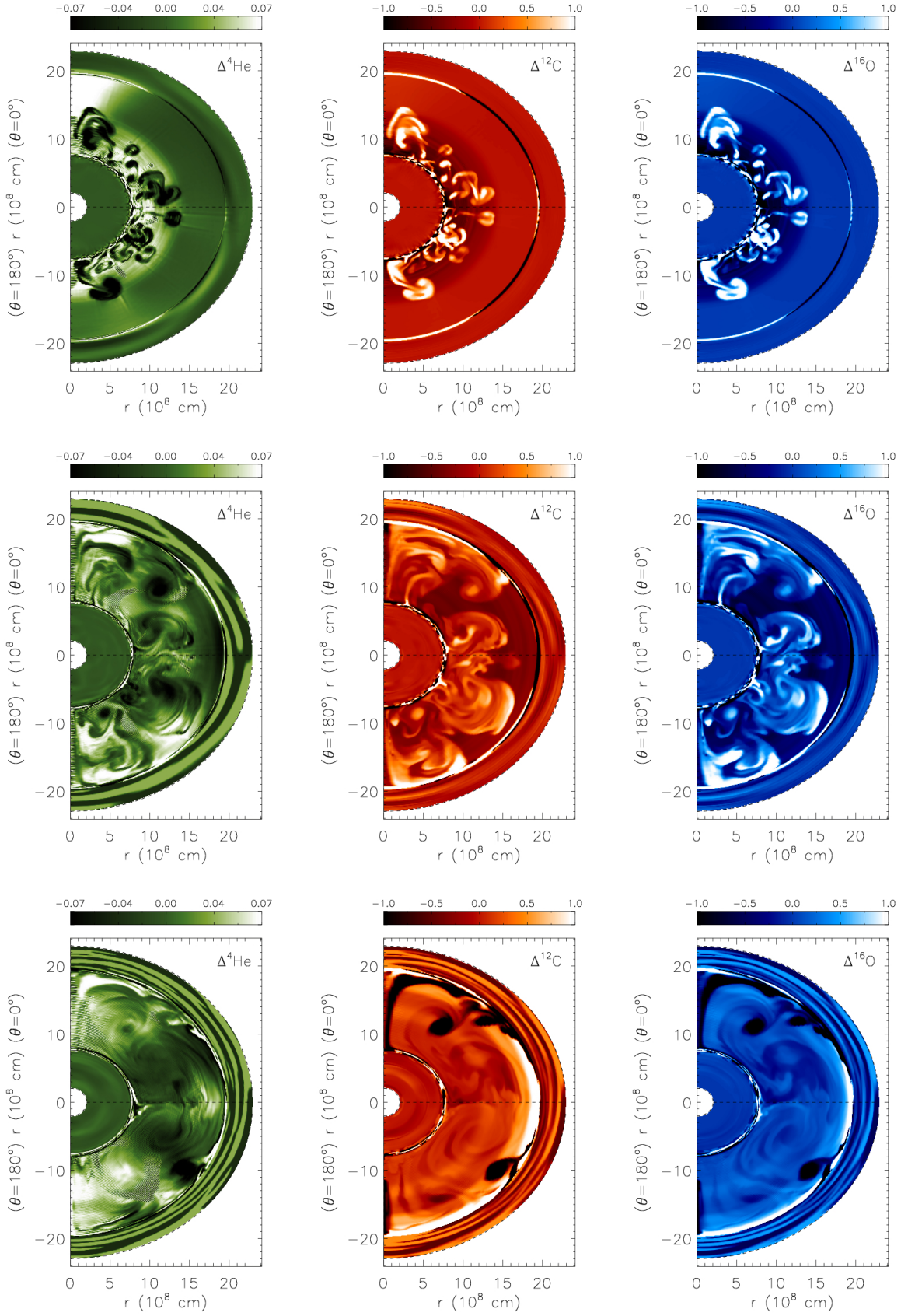


**Figure 7.14.:** Snapshots of the onset of convection at 1 200s (upper panels), and of the evolved convection (lower panels) in model hefl.2d.jw2 at 1 900s (middle panels) and 6 600s (bottom panels), showing the helium  ${}^4\text{He}$  contrast  $\Delta^4\text{He} = 100 \times ({}^4\text{He} - \langle {}^4\text{He} \rangle_\theta) / \langle {}^4\text{He} \rangle_\theta$  (left panels), the carbon  ${}^{12}\text{C}$  contrast  $\Delta^{12}\text{C} = 100 \times ({}^{12}\text{C} - \langle {}^{12}\text{C} \rangle_\theta) / \langle {}^{12}\text{C} \rangle_\theta$  (middle panels), and the oxygen  ${}^{16}\text{O}$  contrast  $\Delta^{16}\text{O} = 100 \times ({}^{16}\text{O} - \langle {}^{16}\text{O} \rangle_\theta) / \langle {}^{16}\text{O} \rangle_\theta$  (right panels), respectively.  $\langle \rangle_\theta$  denotes a horizontal average at a given radius.



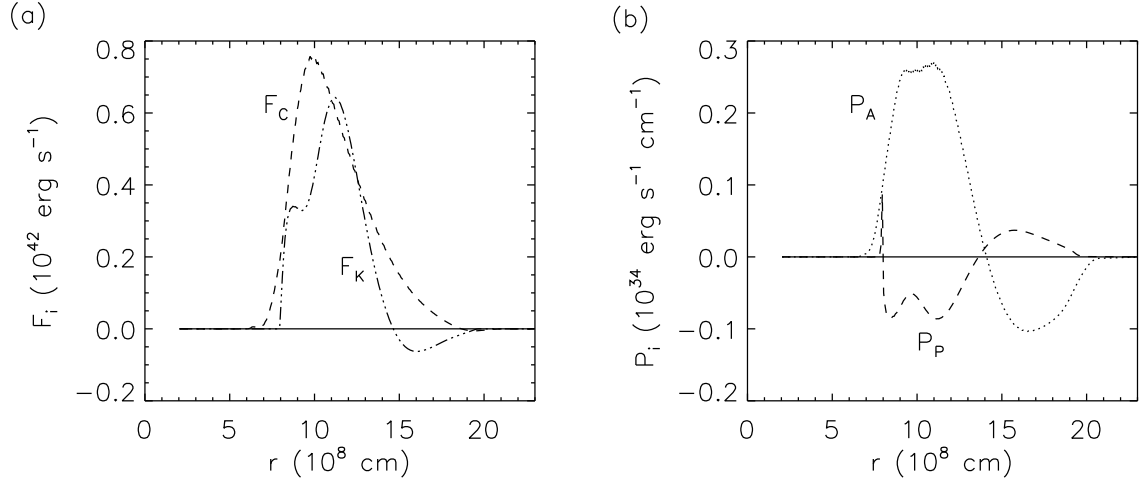


**Figure 7.15.:** Snapshots of various energy fluxes and source terms in model hefl.2d.jw2 (time averaged over 6000 s or almost 6 convective turnover times, from  $t = 3000$  s to  $t = 9000$  s): (a) convective flux  $F_C$  (dashed), and the kinetic flux (dash-dotted); (b) source terms due to work done by buoyancy forces  $P_A$  (dotted), and due to volume changes  $P_P$  (dash-dotted).

**Table 7.4.:** Some properties of the 2D simulations based on initial model JW: number of grid points in radial ( $N_r$ ) and angular ( $N_\theta$ ) direction, radial ( $\Delta r$  in  $10^6$  cm) and angular grid resolution ( $\Delta\theta$ ), characteristic length scale  $l_c$  of the flow (in  $10^8$  cm), characteristic r.m.s velocity  $v_c$  of the flow (in  $10^6$  cm s $^{-1}$ ) averaged over the width of the convection zone  $R \sim l_c$ , Reynolds number  $R_n$  associated with the numerical viscosity of our code (Porter & Woodward 1994), damping timescale due to the numerical viscosity  $t_n$ , typical convective turnover time  $t_o = 2R/v_c$ , and maximum evolution time  $t_{max}$  (in s), respectively.

run	$N_r \times N_\theta$	$\Delta r$	$\Delta\theta$	$l_c$	$v_c$	$R_n$	$t_n$	$t_o$	$t_{max}$
hefl.2d.jw1	180×90	7.77	2°	11.	1.57	4 600	40 700	1400	9 000
hefl.2d.jw2	270×180	5.19	1°	11.	2.02	19 900	137 240	1090	9 000

is not fully resolved yet. The resolution of this model is similar to the resolution of the model hefl.2d.1 where the temperature inversion is only smeared similarly.

The convective and kinetic energy fluxes are again exhibiting the typical shape with positive values across the convection zone, and with positive work done by buoyant forces in the inner part of the convection zone (Fig. 7.15).

### 7.6.3. Model SC

In Table 7.5, we summarize some characteristic parameters of our two-dimensional simulation which is based on model SC. The simulation covered roughly 7500 s. The grid covers a radial region from  $5 \times 10^8$  cm to  $6 \times 10^9$  cm, and contains a splitted convection zone due to the hydrogen entrainment. The inner part of the convection zone (powered by triple- $\alpha$  burning) spans from  $1.1 \times 10^9$  cm to  $3.53 \times 10^9$  cm about 3.7 pressure and 2.3 density scale heights, respectively. The outer part spans from  $3.53 \times 10^9$  cm up to  $5.4 \times 10^9$  cm *i.e.* over 2.9 pressure and 2.4 density scale heights. Note that, the inner part is still well off the inner grid boundary. The boundary conditions in radial direction are reflective, and in angular direction periodic.

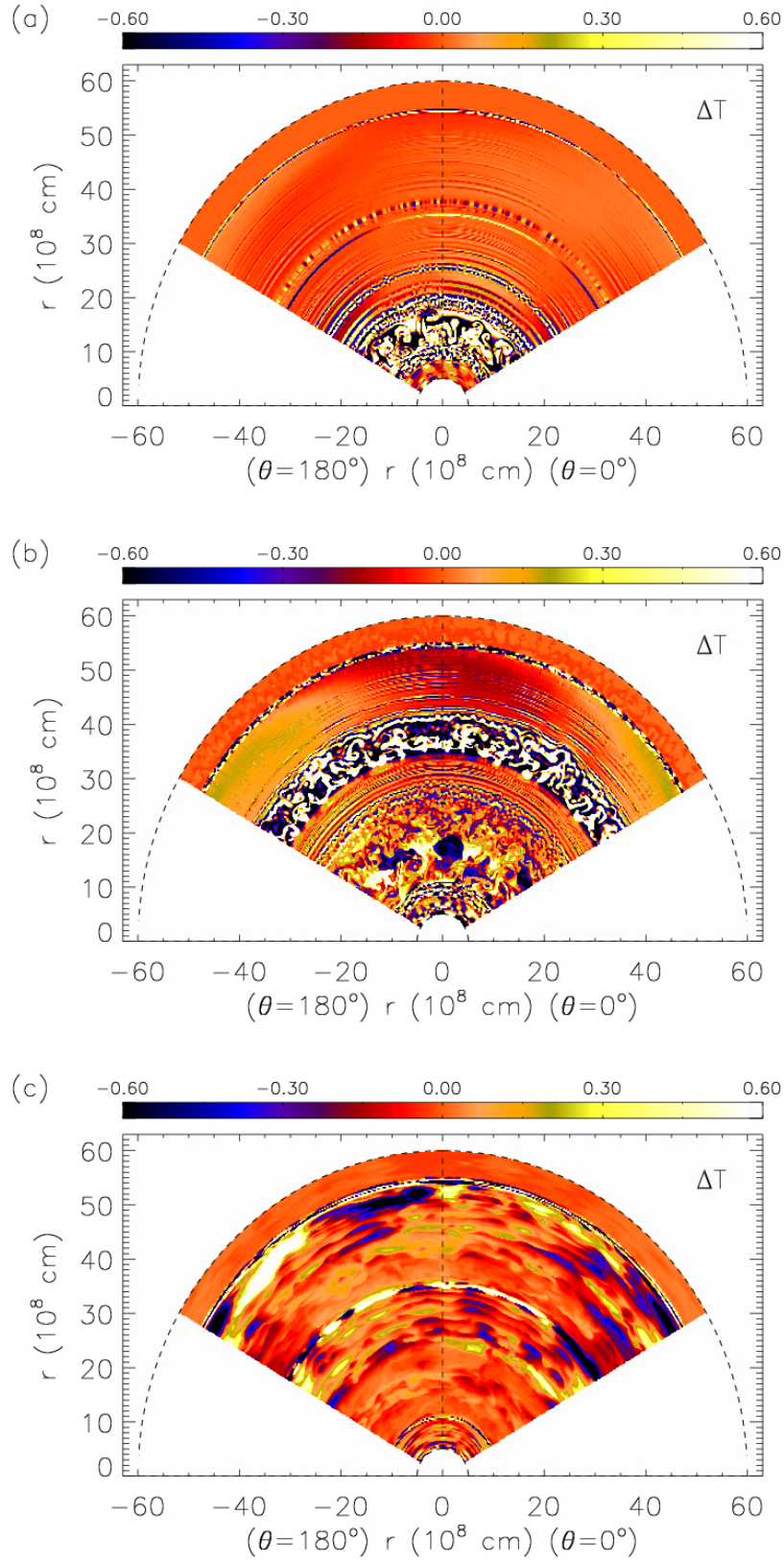


**Figure 7.16.:** Snapshots of the convection in simulation `hefl.2d.sc1` based on model SC, showing the temperature contrast  $\Delta T = 100 (T - \langle T \rangle_\theta) / \langle T \rangle_\theta$  at  $t_1 = 280$  s (a),  $t_2 = 530$  s (b) and  $t_3 = 5630$  s (c).  $\langle \rangle_\theta$  denotes a horizontal average at a given radius.

**Table 7.5.:** Some properties of the 2D simulation based on initial model SC: number of grid points in radial ( $N_r$ ) and angular ( $N_\theta$ ) direction, radial ( $\Delta r$  in  $10^6\text{cm}$ ) and angular grid resolution ( $\Delta\theta$ ), characteristic length scale  $l_c$  of the flow (in  $10^8\text{cm}$ ), characteristic r.m.s velocity  $v_c$  of the flow (in  $10^6\text{ cm s}^{-1}$ ) averaged over the width of the convection zone and maximum evolution time  $t_{max}$  (in s), respectively.

run	$N_r \times N_\theta$	$\Delta r$	$\Delta\theta$	$l_c$	$v_c$	$t_{max}$
hefl.2d.sc1	720×360	7.64	0.5°	44.	0.66	7 470

Despite the high energy production rate due to the CNO cycle in the upper part of the convection zone which is 13 times higher than the inner triple- $\alpha$  burning, the convective motion appears first within the inner part of the convection zone at around 200 s (Fig. 7.16). The onset of the convection in the outer part follows at around 500 s. After a while relaxes the model into a steady state where the radial and angular velocity component of the flow have almost the same r.m.s values which is an indication of internal gravity waves ([Asida & Arnett 2000](#)).

Due to the waves, the typical convective pattern with vortices practically does not exist anymore (Fig. 7.16: c) and therefore the convective mixing and transport of energy is likely completely different in compare what we know and assume in general (see Sect. 2.2). It might be that the volume between the two convection zones act as a resonant chamber which amplifies the waves until they become a dominant feature of the helium core during such a flash.



# 8

## Three-Dimensional Hydrodynamic Simulations

It is well known that two-dimensional hydrodynamic simulations of turbulence are seriously biased due to the imposed symmetry restrictions. Opposite to 3D flows, the turbulent kinetic energy increases from small to large scales in 2D simulations, i.e., the energy cascade to smaller length scales characteristic of turbulent flows is not reproduced (Canuto 2000; Bazan & Arnett 1998). Hence, the mean convective velocities, the amount of overshooting, and the size of turbulent structures is too large. Thus, as pointed out already by *e.g.* Muthsam et al. (1995) and Bazan & Arnett (1998), three-dimensional simulations are required to validate the predictions of two-dimensional simulations.

The hydrodynamic evolution of the core helium flash in three-dimensions will provide us informations on the structure and topology of turbulent convection and entrainment into convectively stable layers during the core helium flash without any symmetry restrictions and give us hints where the two-dimensional simulations fail. One of our goals in following sections is a comparison of two- and three-dimensional hydrodynamic simulations versus predictions made by the mixing length theory.

Our three-dimensional hydrodynamic models are based on the initial model M and are characterized by a convectively unstable layer (the convection zone) embedded in between two stable layers composed of several chemical nuclear species and of a partially degenerate electron gas. Similar systems were studied in the past by many authors *e.g.* Hurlburt et al. (1986, 1994); Muthsam et al. (1995); Singh et al. (1995, 1998) and Brummell et al. (2002) assuming, however, that the stellar matter is composed of a single ideal Boltzmann gas. This gives extra relevance to our simulations because they allow us to study, *e.g.*, the dependence of turbulent entrainment and the structure of convective boundary layers on the composition of the stellar gas, and on the composition gradients present in the stellar model.

In order to study the differences between two- and three-dimensional simulations, we performed one two-dimensional and one three-dimensional simulation which have the same radial and angular resolution. Their properties are summarized in Table 8.1. The simulations hefl.2d.a and hefl.3d cover 9500s and 6000s of evolutionary time near the peak of the core helium flash, respectively, and were computed on a computational grid spanning a wedge of  $120^\circ$  in angular directions centered at the equator. The rather wide angular grid appeared to be necessary for the three-dimensional simulations, due to the size of the largest vortices ( $\sim 40^\circ$ ) found in previous

**Table 8.1.:** Some properties of the two and three-dimensional simulation: number of grid points in  $r$  ( $N_r$ ),  $\theta$  ( $N_\theta$ ) and  $\phi$  ( $N_\phi$ ) direction, spatial resolution in  $r$  ( $\Delta r$  in  $10^6$  cm),  $\theta$  ( $\Delta\theta$ ), and  $\phi$  ( $\Delta\phi$ ) direction, characteristic velocity  $v_c$  (in  $10^6$  cm s $^{-1}$ ) of the flow during the first 6000 s, expansion velocity at temperature maximum  $v_{exp}$  (in m s $^{-1}$ ), typical convective turnover time  $t_o = 2R/v_c$  (in s) where  $R$  is the height of the convection zone, and maximum evolutionary time  $t_{max}$  (in s), respectively.

run	grid	$\Delta r$	$\Delta\theta$	$\Delta\phi$	$v_c$	$v_{exp}$	$t_o$	$t_{max}$
hefl.2d.a	$180 \times 90$	5.55	$1.5^\circ$	-	1.44	24.	650	9500
hefl.3d	$180 \times 90 \times 90$	5.55	$1.5^\circ$	$1.5^\circ$	0.85	10.	1105	6000

two-dimensional simulations (Sect. 7).

All models possess a convection zone that spans 1.5 density scale heights and that is enclosed by convectively stable layers extending out to a radius of  $1.2 \times 10^9$  cm. In the 3D model hefl.3d, we used reflective boundary conditions in every coordinate direction. For the model hefl.2d.a, it turned out to be necessary to impose periodic boundary conditions in angular direction, because reflective boundaries together with the  $120^\circ$  wedge size affect the large scale convective flow adversely, leading to higher convection velocities.

We are limited with our explicit hydrodynamics code by the CFL condition which is most restrictive near the center of the spherical grid. Therefore, we cut off the inner part of the grid at a radius of  $2 \times 10^8$  cm that is still sufficiently far away from the radius of the temperature inversion at  $r \sim 5 \times 10^8$  cm. To trigger convection, we imposed a random flow field with a maximum (absolute) velocity of  $10$  cm s $^{-1}$ , and a random density perturbation  $\Delta\rho/\rho \leq 10^{-2}$ . Imposing some explicit non-radial perturbations is necessary, because a spherically symmetric model evolved with Herakles on a grid in spherical coordinates will remain spherically symmetric forever. This is different from the study of [Asida & Arnett \(2000\)](#), who did not perturb the initial model by an artificial random flow, as instabilities were growing from round-off errors. The different perturbation techniques seem not to influence the final thermally relaxed steady state ([Meakin & Arnett 2007b](#)).

Because thermal transport of energy by conduction and radiation is roughly seven orders of magnitude smaller than the convective energy flux, it has been neglected in the simulations. Most of the liberated nuclear energy is carried away by convection. All computed models are non-rotating, because rotation seems not to play an important role during the core helium flash ([Lattanzio et al. 2006](#)).

## 8.1. Temporal Evolution

The two- and three-dimensional model hefl.2d.a and hefl.3d undergo initially ( $t < 1200$  s) a common evolution where convection sets in after roughly 1000 s. During this phase, hot bubbles appear in the region where helium burns in a thin shell ( $r \sim 5 \times 10^8$  K). After  $\sim 200$  s, they cover complete height of the convective region which is  $\sim 4.8 \times 10^8$  cm and reach a steady state with several upstreams (or plumes) of hot gas carrying the released nuclear energy away from the burning region, thereby inhibiting a thermonuclear runaway.

The models are characterized by a sandwich structure with top and bottom convectively stable layers enclosing an unstable one. The unstable convection zone is characterized by high values of the kinetic energy density (Fig. 8.1). The top and bottom strips are the convective stable layers being characterized by induced waves due to the convection. The strip of high kinetic energy

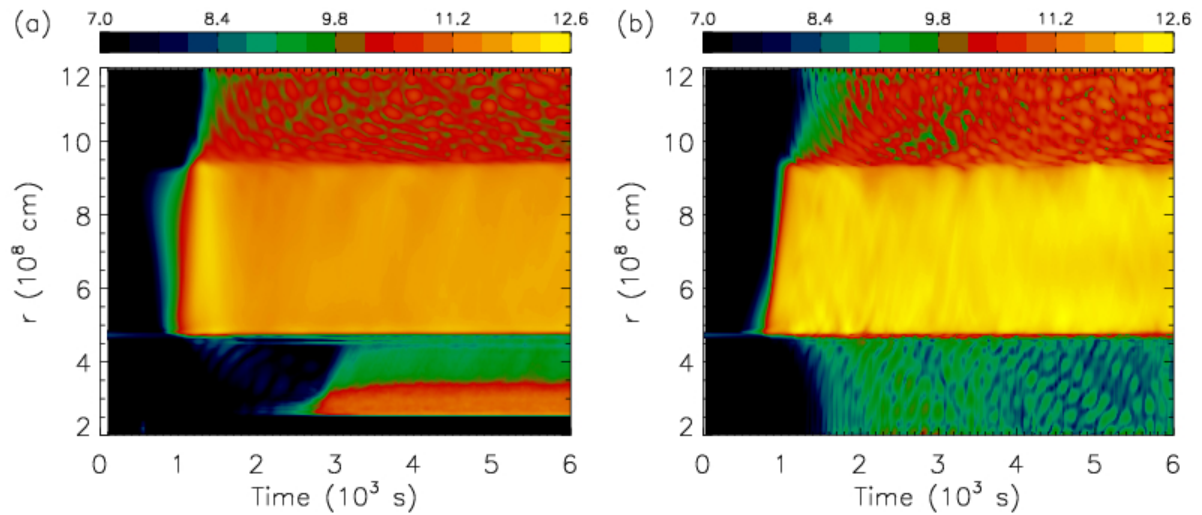


**Figure 8.1.:** Temporal evolution of a mean kinetic energy density (in erg/g) averaged over angular dimensions in hefl.3d (a) and hefl.2d.a (b), respectively.

density starting at time  $\sim 3000$  s at the bottom layer in hefl.3d is strongly biased by numerical instabilities caused by the proximity of the inner reflective grid boundaries.

The models reach a steady state after  $\sim 2000$  s (Figs. 8.1 and 8.2). The steep increase of the total kinetic energy from roughly  $10^{39}$  erg to  $10^{45}$  erg (Fig. 8.2) marks the onset of convection. The kinetic energy density shows small fluctuations in the fully evolved convection zone, and is by an order of magnitude larger in model hefl.2d.a than in model hefl.3d. This is in agreement with other studies, as it is well known that two-dimensional turbulence is more intensive (see, *e.g.* Muthsam et al. (1995)). The total energy production is about 10% higher in the 3D model due to its slightly higher temperature and the strong dependence of the triple- $\alpha$  reaction rate on temperature.

We observe buoyancy driven internal gravity waves (Zahn 1991; Hurlburt et al. 1986, 1994; Meakin & Arnett 2007b) in the convectively stable layers (Fig. 8.1, Fig. 8.7), but we do not discuss these waves any further here, because their properties are likely biased by the reflective boundaries (Asida & Arnett 2000). We only point out that the differences in amplitude and frequency seen in Fig. 8.1 are physical, *i.e.* internal gravity waves have a lower frequency and amplitude in 3D than in 2D.

## 8.2. Size and Structure of Convective Flow

Fully evolved convection ( $t > 2000$  s) in the 3D model hefl.3d differs significantly from that in the corresponding 2D model hefl.2d.a. The convective flow is dominated in the 2D model by vortices having (angular) diameters ranging from  $30^\circ$  to  $50^\circ$  (Fig. 8.3), and an aspect ratio of close to one. The vortices are qualitatively similar to those found in other two-dimensional simulations (Hurlburt et al. 1986, 1994; Porter & Woodward 1994; Bazan & Arnett 1998). This vortex structure of 2D turbulence is quite typical, and arises from the self-organization of the flow (Fornberg 1977; McWilliams 1984).

The convective flow in the 3D model hefl.3d consists of column-shaped plumes (Fig. 8.3, Fig. 8.7), and contrary to the 2D model hefl.2d.a, it does not show any dominant angular mode. The typical angular size of turbulent features ranges from  $10^\circ$  to  $30^\circ$  (Fig. 8.3). The power spectra of angular velocity fluctuations show that turbulent elements have an almost time-independent

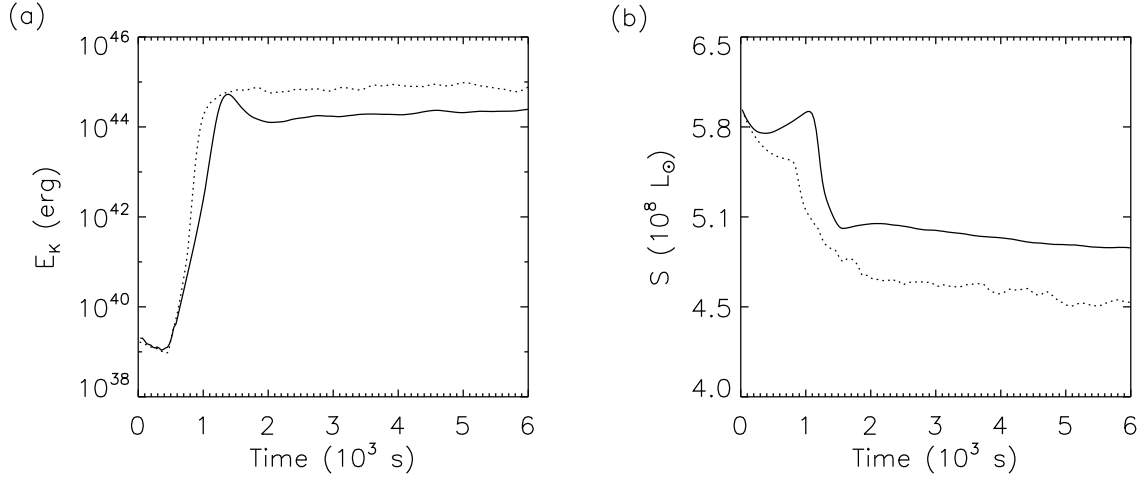


**Figure 8.2.:** Temporal evolution of the total kinetic energy  $E_K$  (a) and the total energy production rate (b) in the model hefl.3d (solid) and hefl.2d.a (dotted), respectively.

**Table 8.2.:** Root mean square fluctuation amplitudes of various variables within the convection zone ( $cnvz$ :  $5 \times 10^8 \text{ cm} \leq r \leq 9.2 \times 10^8 \text{ cm}$ ) averaged over a time period of about 2500 s: temperature  $T'/\langle T \rangle$ , density  $\rho'/\langle \rho \rangle$ , helium abundance  ${}^4\text{He}'/\langle {}^4\text{He} \rangle$ , and carbon abundance  ${}^{12}\text{C}'/\langle {}^{12}\text{C} \rangle$ .

pos	run	$T'/\langle T \rangle$	$\rho'/\langle \rho \rangle$	${}^4\text{He}'/\langle {}^4\text{He} \rangle$	${}^{12}\text{C}'/\langle {}^{12}\text{C} \rangle$
cnvz	hefl.3d	0.00058	0.00015	0.00009	0.01433
	hefl.2d.a	0.00074	0.00021	0.00007	0.01272

characteristic angular size of  $30^\circ$  -  $50^\circ$  in case of the 2D model, while the spectra computed for the 3D model change with time and exhibit no dominant angular mode.

We find turbulent flow features across the whole convection zone resulting from the interaction of convective up and downflows. Close to the edges of the convective zone we observe the smallest turbulent flow features that form when compact turbulent plumes are decelerated and break-up (Brummell et al. 2002). Shear instabilities likely play an important role in the development of the turbulent flow as well (Cattaneo et al. 1991).

Tables 8.2 and 8.3 provide time-averaged root mean square fluctuation amplitudes of various variables of the convective flow inside the convection zone and near its edges, respectively for models hefl.3d and hefl.2d.a. The temperature and density fluctuations are 30-40 % larger in the 2D model than in the 3D one. This is expected, because vortices are stable in 2D flows but decay in 3D ones (Fig. 8.3). The fluctuations in the composition ( ${}^4\text{He}$  and  ${}^{12}\text{C}$ ) are larger by 10-30% in the 3D model which is a result of more “broken” and hence more non-uniform mixing of chemical elements than in the 2D one.

The temperature and density fluctuation amplitudes are a factor of 2-3 larger near the inner edge than near the outer edge of the convective layer. At both edges are the fluctuation amplitudes by a factor of 2-4 larger in 2D than in 3D models. The fluctuations in the composition ( ${}^4\text{He}$  and  ${}^{12}\text{C}$ ) in both models differ close to the convective boundaries as well, by up to a factor of two.



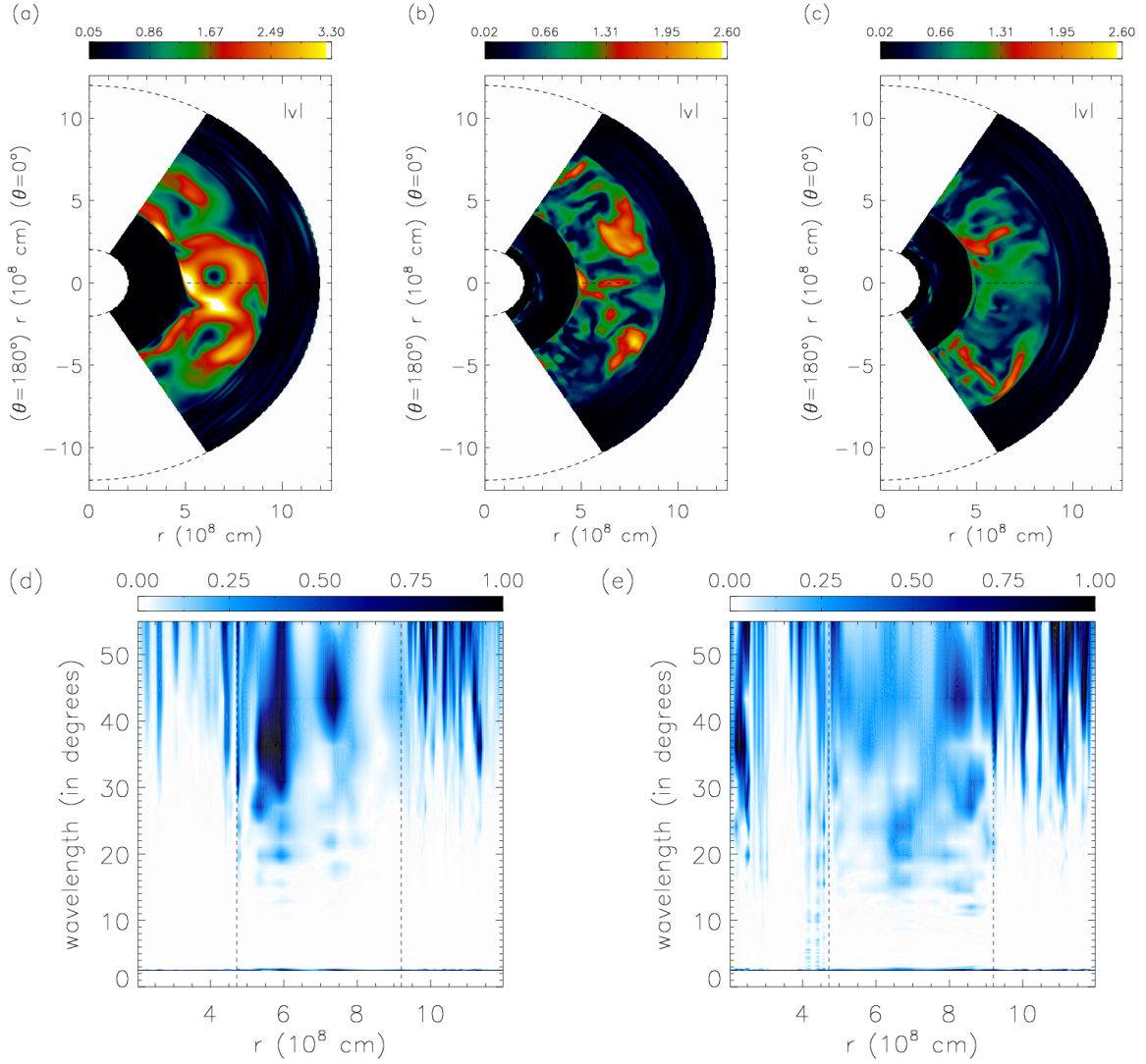


**Figure 8.3.:** *Upper panels:* Snapshots taken at  $\sim 4754$  s showing contour plots of the absolute value of the velocity (in units of  $10^6$  cm s $^{-1}$ ) for the 2D model hefl.2d.a (a), and for the 3D model hefl.3d in a meridional plane of azimuth angle  $\phi = 50^\circ$  (b) and  $\phi = 70^\circ$  (c), respectively. *Lower panels:* Normalized power spectra of angular fluctuations in the absolute velocity as a function of radius for the 2D model hefl.2d.a (a) averaged over time from 2100 s to 9500 s, and for the 3D model hefl.3d (b) averaged over time from 2250 s to 6000 s, and azimuthal angle. The dashed vertical lines mark the edges of the convective zone of the initial model according to the Schwarzschild criterion.

**Table 8.3.:** Root mean square fluctuation amplitudes of various variables at the *inner* ( $r = 5 \times 10^8$  cm) and *outer* ( $r = 9.2 \times 10^8$  cm) edge of the convection zone averaged over a time period of about 2500 s: temperature  $T'/\langle T \rangle$ , density  $\rho'/\langle \rho \rangle$ , helium abundance  ${}^4\text{He}'/\langle {}^4\text{He} \rangle$ , and carbon abundance  ${}^{12}\text{C}'/\langle {}^{12}\text{C} \rangle$ .

pos	run	$T'/\langle T \rangle$	$\rho'/\langle \rho \rangle$	${}^4\text{He}'/\langle {}^4\text{He} \rangle$	${}^{12}\text{C}'/\langle {}^{12}\text{C} \rangle$
inner	hefl.3d	0.00643	0.00144	0.00045	0.11497
	hefl.2d.a	0.02027	0.00441	0.00024	0.08958
outer	hefl.3d	0.00420	0.00117	0.00089	0.45105
	hefl.2d.a	0.00626	0.00177	0.00141	0.62193

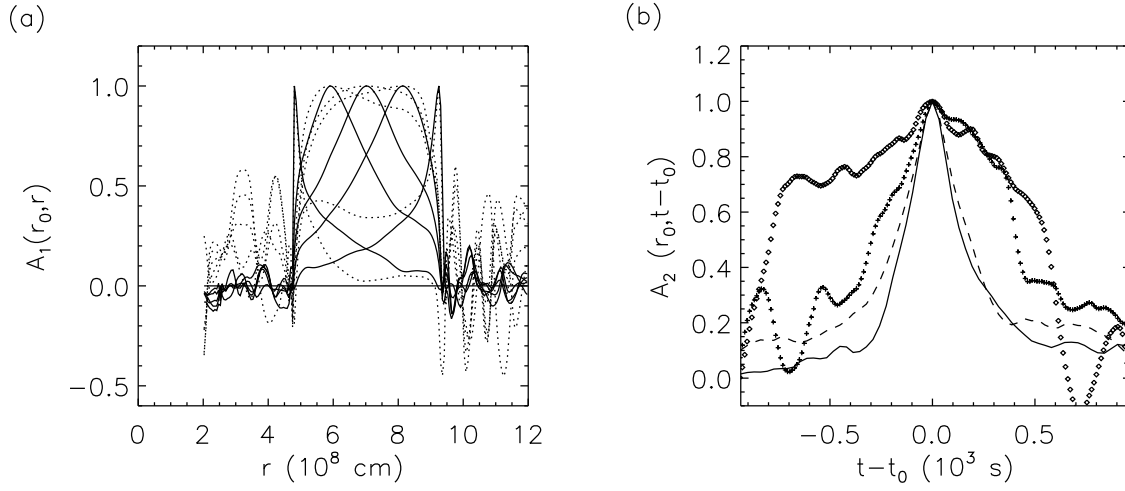


**Figure 8.4.:** (a) Auto-correlation function  $A_1(r_0; r)$  for different radii  $r_0$  ( $4.8 \times 10^8$  cm,  $5.9 \times 10^8$  cm,  $7 \times 10^8$  cm,  $8.1 \times 10^8$  cm,  $9.25 \times 10^8$  cm) in the model hefl.2d.a (dotted lines) and hefl.3d (solid lines) at  $t \sim 4000$  s. (b) Auto-correlation function  $A_2(r_0; t - t_0)$  for model hefl.3d at 2 different times  $t_0 \sim 2260$  s (solid) and  $2900$  s (dashed), respectively, and model hefl.2d.a at the same times  $t_0$  (crosses and diamonds, respectively);  $r_0$  is  $7.6 \times 10^8$  cm.

### 8.3. Stability of the Flow Structures

To analyze the size and the stability of the vortices we introduce an auto-correlation function of the radial velocity

$$A_1(r_0; r) = \frac{\langle v_r(r_0) v_r(r) \rangle_{\Omega, t}}{\langle v_r(r_0)^2 \rangle_{\Omega, t}^{1/2} \langle v_r(r)^2 \rangle_{\Omega, t}^{1/2}} \quad (8.1)$$

that measures the radial extent of flow patterns at a given radius  $r_0$ , or equivalently the radial size of vortices. The notation  $\langle \rangle_{\Omega, t}$  indicates averaging over angles and time. A second auto-correlation function

$$A_2(r_0; t - t_0) = \frac{\langle v_r(r_0, t_0) v_r(r_0, t) \rangle_{\Omega}}{\langle v_r(r_0, t_0)^2 \rangle_{\Omega}^{1/2} \langle v_r(r_0, t)^2 \rangle_{\Omega}^{1/2}} \quad (8.2)$$

provides a measure of the lifetime of flow patterns at radius  $r_0$ , beyond time  $t_0$ . Here, we average only over angles. Both correlation functions have the properties  $-1 \leq A_{1,2} \leq 1$ , and  $A_1(r_0; r_0) = 1$  and  $A_2(r_0; t_0 - t_0) = 1$ , respectively. They are similar to the autocorrelation function used by Chan et al. (1982); Chan & Sofia (1986).

Figure 8.4 displays the radial auto-correlation for models hefl.2d.a and hefl.3d and confirms the extension of the convective flow across the whole convective region as determined by the Schwarzschild criterion in the initial stellar model. The broad plateaus with  $A_1 \approx 1$  corresponding to the 2D model hefl.2d.a bear evidence of the axial symmetry imposed in the two-dimensional case which leads to pronounced circular vortices. In the three-dimensional case, the distributions of  $A_1$  tend to differ from unity at nearly all radii.

Figure 8.4 shows the temporal auto-correlations with two typical results for different  $t_0$ . The three-dimensional model always shows the typical behavior of a decrease of the function value to 0.5 within 200-250 s. From this we conclude that the flow pattern fluctuates always in the same way. This is different in the two-dimensional model, where  $A_2$  can keep high values for a much longer time implying rather persistent structure (the vortices) of the convective flow.

## 8.4. Turbulent Entrainment and Size of the Convection Zone

Convection may induce mixing in convectively stable layers adjacent to convectively unstable regions. Following Meakin & Arnett (2007b), we prefer to call this process turbulent entrainment, a term also used in oceanography, see *e.g.* Fernando (1991). The commonly used term (convective) overshooting accounts only for localized ascending or descending plumes crossing the edge of the convection zone. If the filling factor of these plumes or their crossing frequency is high, they can change the entropy in convectively stable regions surrounding convection zones, a process that is known as penetration (Brummell et al. 2002). Turbulent entrainment accounts for both overshooting and penetration.

Contrary to Hurlburt et al. (1994) we determine the depth of the entrainment neither by the radius where the kinetic energy carried into the stable layers is zero, nor by the radius where the kinetic energy has dropped to a certain fraction of its maximum value (Brummell et al. 2002). We find both conditions insufficient, because the kinetic energy flux becomes zero much faster than the convective flux, which is another possible indicator of the depth of the entrainment (see next subsection). Instead, we rather use the  $^{12}\text{C}$  mass fraction, as it is low outside the convection zone during the flash ( $X(^{12}\text{C}) < 2 \times 10^{-3}$ ), and as it can rise there only due to turbulent entrainment.

In this study, we use the condition  $X(^{12}\text{C}) = 2 \times 10^{-3}$  to define the edges of the convection zone. Due to the turbulent entrainment, these edges are pushed towards the stellar center and surface (Fig. 8.6). Hence, the width of the convection zone increases on the dynamic timescale, which is in contradiction with the predictions of one-dimensional hydrostatic stellar modeling, where the width of the convection zone is determined by the local Schwarzschild or Ledoux criterion. However, the criterion for the width of the convection zone cannot be a local one due to turbulent entrainment caused by convection.

The speed, at which the radius of the outer edge of the convection zone increases with time due to entrainment, is estimated for models hefl.2d.a and hefl.3d to be at most  $14 \text{ m s}^{-1}$ . The radius of the inner edge of the convection zone changes at a much smaller rate (Bazan & Arnett 1998; Meakin & Arnett 2007b), as the region interior to the convection zone is more stable against convection and has a higher density than the region exterior to the convection zone (Singh et al. 1995). The entrainment at the bottom of the convection zone also leads to a heating of the cool interior layers (Deupree & Cole 1983; Cole et al. 1985). This seems to be a robust feature of convection zones driven by nuclear burning, and is observed in other studies too (*e.g.* Asida & Arnett (2000)).

The region just interior to the convection zone shows less entrainment (Bazan & Arnett 1998; Meakin & Arnett 2007b), as the square of the Brunt-Väisälä frequency is almost ten times larger there than that in the region just outside the outer edge of the convection zone. The Brunt-Väisälä frequency is a good stability indicator since it is related to the behavior of convective elements within a convection zone, a fact also pointed out by Hurlburt et al. (1994). The Brunt-Väisälä frequency can be written as (Meakin & Arnett 2007b):

$$N^2 = -g \left( \frac{\partial \ln \rho}{\partial r} - \frac{\partial \ln \rho}{\partial r} \Big|_s \right), \quad (8.3)$$

where  $g$ ,  $\rho$ , and  $r$  are the gravitational acceleration, the density and the radius, respectively. A layer is convectively stable, if  $N^2 > 0$ , and unstable otherwise <sup>1</sup> (Kippenhahn & Weigert (1990)).

<sup>1</sup>The Brunt-Väisälä frequency is related to the bulk Richardson number known from oceanography, which is a more direct measure of the stability of the edges of a convection zone in the presence of a turbulent flow (Meakin & Arnett 2007b).

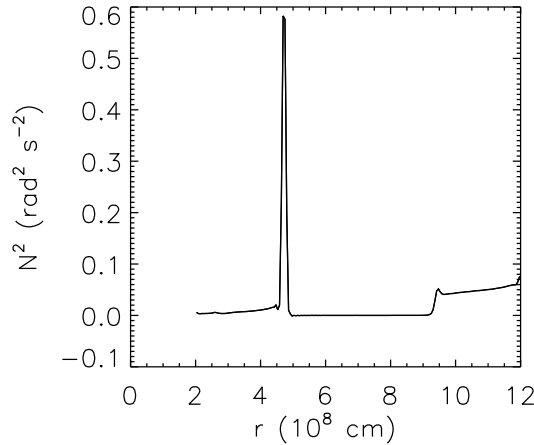


**Figure 8.5.:** Square of the Brunt-Väisälä buoyancy frequency as a function of radius for the 3D model hefl.3d at  $t = 4638$  s.

The Brunt-Väisälä frequency differs in the 2D and 3D simulations slightly, and has on average a very small negative value inside the convection zone:  $N^2 = -4.4 \times 10^{-6} \text{ rad}^2 \text{ cm}^{-2}$  in the 2D model hefl.2d.a, and  $N^2 = -1.2 \times 10^{-6} \text{ rad}^2 \text{ cm}^{-2}$  in the 3D model hefl.3d. Just outside (inside) the inner (outer) edge of the convection zone of the 2D model hefl.2d.a we find  $N^2 = 0.580 \text{ rad}^2 \text{ cm}^{-2}$  ( $0.053 \text{ rad}^2 \text{ cm}^{-2}$ ), and  $N^2 = 0.583 \text{ rad}^2 \text{ cm}^{-2}$  ( $0.052 \text{ rad}^2 \text{ cm}^{-2}$ ) for the 3D model hefl.3d, respectively (Fig. 8.5). In the 2D model hefl.2d.3, these frequencies are higher by about a factor of two.

Due to its high stability, the radius of the bottom edge of the convection zone did not change during the time covered by our simulations, except for an initial jump over one radial grid zone from  $r = 4.69 \times 10^8 \text{ cm}$  to  $r = 4.63 \times 10^8 \text{ cm}$ , when it was touched by convective downflows for the first time. However, entrainment may move the edge further towards the stellar center later in the evolution (see Sect. 7.4). The entrainment rate (*i.e.* the velocity at which the convective boundary moves) is lower by a factor of  $\sim 5$ -6 at the bottom of the convection zone in our 2D simulations of the core helium flash as compared to that at the outer boundary ( $\sim 14 \text{ m s}^{-1}$ ; see above). This behavior was also observed in 3D simulations of oxygen burning shell (Meakin & Arnett 2007b). This implies that the entrainment rate at the inner edge of the convection zone is  $\sim 2.5 \text{ m s}^{-1}$  in our core helium flash simulations. The corresponding change in radius is only  $1.5 \times 10^6 \text{ cm}$  or about a quarter of the width of a radial zone during the time covered by the simulations, and hence too small to be seen. As these estimates are resolution dependent, the values presented should be considered as order of magnitude estimates, only.

The entrainment is more efficient in the 2D model hefl.2d.a than in the 3D model hefl.3d. In 2D, the observed convective flow structures are large and fast rotating vortices that due to the imposed axisymmetry are actually tori (Bazan & Arnett 1998). They have a high filling factor near the edge of the convection zone where they overshoot or penetrate (Brummell et al. 2002). 3D structures crossing the edge of the convection zones are smaller (localized) plumes with a lower filling factor and smaller velocities.

We studied convective stability in detail only for the layer above the convection zone, where the gas is only weakly degenerate, and we are thus able to compare our results with those of similar systems simulated in 3D at high Reynolds numbers ( $\sim 10^4$ ) by Brummell et al. (2002). According to these authors, a stable layer allows for more “overshooting”, if its entropy gradient is smaller. We found that the turbulent entrainment lowers the entropy gradient at the outer

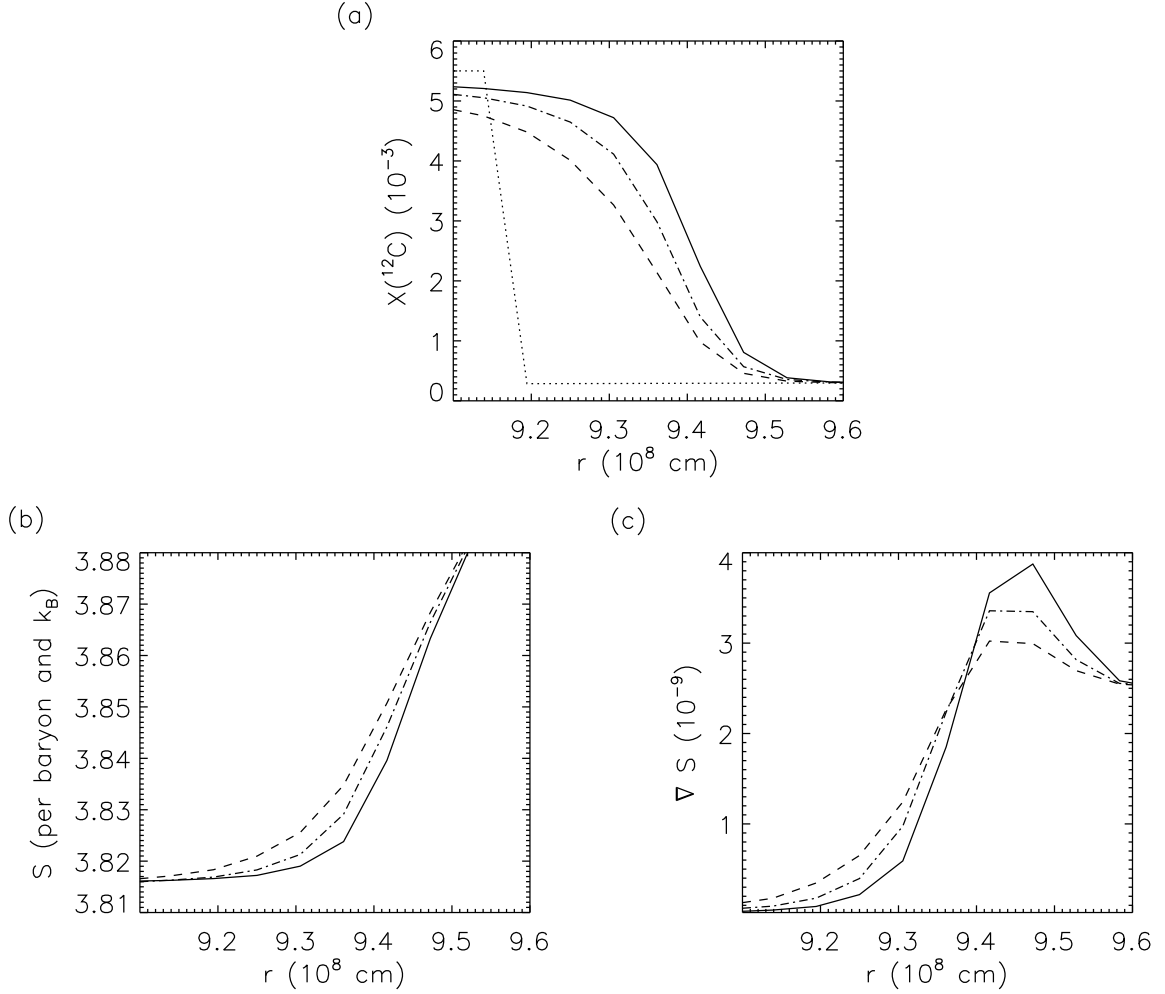


**Figure 8.6.:** Carbon mass fraction  $X(^{12}\text{C})$  (a), entropy  $S$  (b), and entropy gradient  $\nabla S$  (c) as a function of radius near the outer edge of the convection zone of model hefl.3d at three different epochs:  $t_1 = 2000$  s (dashed),  $t_1 = 4000$  s (dash-dotted), and  $t_1 = 6000$  (solid). In addition, the initial  $X(^{12}\text{C})$  profile is shown in the top panel (dotted).

edge of the convection zone in our simulations (Fig. 8.6). Hence, the stability of the exterior stable layer decreases with time, allowing for more turbulent entrainment.

Contrary to Brummell et al. (2002), who studied only single fluid flow, our simulations involve a mixture of different fluids of different composition. This complicates the above argumentation, as in a multi-fluid flow a shallow entropy gradient does not necessarily imply that the layer is less stable against turbulent entrainment. We plan to address this issue in more detail elsewhere. We have not analyzed the stability of the region below the inner edge of the convection zone, because it is highly degenerate and appears to be very stable. No significant entrainment of  $^{12}\text{C}$  was observed there during the entire simulation of models hefl.2d.a and hefl.3d, respectively. Simulations covering longer periods of time are therefore needed (see Sect. 7.4). The analysis of the energy fluxes inside the convection zone and near the outer edge of the convection zone, which will be discussed in the next subsection, will provide more information about the phenomenon of the turbulent entrainment.

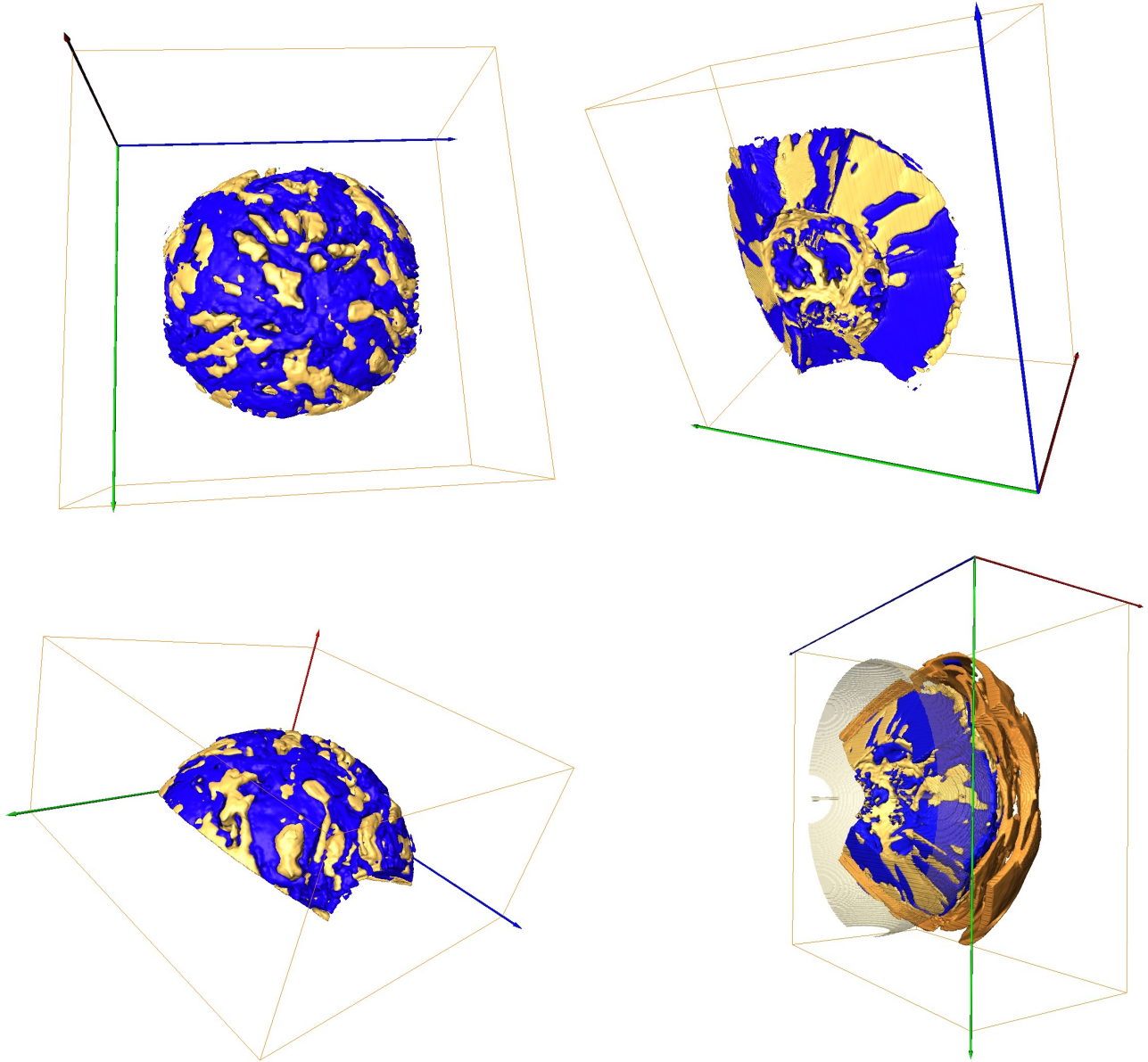


**Figure 8.7.:** Different views of isosurfaces of the velocity field for the 3D model hefl.3d at  $t = 3000$  s. The blue isosurface corresponds to radial downflows with  $v_r = -6 \times 10^5 \text{ cm s}^{-1}$ , and the yellow and brown isosurfaces show radial upflows with  $v_r = 6 \times 10^5 \text{ cm s}^{-1}$ , and  $1 \times 10^4 \text{ cm s}^{-1}$  (internal gravity waves), respectively. The edge sizes of the box are  $1.2 \times 10^9 \text{ cm}$  and  $2.4 \times 10^9 \text{ cm}$ , respectively. The yellow-greenish sphere in the bottom right panel marks the top of the convection zone according to the Schwarzschild criterion.



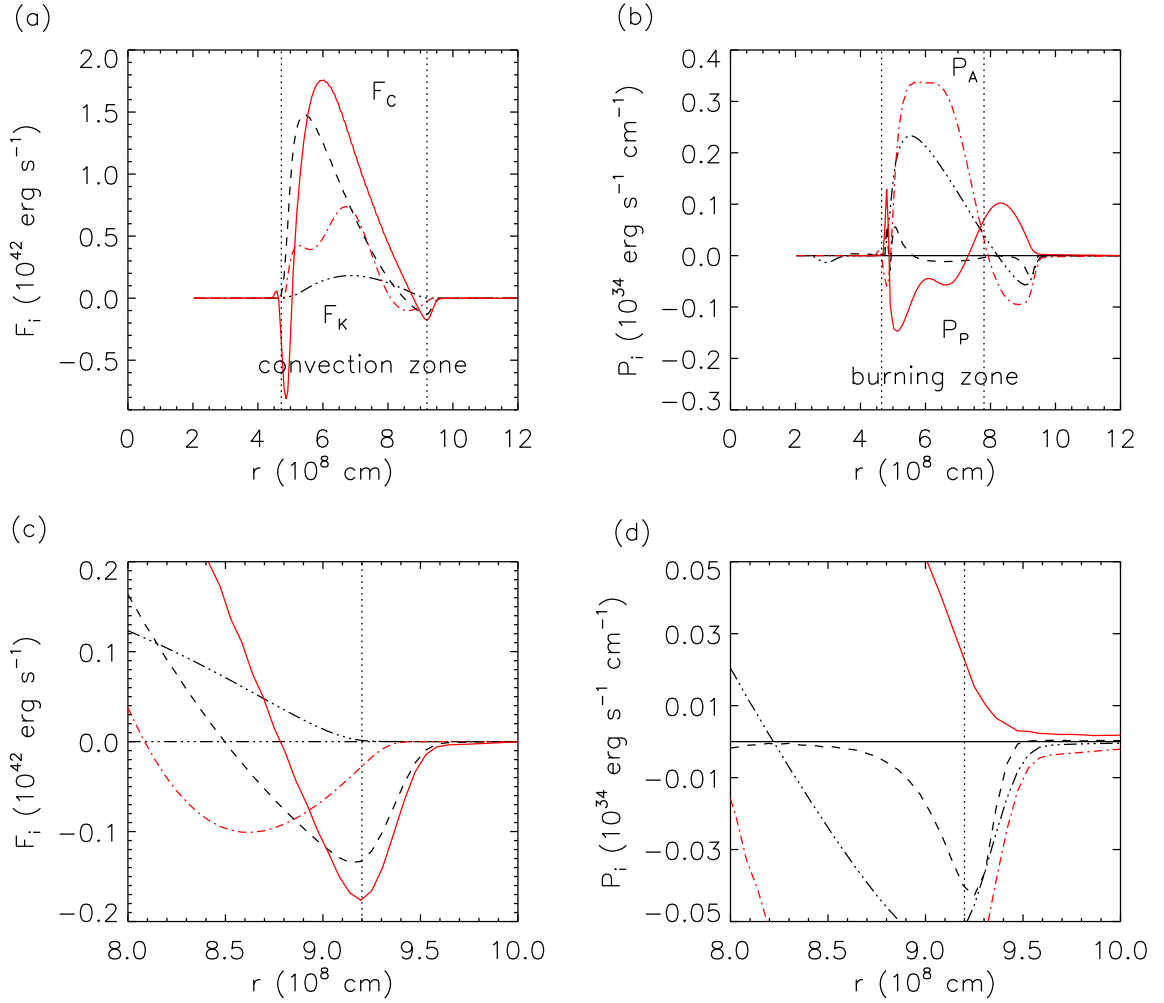


**Figure 8.8.:** Various energy fluxes and source terms as a function of radius averaged (from 2000 s to 6000 s) over about four convective turnover times. *Panel (a)* shows the convective flux  $F_C$  of the 2D model hefl.2d.a (solid-red) and the 3D model hefl.3d (dashed-black) together with the kinetic energy flux  $F_K$  in the 2D (dash-dotted-red) and 3D (dash-dot-dotted-black) model, respectively. The dotted vertical lines mark the edges of the convection zone in the initial model according to the Schwarzschild criterion. *Panel (b)* gives the source terms due to the work done by buoyancy forces  $P_A$  (dash-dot-dotted black) and due to volume changes  $P_P$  (dashed black) in the 3D model hefl.3d, and in the 2D model hefl.2d.a (dash-dotted-red, solid red) respectively. The vertical lines enclose the nuclear burning zone ( $T > 10^8$  K). *Panels (c)* and *(d)* show an enlarged view of the energy fluxes and source terms displayed in panels (a) and (b) near the outer edge of the convection zone.

## 8.5. Energy Fluxes

Energy fluxes are a useful tool for understanding convective flows (Chan & Sofia 1986; Hurlburt et al. 1986; Muthsam et al. 1995; Hurlburt et al. 1994; Brummell et al. 2002; Meakin & Arnett 2007b). They allow one to discriminate the energy transport due to different processes and mechanisms (*e.g.* due to convection, heat conduction, etc). We thus analyzed various energy fluxes and source terms that are defined in Appendix A.2. All energy fluxes and source terms (see, Fig. 8.8) are averaged over several convective turnover times, as they change considerably with time due to the appearance of plumes (Muthsam et al. 1995).

The convective energy flux is mainly positive as heat is mostly transported upwards by convec-

tion. It is larger in the 2D model hefl.2d.a, as in 2D the convective flow structures are more laminar and ordered, and thus experience less dissipation. The smaller value of  $F_C$  in the 3D model hefl.3d is a result of a less ordered flow throughout the whole convection zone. This is in agreement with Table 8.2 which shows that the fluctuations in temperature and density are smaller in the 3D model.

A kinetic energy flux arises from deviations from the mean convective flow (*i.e.* mainly from the upflow-downflow asymmetry). Typically it is largest in the most turbulent regions of the flow, where on top of the kinetic flux due to the up- and down-flow asymmetry, there is also a significant contribution due to the asymmetry of localized turbulent (convective) elements. Directly connected to this is the offset between the maxima of the kinetic and the convective flux (see Fig. 8.8), which reflects the fact that the convective flow decays more efficiently when the flow becomes strongly turbulent.

The work done by buoyancy forces is positive in the whole region of dominant nuclear burning (see Fig. 8.8) indicating either less dense and hot gas moving upwards or more dense and cooler gas moving downwards. A negative value of the work done by buoyancy forces implies the opposite situation, *i.e.* less dense and hot gas flowing downward or denser and cooler gas flowing upward. The latter is known as buoyancy breaking leading to a deceleration of the flow motion (Brummell et al. 2002), and to the unusual situation that hot matter tends to sink, and cool matter is likely to rise.

The gas should expand while rising up through the convection zone, *i.e.* the work done by buoyancy ( $P_A$ ) and by volume changes ( $P_P$ ) should always be anti-correlated. The anti-correlation is clearly seen only in the 2D model hefl.2d.a, whereas in the 3D model hefl.3d the quantities are on average anti-correlated only in the central region of the convection zone. At the inner edge of the convection zone, buoyancy drives gas upwards which is on average simultaneously compressed, probably by the broad downflows. At the outer edge where buoyancy braking occurs, the gas on average expands. Hence, it must expand faster than the upflows cool and are being compressed (a situation observed for the 2D model hefl.2d.a).

All the fluxes discussed here agree qualitatively well with those of our previous high-resolution 2D simulations (see Sect. 7.2). They are also qualitatively very similar to those of the high-resolution 3D simulations of Brummell et al. (2002) who investigated a stratified model with a convectively stable region located on top of a convectively unstable region both consisting of an ideal gas with a very high Reynolds number ( $\sim 10^4$ ). The angular and time averaged radial distributions of the kinetic and convective fluxes seem to be robust in the convectively unstable region, as our 3D results are qualitatively similar to those obtained in several other 3D studies (Hurlburt et al. 1994; Brummell et al. 2002; Meakin & Arnett 2007b).

The outer part of the convection zone, where buoyancy breaking occurs, resembles the overshooting region due to active penetration of plumes described by Hurlburt et al. (1986, 1994) and Brummell et al. (2002). Note, however, that this region is convectively stable at the beginning of their simulations, *i.e.* buoyancy breaking takes already place inside the convection zone in our models.

The distribution of the kinetic flux (Fig. 8.8) exhibits structural differences in the convection zone between 2D and 3D flows. The typical evolved 2D flow contains well defined vortices (Fig. 8.3) whose central parts never interact with the region of dominant nuclear burning. This results in a reduced kinetic energy flux at  $r \sim 5.5 \times 10^8$  cm, as this region corresponds to the central region of the vortices, which do not experience any strong radial motion. On the other hand, the distribution of the kinetic energy flux in the 3D model hefl.3d is rather smooth as a result of the column-shaped flow structures (Fig. 8.7).



The convective flux changes sign in stable layers since the downflows or upflows penetrating into the stable zones are suddenly too hot or cold compared to the surrounding gas. The penetration continues until the momentum of the convective elements is used up or diffusion smooths out the perturbations, and the convective flux approaches zero (Brummell et al. 2002). This fingerprint of turbulent entrainment is clearly present at both convective boundaries of our models (Fig. 8.8, Fig. 7.4).

The convective energy flux is relatively strong even in regions where the kinetic energy flux is almost zero. Therefore, the “zero” kinetic flux criterion (Hurlburt et al. 1994; Brummell et al. 2002) seems to be a bad indicator of entrainment which may extend well beyond the location where the kinetic flux becomes small. In fact, what is happening at the convective boundaries is an exchange between the potential energy of the stratification given by the buoyancy jump  $db = N^2 dr$  and the kinetic energy of the turbulence. Turbulence loses its kinetic energy by doing work against gravity, which leads to a reduction of the buoyancy jump, and hence to stability weakening of the stable boundary layer to the effects of the turbulent entrainment. The buoyancy jump  $db$  is a direct measure of the stability of the boundary layer. To mix gas into the boundary layer the buoyancy must be reduced. This is accomplished through the buoyancy flux  $q = P_A/\rho$ , which is related to the temporal variation of the buoyancy jump by  $db/dt = -\text{div}(q)$ , where  $P_A$  and  $\rho$  are the sink/source term of the kinetic energy due to buoyancy forces and the density, respectively.

The convective flux can directly be related to the buoyancy flux that is a function of  $P_A$  by a linear relation  $F_C = F_C(q)$  described in more detail by Meakin & Arnett (2007b). Figure 8.8 shows that this agrees well with what we observe in our simulations. It also supports our previous conclusion that entrainment is well indicated by the convective flux and the related buoyancy flux which via the equation  $db/dt = -\text{div}(q)$  leads to the decrease of the buoyancy jump in the stable layer. This in turn reduces the convective stability of that layer.

The properties of the entrainment at the outer convective boundary differs in models hefl.2d.a and hefl.3d (see Fig. 8.8). In the 2D model entrainment is reaching deeper into the stable layer due to a more active convection zone with higher typical velocities (Fig. 8.9) than in the 3D model. The radial distribution of the work done by buoyancy  $P_A$  is qualitatively similar in both the 2D and 3D models, *i.e.* it is negative indicating buoyancy breaking. Nevertheless, the work done by gas compression or expansion  $P_P$  is different. In the 2D model hefl.2d.a the gas on average is compressed ( $P_P$  is positive), while in the 3D model hefl.3d the gas is expanding at the boundary. This again confirms that 2D and 3D convective flows are qualitatively different.

## 8.6. The flow within the convection zone

The amount of energy ( $F_C + F_K$ ) which has to be transported by convection in order to prevent a thermonuclear runaway during the flash is similar in models hefl.2d.a and hefl.3d. Since the convective flux is almost the same in both models, the resulting typical convective velocities are higher in the 2D model than in the 3D one (Fig. 8.9).

The velocities in the 3D model hefl.3d match those predicted by mixing-length theory better than in the 2D model hefl.2d.a, where they are about a factor of 2 larger. This behavior was also observed in other hydrodynamic simulations of convective flows; see *e.g.* Muthsam et al. (1995); Meakin & Arnett (2007b). The radial velocities in the regions above and below the convection zone are smaller than the angular velocities in both models, which is a typical feature of internal gravity waves (Asida & Arnett 2000).

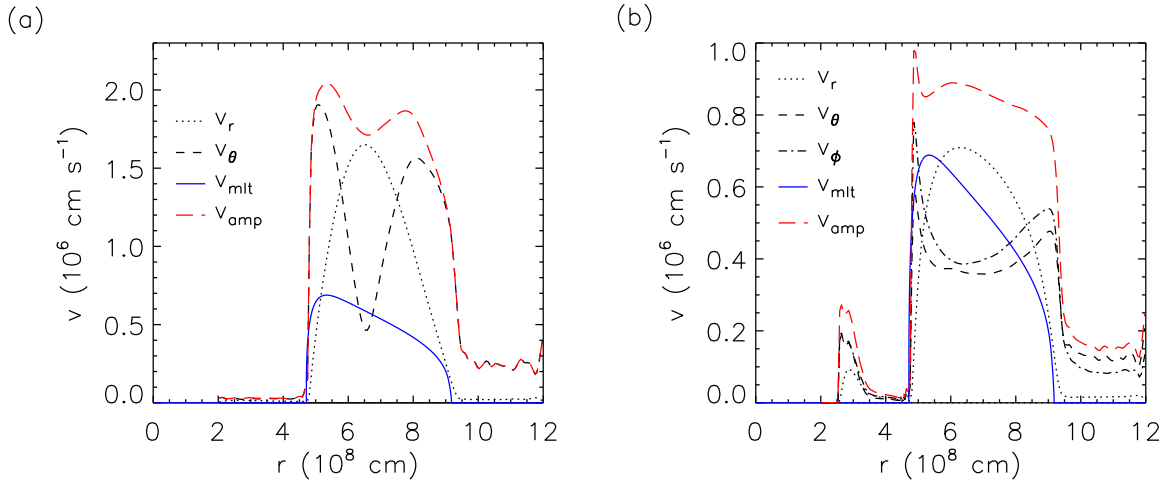


**Figure 8.9.:** Radial distributions of the time (from 2000 s to 4000 s) and angle-averaged velocity components ( $v_r$ ,  $v_\theta$ ,  $v_\phi$ ) and velocity modulus ( $v_{abs}$ ) for the 2D model hefl.2d.a (a), and the 3D model hefl.3d (b), respectively. The panels also show the velocity predicted by the mixing-length theory ( $v_{mlt}$ ).

In the 3D model hefl.3d, the flow in the convectively stable layer beneath the convection zone exhibits some numerical artefacts due to the proximity of the inner grid boundary (see Fig. 8.9). The radial distributions of the time and angle-averaged components of the velocity field and of the density and temperature fluctuations show pronounced maxima at  $\sim 3 \times 10^8 \text{ cm}$  and a sharp cut-off at  $r = 2.5 \times 10^8 \text{ cm}$  (Fig. 8.9, Fig. 8.10). The sharp cut-off is caused by the artificial damping we had to apply to the velocity field in the innermost grid zones to prevent numerical instabilities from spreading limitless to the convection zone.

Although, the flow velocities in the 3D model match those predicted by mixing-length theory very well, one should keep in mind that with increasing resolution the flow velocities will likely increase due to the reduced numerical viscosity. This trend is confirmed by the velocities obtained for the high-resolution 2D model hefl.2d.3 (Sect. 7) that are a factor of two higher than in the low-resolution model hefl.2d.a.

Near both edges of the convective zone there are large narrow peaks visible in the radial distributions of the time and angle-averaged density and temperature fluctuations (Fig. 8.10). These peaks are not caused by compression or expansion, but they are a result of the density and temperature discontinuities at the edges of the convection zone (Meakin & Arnett 2007a; Arnett et al. 2007), because any angle-dependent radial perturbation will cause large angular variations of density and temperature at these discontinuities.

The temperature fluctuations within the convection zone (Fig. 8.11) are rather uniformly distributed, but they are more intense near the outer edge of the convection zone, where they are only weakly correlated with the radial velocity. At the top of the convection zone the emerging rising plumes are embedded in an environment which sinks down (Fig. 8.11, bottom panels). This situation is similar to the sinking down-drafts with upwelling centers found in simulations by Nordlund & Dravins (1990) and Cattaneo et al. (1991).

## 8.7. Upflow-downflow asymmetry

The 2D and 3D simulations share the common property of an upflow-downflow asymmetry (Hurlburt et al. 1994; Muthsam et al. 1995; Brummell et al. 2002). The downflows cover a

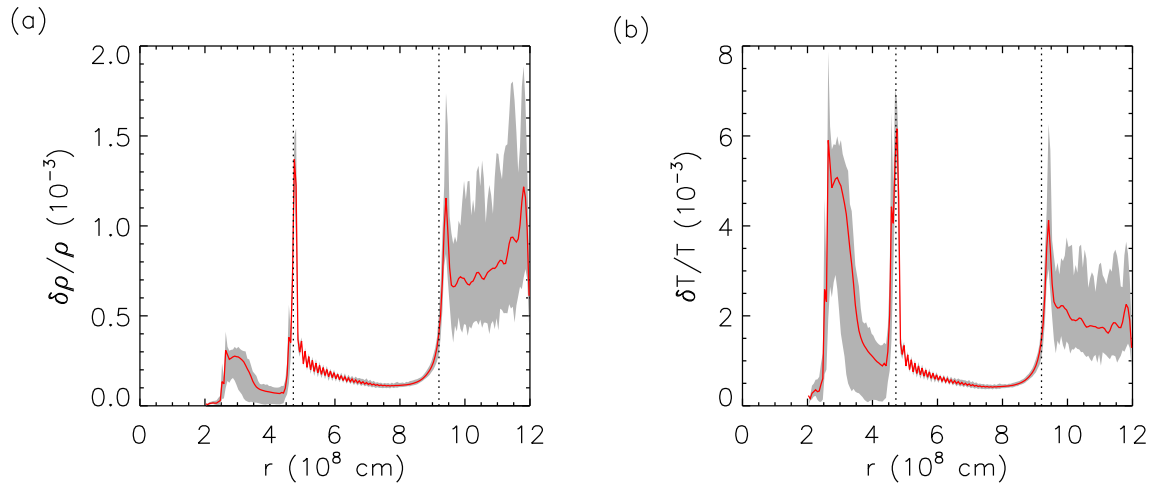


**Figure 8.10.:** Radial distributions of the time (from 2800 s to 4800 s) and angle-averaged density (a) and temperature (b) fluctuations in the 3D model hefl.3d (solid red line). The panels also show the angular variation of the respective quantity at a given radius (gray shaded region). The dotted vertical lines mark the edges of the convection zone as determined by the Schwarzschild criterion.

much larger volume fraction of the convection zone than the upflows. The filling factor of the downflows increases with decreasing depth (Rast et al. 1993; Meakin & Arnett 2007b) across most of the convection zone, and the downflows are more dominant in the 3D model hefl.3d than in the 2D models. Contrary to the simulations of oxygen shell burning of Asida & Arnett (2000) we find that the absolute velocities are about 40% higher in the upflows than in the downflows. Hence, the downflows in the convection zone of a star at the peak of the core helium flash are slower and broader than the faster and narrower upflows.

## 8.8. Mixing Within The Convection Zone

Cuts through the 3D model hefl.3d at  $t = 4815$  s showing the angular variation of temperature,  $^{12}\text{C}$  mass fraction, and radial velocity at three different radii (Fig. 8.11) demonstrate that the helium core at the peak of the core helium flash is a very turbulent environment at all heights of the convection zone.

The bottom of the convection zone contains hot filaments of gas where the temperature exceeds that of the environment by about 1%. The filaments contain ashes from helium burning, *i.e.*  $^{12}\text{C}$  and  $^{16}\text{O}$ , and they move across the whole bottom of the convection zone in a random way. The filaments are correlated with upflows, as the hot gas of burned matter is forced by buoyancy to rise towards the top of the convection zone.

The apparent turbulent nature of the convective flow indicated by our simulations implies that the treatment of mixing in stars as a diffusive process may lead to inaccurate or even incorrect results. Convective flows are rather advective, as suggested by Woodward et al. (2008).

## 8.9. Mixing Length Theory and Simulations

Mixing length theory (or MLT) commonly used for treating convection in stellar evolutionary calculations relies on assumptions and parameters that are often chosen based on convenient

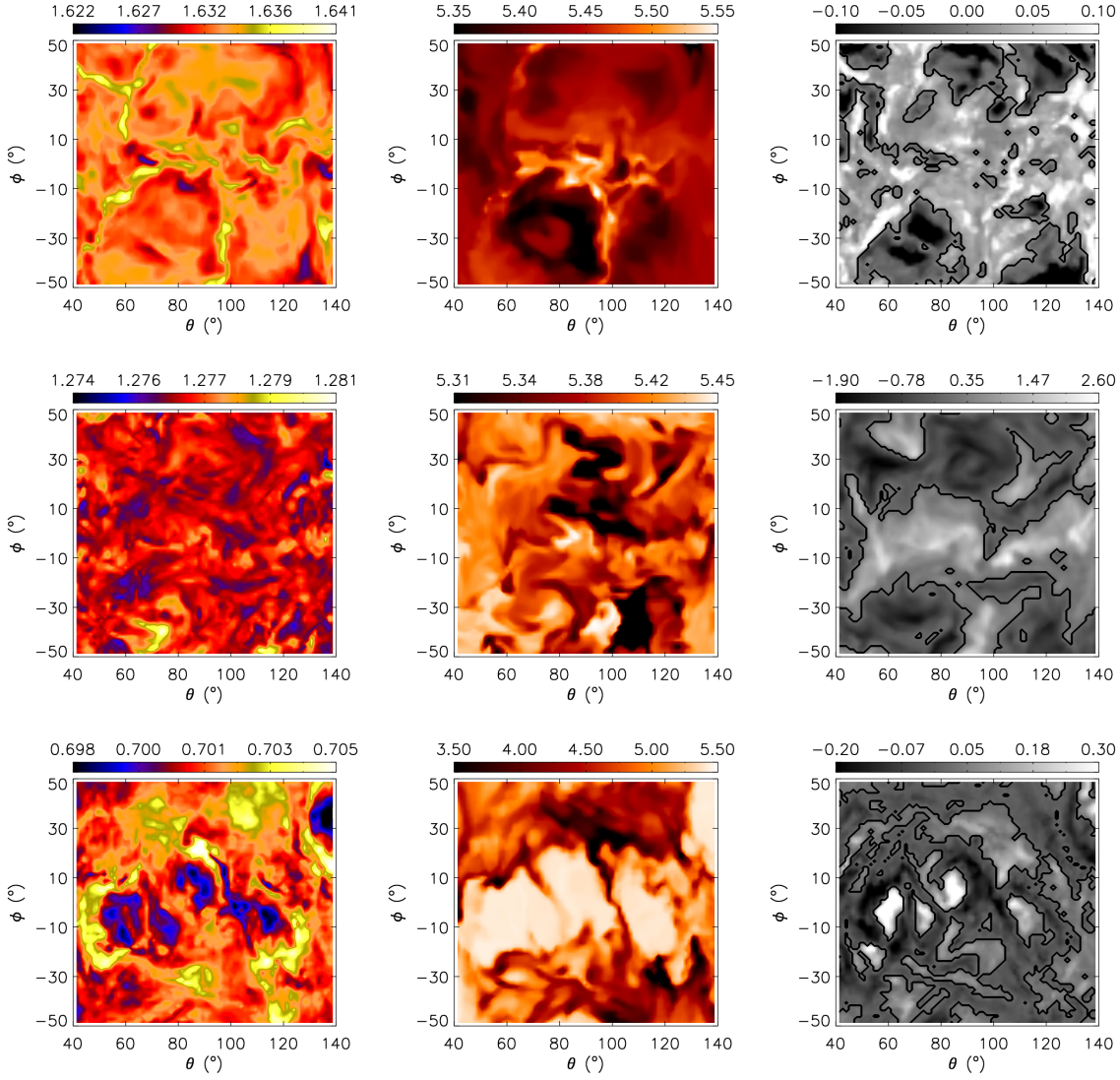


**Figure 8.11.:** Cuts through the 3D model hefl.3d at  $t = 4815$  s showing the angular variation of temperature (in units of  $10^8$  K; left panels),  $^{12}\text{C}$  mass fraction (in units of  $10^{-3}$ ; middle panels), and radial velocity (in units of  $10^5$  cm s $^{-1}$ ; right panels), respectively, at three different radii:  $r_1 = 4.8 \times 10^8$  cm (temperature maximum; top),  $r_2 = 6.5 \times 10^8$  cm (center of the convection zone; middle), and  $r_3 = 9.3 \times 10^8$  cm (top of convection zone, bottom). The black lines in the right panels mark the boundaries between positive and negative radial velocities.

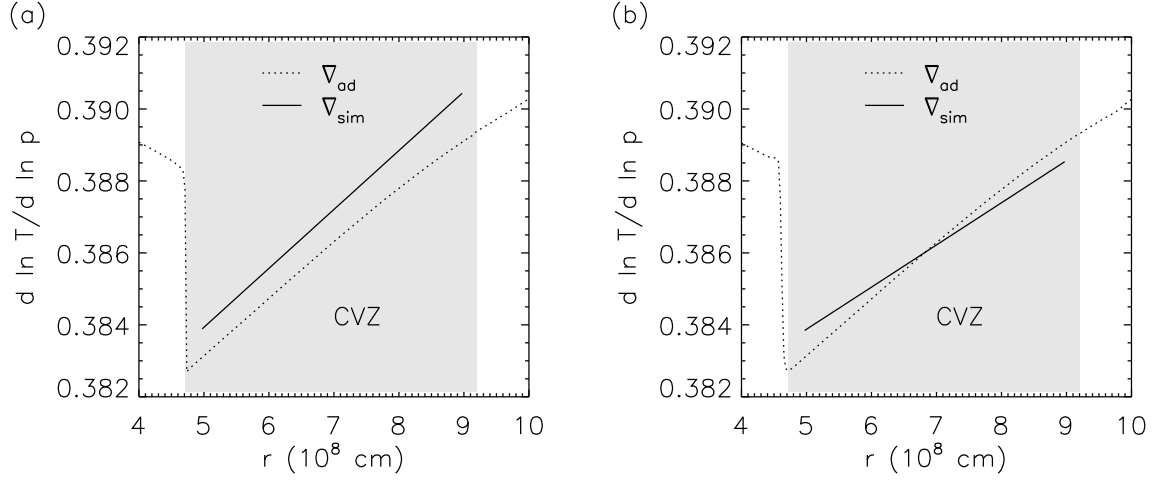


**Figure 8.12.:** (a) Radial distributions of the adiabatic temperature gradient  $\nabla_{\text{ad}}$  (dotted) and of the temperature gradients  $\nabla_{\text{sim}}$  of model hefl.3d (solid), respectively. The latter distribution is a linear fit to the gradients averaged over angle and over the first 200s of the evolution of the model. The gray shaded region marks the convection zone CVZ. (b) Same as left, but showing the radial distributions in the evolved convection zone averaged over roughly 3000s of evolutionary time.

ad-hoc arguments about the convective flow, like *e.g.* the value of the mixing length, the amount of upflow-downflow symmetry or the position where, within the convection zone, convective elements start to rise (Kippenhahn & Weigert 1990; Weiss et al. 2004).

MLT also assumes that the temperature of a convective element (blob) is the same as that of the ambient medium surrounding it when it starts to rise. However, as a blob will not rise until it is hotter than the surroundings, this MLT assumption is contradictory. MLT further assumes that once the blobs begin to rise they carry their surplus of heat lossless over a distance given by the mixing length before they release it to the surrounding gas instantaneously at the end of their path. These assumptions are also not fulfilled in general. Our simulations show that convective elements typically start their rise inside the star from the region of dominant nuclear burning where they are accelerated by buoyant forces. The assumptions of MLT that convective blobs form and begin their motion at different depths of the convection zone, and that the average convective blob propagates a distance equal to half of the assumed mixing length before dissolving with the surrounding gas (Kippenhahn & Weigert 1990), therefore do not hold. MLT finally also assumes a correlation between the thermodynamic variables and the velocity of the flow in a convection zone. However, the results of our simulations falsify this assumption (Fig. 8.11).

According to MLT, the temperature fluctuations in a convection zone are directly proportional to the mixing length and to the deviation of the temperature gradient of the model  $\nabla_{\text{sim}} = (d \ln T / d \ln p)_{\text{sim}}$  from the adiabatic one  $\nabla_{\text{ad}} = (d \ln T / d \ln p)_{\text{ad}}$ :

$$\frac{T'}{T} = (\nabla_{\text{sim}} - \nabla_{\text{ad}}) \frac{1}{H_p} \frac{\Lambda}{2} \quad (8.4)$$

where  $\Lambda$  is the mixing length,  $H_p$  the pressure scale height,  $T'$  the absolute value of the temperature deviation from the mean (horizontally averaged) temperature  $T$ , and  $p$  the pressure, respectively.

Since  $T'/T$  and  $\nabla_{\text{sim}} - \nabla_{\text{ad}}$  can directly be obtained from our simulations, we attempted to test MLT in a qualitative manner. Our simulations show that in the outer part of the con-

vection zone, *i.e.* in the region where the work done by buoyancy is getting smaller (Fig. 8.8), the temperature gradient of the models  $\nabla_{\text{sim}}$  becomes subadiabatic (see Fig. 8.12). Equation (8.4) which was derived for the adiabatic rise of convective bubbles would then imply that the temperature of convective elements should be lower than that of the surrounding gas (hence no convection) in the outer part of the convection zone, or that the value of  $\Lambda$  should be negative. However, convective elements do not rise adiabatically in our hydrodynamic simulations and the sub-adiabatic gradient means only that the convective elements start to cool faster than their surroundings. It does not imply necessarily that the elements are already cooler than the surrounding gas which would prevent the gas from being convectively active. Note that initially, the temperature gradient is super-adiabatic in the whole convection zone (see Fig. 8.12: a), because the stellar evolutionary model used as initial input for our simulations is computed under the assumptions of the MLT.

# 9

## Summary

We have presented one-dimensional, two-dimensional (axisymmetric) and three-dimensional hydrodynamic simulations of the core helium flash close to its peak. We found no hydrodynamic events that deviated significantly from the predictions of stellar evolutionary calculations. After an initial adjustment phase, the two- and three-dimensional models reached a quasi-steady state where the temperature and nuclear energy production rate were changing only slowly *i.e.* the core helium flash neither rips the star apart, nor significantly alters its structure.

Convection plays a crucial role in keeping the star in hydrostatic equilibrium, as one-dimensional hydrodynamic simulations demonstrated that thermal transport and expansion alone fail to prevent star from thermonuclear runaway.

Based on our two-dimensional simulation with the highest grid resolution (model hefl.2d.3), the convection followed the predictions of mixing length theory approximately, although the temperature gradient of our dynamically evolved two-dimensional models deviated slightly from that of the initial model obtained from (one-dimensional) stellar evolutionary calculations (the relative difference was lower than 1%). The maximum temperature  $\langle T \rangle_{max}$  rose at a rate of about  $40 \text{ K s}^{-1}$ , which was about 60% lower than the rate predicted by stellar evolutionary calculations. The mean convective velocity exceeded the velocities predicted by mixing length theory by up to factor of four.

During early evolution ( $t < 1000 \text{ s}$ ) of the model hefl.2d.3, the size of the convective region did not deviate from that of the initial (hydrostatic) model. However, after a stable convective pattern was established, the simulation showed that the convective flow, started to push the initial inner and outer boundary of the convection zone, due to the turbulent entrainment towards the center of the star at a velocity of  $2.3 \text{ m s}^{-1}$ , and towards the stellar surface at a velocity of  $14 \text{ m s}^{-1}$ , respectively. This produced a rapid growth in the radial extent of the convection zone on dynamic timescales. The presence of the turbulent entrainment was confirmed by three-dimensional simulations.

The fast growth of the convection zone due to entrainment has some potentially interesting implications. As entrainment is not considered in canonical stellar evolutionary calculations, stars evolving towards the core helium flash may never reach a state like the one in our initial stellar model. This may thus influence the growth of the convection zone observed in our

hydrodynamic simulations, as the thermodynamic conditions at the edges of the convection zone may differ.

If the convection zone does indeed grow rapidly, the main core helium flash studied here will never be followed by subsequent mini-flashes, as convection will lift the electron degeneracy in the helium core within 10 days. In addition, the helium core will likely experience an injection of hydrogen from the surrounding envelope (Fig. 1.2) within a month and undergo a violent nuclear burning phase powered by the CNO cycle. However, the growth of the central convection zone (within the core) simulated in our models does not have to continue until it will reach the outer convection zone extending up to the surface of the star. Hence, mixing of nuclear ashes to the stellar atmosphere does not necessarily take place. However a fast dynamic growth of the inner convection zone will lead to a change of the composition of the stellar core (less carbon and oxygen), and consequently of the luminosities of low-mass stars on the horizontal branch.

By comparison of two- and three-dimensional simulations we have found that the evolved convection of the three-dimensional models differs qualitatively and quantitatively from that of the two-dimensional (axisymmetric) ones. The typical convective structure in the two-dimensional simulations is a vortex with a diameter roughly equal to the width of convection zone, whereas the three-dimensional structures are smaller in extent and have a plume-like shape. The typical convective velocities are much higher in the two-dimensional models than in the three-dimensional ones. In the latter models the convective velocities tend to fit those predicted by the mixing length theory better. Both two- and three-dimensional models are characterized by an upflow-downflow asymmetry, where the fractional volume occupied by downflows is higher.





# Appendix

## A.1. Hydrodynamical Equations in Spherical Geometry

The hydrodynamic equations of a non-viscous multi-component reactive gas subject to a gravitational potential  $\Phi$  and having a heat conductivity  $K$  are given in spherical polar coordinates  $(r, \theta, \phi)$  by

$$\partial_t(\rho) + \frac{1}{r^2} \partial_r(r^2[\rho v_r]) + \frac{1}{r \sin \theta} \partial_\theta(\sin \theta[\rho v_\theta]) + \frac{1}{r \sin \theta} \partial_\phi[\rho v_\phi] = 0 \quad (\text{A.1})$$

$$\begin{aligned} \partial_t(\rho v_r) + \frac{1}{r^2} \partial_r(r^2[\rho v_r^2]) + \frac{1}{r \sin \theta} \partial_\theta(\sin \theta[\rho v_r v_\theta]) + \frac{1}{r \sin \theta} \partial_\phi([\rho v_r v_\phi]) - \\ - \frac{\rho v_\theta^2}{r} - \frac{\rho v_\phi^2}{r} + \partial_r p = -\rho \partial_r \Phi \end{aligned} \quad (\text{A.2})$$

$$\begin{aligned} \partial_t(\rho v_\theta) + \frac{1}{r^2} \partial_r(r^2[\rho v_\theta v_r]) + \frac{1}{r \sin \theta} \partial_\theta(\sin \theta[\rho v_\theta^2]) + \frac{1}{r \sin \theta} \partial_\phi[\rho v_\theta v_\phi] + \\ + \frac{\rho v_\theta v_r}{r} - \frac{\rho v_\phi^2 \cos \theta}{r \sin \theta} + \frac{1}{r} \partial_\theta p = -\rho \frac{1}{r} \partial_\theta \Phi \end{aligned} \quad (\text{A.3})$$

$$\begin{aligned} \partial_t(\rho v_\phi) + \frac{1}{r^2} \partial_r(r^2[\rho v_\phi v_r]) + \frac{1}{r \sin \theta} \partial_\theta(\sin \theta[\rho v_\theta v_\phi]) + \frac{1}{r \sin \theta} \partial_\phi([\rho v_\phi^2]) + \\ + \frac{\rho v_\phi v_r}{r} + \frac{\rho v_\phi v_\theta \cos \theta}{r \sin \theta} + \frac{1}{r \sin \theta} \partial_\phi p = -\rho \frac{1}{r \sin \theta} \partial_\phi \Phi \end{aligned} \quad (\text{A.4})$$

$$\begin{aligned}
\partial_t(\rho e) \frac{1}{r^2} \partial_r(r^2[v_r(\rho e + p) - K \partial_r T]) + \frac{1}{r \sin \theta} \partial_\theta(\sin \theta[v_\theta(\rho e + p) - K \frac{1}{r} \partial_\theta T]) + \\
\frac{1}{r \sin \theta} \partial_\phi[v_\phi(\rho e + p) - K \frac{1}{r \sin \theta} \partial_\phi T] = \\
-\rho(v_r \partial_r \Phi + v_\theta \frac{1}{r} \partial_\theta \Phi + v_\phi \frac{1}{r \sin \theta} \partial_\phi \Phi) + \rho \dot{S}
\end{aligned} \tag{A.5}$$

$$\begin{aligned}
\partial_t(\rho X_k) + \frac{1}{r^2} \partial_r(r^2[\rho v_r X_k]) + \frac{1}{r \sin \theta} \partial_\theta(\sin \theta[\rho v_\theta X_k]) + \\
\frac{1}{r \sin \theta} \partial_\phi[\rho v_\phi X_k] = \rho \dot{X}_k^S k = 1 \dots N_{nuc}
\end{aligned} \tag{A.6}$$

where  $\rho$ ,  $v_r$ ,  $v_\theta$ ,  $v_\phi$ ,  $p$ ,  $e$ ,  $T$ ,  $\dot{\varepsilon}$ ,  $X_k$ , and  $\dot{X}_k$  are the density, the radial velocity, the  $\theta$ -velocity, the rotation velocity, the pressure, the total specific energy, the temperature, the energy generation rate per mass due to reactions, the mass fraction of species  $k$ , and the change of this mass fraction due to reactions, respectively.  $N_{nuc}$  is the number of species the gas is composed of.

## A.2. Energy Fluxes

The various contributions to the total energy flux (Hurlburt et al. 1986; Achatz 1995) can be obtained by first integrating the hydrodynamic energy equation given in Appendix A.1 over the angular coordinates  $\theta$  and  $\phi$ . Then, one decomposes both the specific enthalpy  $\varepsilon + p/\rho$  (where  $\varepsilon$  is the specific thermal energy) and the specific kinetic energy  $v_i v_i/2$  into a horizontal mean and a perturbation,  $f \equiv \bar{f} + f'$ , and obtains

$$\partial_t E + \partial_r(F_C + F_K + F_R + F_E) = 0 \tag{A.7}$$

where

$$E = \int_V \rho e \, dV \tag{A.8}$$

$$F_C = \oint v_r \rho \cdot \left( \varepsilon + \frac{p}{\rho} \right)' r^2 d\Omega \tag{A.9}$$

$$F_K = \oint v_r \rho \cdot \left( \frac{1}{2} v_i v_i \right)' r^2 d\Omega, \quad i = 1, 2, 3 \tag{A.10}$$

$$F_R = - \oint K \partial_r T r^2 d\Omega \tag{A.11}$$

$$F_E = 4\pi r^2 \overline{v_r \rho} \cdot \left( \overline{\varepsilon + \frac{p}{\rho}} + \overline{\frac{1}{2} v_i v_i + \Phi} \right). \tag{A.12}$$

Here, the gravitational potential  $\Phi$  is assumed to be constant for simplicity. The sum of the various flux terms  $F_i$  give the total energy transported per unit time across a sphere of radius  $r$  by different physical processes. One has the convective (or enthalpy) flux,  $F_C$ , the flux of kinetic energy,  $F_K$ , and the flux due to heat conduction and radiation,  $F_R$ . Finally,  $F_E$ , includes all terms causing a spherical mass flow, *i.e.* the model's expansion or contraction, while  $F_C$  and  $F_K$  rest on deviations from this mean energy flow (vortices). The latter are the major contributors to the heat transport by convection.

In a similar way one can also formulate a conservation equation for the mean horizontal kinetic energy that provides further insight into the effects of convective motions. Using the other hydrodynamic equations (Eqs. A.1 to A.4), and the relation  $\partial_t(\rho v_i v_i/2) = v_i \partial_t(\rho v_i) - v_i v_i \partial_t \rho/2$ , one finds

$$\partial_t E_K + \partial_r(F_K + F_P + F_{E,K}) = P_A + P_P + P_{E,K} \quad (\text{A.13})$$

With  $F_K$  as introduced above, one obtains

$$E_K = \int_V \frac{\rho}{2} v_i v_i dV \quad (\text{A.14})$$

$$F_P = - \oint v_r p' r^2 d\Omega \quad (\text{A.15})$$

$$F_{E,K} = 4\pi r^2 \bar{v}_r \bar{\rho} \cdot \left( \frac{\bar{p}}{\rho} + \frac{\overline{v_i v_i}}{2} \right) \quad (\text{A.16})$$

$$P_A = - \oint v_r \rho' \partial_r \Phi r^2 d\Omega \quad (\text{A.17})$$

$$P_P = \oint p' \partial_i v_i r^2 d\Omega \quad (\text{A.18})$$

$$P_{E,K} = 4\pi r^2 \cdot (\bar{p} \overline{\partial_i v_i} - \bar{v}_r \bar{\rho} \partial_r \Phi) , \quad i = 1, 2, 3 \quad (\text{A.19})$$

where the  $P_i$  are source or sink terms of the kinetic energy. They are separated into the effect of buoyancy forces ( $P_A$ ), and the work due to density fluctuations ( $P_P$ , volume changes). By analyzing the various  $P_i$  one can determine what causes the braking or acceleration of the convective flow. The acoustic flux,  $F_P$ , describes the vertical transport of density fluctuations.  $F_{E,K}$  and  $P_{E,K}$  describe the effect of expansion (volume work, and work against the gravitational potential), similar to  $F_E$  in Eq. (A.12).



# List of Figures

1.1. Introduction: H-R diagram (a) and luminosity evolution (b) . . . . .	7
1.2. Introduction: Sketch of the helium core . . . . .	7
1.3. Introduction: Temperature (a) and density (b) profile . . . . .	8
1.4. Introduction: Time evolution of stellar structure (a,b) . . . . .	9
2.1. Properties of the System: Temperature gradients (a,b) . . . . .	15
2.2. Properties of the System: Energy generation rates (a,b) . . . . .	18
2.3. Properties of the System: Opacities . . . . .	20
4.1. Code: Numerical fluxes with PPM method (a,b,c,d) . . . . .	29
4.2. Code: Dissipation of the Kinetic Energy Field (a,b,c,d,e) . . . . .	31
4.3. Code: Double Mach Reflection (a,b,c) . . . . .	33
4.4. Code: Richardson extrapolation . . . . .	34
4.5. Code: One-Zone Nuclear Burning (a,b) . . . . .	35
4.6. Code: White dwarf detonation problem (a,b) . . . . .	36
4.7. Code: Density profile of a polytrope (a,b) . . . . .	39
5.1. Initial model M: $T$ , $p$ , $\rho$ , $X_i$ , $S$ and $\Psi$ (a, b, c, d, e, f) . . . . .	44
5.2. Initial model DM & JW: $T$ , $p$ , $\rho$ , $X_i$ , $S$ and $\Psi$ (a, b, c, d, e, f) . . . . .	46
5.3. Initial model SC: $T$ , $p$ , $\rho$ , $X_i$ , $S$ and $\Psi$ (a, b, c, d, e, f) . . . . .	47
6.1. One-D (model M): Evolution of $T$ , $\rho$ and $p$ (a,b,c,d) . . . . .	50
7.1. Two-D (model M): Temperature evolution (a) and convection velocities (b) . . . . .	52
7.2. Two-D (model M): $T$ , $\rho$ fluctuations in the convection zone and velocity field . . . . .	53
7.3. Two-D (model M): ${}^4\text{He}$ , ${}^{12}\text{C}$ and ${}^{16}\text{O}$ fluctuations in the convection zone . . . . .	54
7.4. Two-D (model M): Energy fluxes (a,b,c,d,e,f) . . . . .	56
7.5. Two-D (model M): Temporal evolution of convective boundaries (a,b) . . . . .	58
7.6. Two-D (model M): Long-term evolution of the temperature maximum . . . . .	59
7.7. Two-D (model M): Velocity magnitude at different times (a,b,c) . . . . .	60
7.8. Two-D (model M): Growth of the convection zone (a,b,c,d) . . . . .	61
7.9. Two-D (model M): Energy production (a) and temperature distribution (b) . . . . .	62
7.10. Two-D (model DM): $T$ , $\rho$ fluctuations in the convection zone and velocity field . . . . .	64
7.11. Two-D (model DM): ${}^4\text{He}$ , ${}^{12}\text{C}$ and ${}^{16}\text{O}$ fluctuations in the convection zone . . . . .	65
7.12. Two-D (model DM): Energy fluxes (a,b) . . . . .	66
7.13. Two-D (model JW): $T$ , $\rho$ fluctuations in the convection and velocity field . . . . .	67
7.14. Two-D (model JW): ${}^4\text{He}$ , ${}^{12}\text{C}$ and ${}^{16}\text{O}$ fluctuations in the convection zone . . . . .	68
7.15. Two-D (model JW): Energy fluxes (a,b) . . . . .	69
7.16. Two-D (model SC): $T$ fluctuations in the convection zones (a,b,c) . . . . .	70
8.1. Three-D & Two-D (model M): Kinetic energy density (a,b) . . . . .	75
8.2. Three-D & Two-D (model M): Total kinetic energy (a,b) . . . . .	76

8.3. Three-D & Two-D (model M): Velocity magnitude and power spectra (a,b,c,d,e)	77
8.4. Three-D & Two-D (model M): Auto-correlation functions (a,b)	78
8.5. Three-D (model M): Brunt-Väisälä buoyancy frequency	80
8.6. Three-D (model M): Outer convective boundary (a,b,c)	81
8.7. Three-D (model M): Different views of isosurfaces of the velocity field	82
8.8. Three-D & Two-D (model M): Various energy fluxes (a,b,c,d)	83
8.9. Three-D & Two-D (model M): Velocity components and MLT	86
8.10. Three-D (model M): Radial distributions of T and $\rho$ fluctuations (a,b)	87
8.11. Three-D (model M): Horizontal cuts through convection zone	88
8.12. Three-D & Two-D (model M): Temperature gradients (a,b)	89

# List of Tables

4.1. Parallel scaling behavior of the code Herakles . . . . .	40
5.1. Initial models: Properties of M, DM, JW & SC . . . . .	43
6.1. One-D (model M): Some properties of hydrodynamic simulations . . . . .	49
7.1. Two-D (model M): Some properties of hydrodynamic simulations . . . . .	51
7.2. Two-D (model M): Approximate rates for evolution of chemical species . . . . .	61
7.3. Two-D (model DM): Some properties of hydrodynamic simulations . . . . .	63
7.4. Two-D (model JW): Some properties of hydrodynamic simulations . . . . .	69
7.5. Two-D (model SC): Some properties of hydrodynamic simulations . . . . .	71
8.1. Three-D & Two-D (model M): Some properties of hydrodynamic simulations . .	74
8.2. Three-D & Two-D (model M): Fluctuations in the convection zone . . . . .	76
8.3. Three-D & Two-D (model M): Fluctuations at edges of the convection zone . . .	77





# Bibliography

- Achatz, K. 1995, in Master thesis, Technical University München [12](#), [16](#), [45](#), [57](#), [62](#), [63](#), [66](#), [94](#)
- Alastuey, A. & Jancovici, B. 1978, ApJ, 226, 1034 [37](#)
- Almgren, A. S., Bell, J. B., Rendleman, C. A., & Zingale, M. 2006, ApJ, 637, 922 [30](#)
- Arnett, D., Meakin, C., & Young, P. A. 2007, in IAU Symposium, Vol. 239, IAU Symposium, ed. F. Kupka, I. Roxburgh, & K. Chan, 247–257 [11](#), [86](#)
- Asida, S. M. & Arnett, D. 2000, ApJ, 545, 435 [11](#), [60](#), [71](#), [74](#), [75](#), [79](#), [85](#), [87](#)
- Bader, G. & Deuffhard, P. 1983, Numer. Math., 41, 373 [27](#), [32](#)
- Bazan, G. & Arnett, D. 1998, ApJ, 496, 316 [11](#), [73](#), [75](#), [79](#), [80](#)
- Beaudet, G., Petrosian, V., & Salpeter, E. E. 1967, ApJ, 150, 979 [19](#)
- Böhm-Vitense, E. 1958, Zeitschrift für Astrophysik, 46, 108 [11](#), [14](#), [41](#)
- Brummell, N. H., Clune, T. L., & Toomre, J. 2002, ApJ, 570, 825 [73](#), [76](#), [79](#), [80](#), [81](#), [83](#), [84](#), [85](#), [86](#)
- Campbell, S. W. & Lattanzio, J. C. 2008, in American Institute of Physics Conference Series, Vol. 990, First Stars III, ed. B. W. O’Shea & A. Heger, 315–319 [45](#), [63](#)
- Canuto, V. M. 2000, A&A, 357, 177 [17](#), [73](#)
- Cassisi, S., Schlattl, H., Salaris, M., & Weiss, A. 2003, ApJ, 582, L43 [45](#)
- Catelan, M. 2005, arXiv: astro-ph/0507464 [6](#)
- Cattaneo, F., Brummell, N. H., Toomre, J., Malagoli, A., & Hurlburt, N. E. 1991, ApJ, 370, 282 [76](#), [86](#)
- Chan, K. L. & Sofia, S. 1986, ApJ, 307, 222 [78](#), [83](#)
- Chan, K. L., Sofia, S., & Wolff, C. L. 1982, ApJ, 263, 935 [78](#)
- Chandrasekhar, S. 1967, An Introduction to the Study of Stellar Structure (New York: Dover Publications) [38](#)
- Clayton, D. D. 1968, Principles of stellar evolution and nucleosynthesis (New York: McGraw-Hill, 1968) [13](#), [19](#)
- Cole, P. W., Demarque, P., & Deupree, R. G. 1985, ApJ, 291, 291 [10](#), [58](#), [79](#)
- Cole, P. W. & Deupree, R. G. 1980, ApJ, 239, 284 [10](#), [45](#), [63](#)

- Cole, P. W. & Deupree, R. G. 1981, *ApJ*, 247, 607 [10](#), [11](#), [62](#), [63](#)
- Colella, P. & Glaz, H. H. 1984, *J.Comput.Phys.*, 59, 264 [27](#), [30](#)
- Colella, P. & Woodward, P. R. 1984, *J.Comput.Phys.*, 54, 174 [27](#), [28](#)
- Cox, A. N. & Stewart, J. N. 1970a, *ApJS*, 19, 243 [24](#)
- Cox, A. N. & Stewart, J. N. 1970b, *ApJS*, 19, 261 [24](#)
- Dalgaard, J. C. 2003, *Stellar Oscillations* (Institut for Fysik og Astronomi, Aarhus Universitet) [15](#)
- Dearborn, D. S. P., Lattanzio, J. C., & Eggleton, P. P. 2006, *ApJ*, 639, 405 [11](#)
- Demarque, P. & Mengel, J. G. 1971, *ApJ*, 164, 469 [10](#), [19](#), [45](#)
- Deupree, R. G. 1984a, *ApJ*, 282, 274 [10](#), [11](#)
- Deupree, R. G. 1984b, *ApJ*, 287, 268 [10](#), [11](#)
- Deupree, R. G. 1986, *ApJ*, 303, 649 [11](#)
- Deupree, R. G. 1996, *ApJ*, 471, 377 [11](#)
- Deupree, R. G. & Cole, P. W. 1983, *ApJ*, 269, 676 [10](#), [58](#), [79](#)
- Deupree, R. G. & Wallace, R. K. 1987, *ApJ*, 317, 724 [11](#)
- Dewitt, H. E., Graboske, H. C., & Cooper, M. S. 1973, *ApJ*, 181, 439 [24](#), [37](#)
- Edwards, A. C. 1969, *MNRAS*, 146, 445 [10](#)
- Fernando, H. 1991, *Annu.Rev.Fluid Mech.*, 23, 455 [16](#), [57](#), [79](#)
- Fornberg, B. 1977, *J.Comput.Phys.*, 25, 1 [75](#)
- Fryxell, B., Arnett, D., & Mueller, E. 1991, *ApJ*, 367, 619 [27](#), [36](#)
- Fujimoto, M. Y., Iben, I. J., & Hollowell, D. 1990, *ApJ*, 349, 580 [10](#), [11](#), [45](#), [59](#)
- Graboske, H. C., Dewitt, H. E., Grossman, A. S., & Cooper, M. S. 1973, *ApJ*, 181, 457 [37](#)
- Hansen, B. M. S. 2005, *ApJ*, 635, 522 [6](#)
- Härm, H. & Schwarzschild, M. 1964, *ApJ*, 139, 594 [9](#)
- Härm, R. & Schwarzschild, M. 1966, *ApJ*, 145, 496 [9](#)
- Herwig, F., Freytag, B., Hueckstaedt, R. M., & Timmes, F. X. 2006, *ApJ*, 642, 1057 [11](#), [17](#)
- Hurlburt, N. E., Toomre, J., & Massaguer, J. M. 1986, *ApJ*, 311, 563 [73](#), [75](#), [83](#), [84](#), [94](#)
- Hurlburt, N. E., Toomre, J., Massaguer, J. M., & Zahn, J.-P. 1994, *ApJ*, 421, 245 [73](#), [75](#), [79](#), [83](#), [84](#), [85](#), [86](#)
- Iben, I. & Renzini, A. 1984, *Phys. Rep.*, 105, 329 [11](#)
- Iben, Jr., I. 1975, *ApJ*, 196, 525 [24](#)

- Inman, C. L. & Ruderman, M. A. 1964, *ApJ*, 140, 1025 [19](#)
- Itoh, N., Hayashi, H., Nishikawa, A., & Kohyama, Y. 1996, *ApJS*, 102, 411 [24](#), [37](#)
- Itoh, N., Kohyama, Y., & Takeuchi, H. 1987, *ApJ*, 317, 733 [16](#)
- Itoh, N., Totsuji, H., Ichimaru, S., & Dewitt, H. E. 1979, *ApJ*, 234, 1079 [37](#)
- Kercek, A., Hillebrandt, W., & Truran, J. W. 1998, *A&A*, 337, 379 [11](#)
- Kercek, A., Hillebrandt, W., & Truran, J. W. 1999, *A&A*, 345, 831 [11](#)
- Kifonidis, K., Plewa, T., Janka, H.-T., & Müller, E. 2003, *A&A*, 408, 621 [11](#), [27](#)
- Kifonidis, K., Plewa, T., Scheck, L., Janka, H.-T., & Müller, E. 2006, *A&A*, 453, 661 [11](#), [27](#)
- Kippenhahn, R. & Weigert, A. 1990, *Stellar Structure and Evolution* (Stellar Structure and Evolution, XVI, 468 pp. 192 figs.. Springer-Verlag Berlin Heidelberg New York. Also Astronomy and Astrophysics Library) [5](#), [9](#), [14](#), [41](#), [79](#), [89](#)
- Kippenhahn, R., Weigert, A., & E., H. 1967, *Methods in Computational Physics* (Academic Press, New York) [41](#)
- Kuhlen, M., Woosley, W. E., & Glatzmaier, G. A. 2003, in *Astronomical Society of the Pacific Conference Series*, Vol. 293, *3D Stellar Evolution*, ed. S. Turcotte, S. C. Keller, & R. M. Cavallo, 147–+ [30](#)
- Landau, L. D. & Lifshitz, E. M. 1966, *Hydrodynamik* (Lehrbuch der theoretischen Physik, Berlin: Akademie-Verlag, 1966) [16](#)
- Lattanzio, J., Dearborn, D., Eggleton, P., & Dossa, D. 2006, *ArXiv: astro-ph/0612147* [11](#), [74](#)
- McWilliams, J. 1984, *J.Fluid.Mech.*, 146, 21 [75](#)
- Meakin, C. A. & Arnett, D. 2006, *ApJ*, 637, L53 [11](#)
- Meakin, C. A. & Arnett, D. 2007a, *ApJ*, 665, 690 [30](#), [55](#), [86](#)
- Meakin, C. A. & Arnett, D. 2007b, *ApJ*, 667, 448 [11](#), [17](#), [27](#), [57](#), [59](#), [60](#), [74](#), [75](#), [79](#), [80](#), [83](#), [84](#), [85](#), [87](#)
- Miczek, F. 2008, in *Master thesis*, Technical University München [31](#)
- Mocák, M., Müller, E., Weiss, A., & Kifonidis, K. 2008, *A&A*, 490, 265 [11](#), [17](#)
- Müller, E. 1986, *A&A*, 162, 103 [34](#), [36](#)
- Müller, E. 1998, in *Lecture Notes in Physics*, Berlin Springer Verlag, Vol. 27, *Computational methods for astrophysical fluid flow*, ed. O. Steiner & A. Gautschi, 343–480 [23](#)
- Müller, E., Fryxell, B., & Arnett, D. 1991, in *ESO/EIPC Workshop on Supernova 1987A and other Supernovae*, p. 99 - 116, 99–116 [27](#), [36](#)
- Müller, E. & Steinmetz, M. 1995, *Comp.Phys.Commun.*, 89, 45 [27](#), [38](#)
- Muthsam, H. J., Goeb, W., Kupka, F., Liebich, W., & Zoechling, J. 1995, *A&A*, 293, 127 [57](#), [73](#), [75](#), [83](#), [85](#), [86](#)
- Nordlund, A. & Dravins, D. 1990, *A&A*, 228, 155 [86](#)

- Paczynski, B. & Tremaine, S. D. 1977, *ApJ*, 216, 57 [10](#)
- Plewa, T. & Müller, E. 1999, *A&A*, 342, 179 [27](#)
- Porter, D. H. & Woodward, P. R. 1994, *ApJS*, 93, 309 [51](#), [63](#), [69](#), [75](#)
- Potekhin, A. Y., Chabrier, G., & Yakovlev, D. G. 1997, *A&A*, 323, 415 [25](#)
- Press, W. H., Tutorials, S. A., Vetterling, W. T., & P., F. B. 1992, in *Numerical Recipes in FORTRAN, The Art of Scientific Computing*, Second Edition (Cambridge: Cambridge University Press), Vol. 1 [27](#), [32](#), [34](#), [41](#)
- Ramadurai, S. 1976, *MNRAS*, 176, 9 [10](#), [19](#)
- Rast, M. P., Nordlund, A., Stein, R. F., & Toomre, J. 1993, *ApJ*, 408, L53 [87](#)
- Reeves, H. 1963, *ApJ*, 138, 79 [19](#)
- Refsdal, S. & Weigert, A. 1970, *A&A*, 6, 426 [6](#)
- Schlattl, H., Cassisi, S., Salaris, M., & Weiss, A. 2001, *ApJ*, 559, 1082 [10](#), [45](#), [59](#)
- Schneider, T., Botta, N., Geratz, K. J., & Klein, R. 1999, *J.Comput.Phys.*, 155, 248 [30](#)
- Schwarzschild, M. & Härm, R. 1962, *ApJ*, 136, 158 [9](#)
- Singh, H. P., Roxburgh, I. W., & Chan, K. L. 1995, *A&A*, 295, 703 [73](#), [79](#)
- Singh, H. P., Roxburgh, I. W., & Chan, K. L. 1998, *A&A*, 340, 178 [73](#)
- Sitine, I. V., Porter, D. H., Woodward, P. R., Hodson, S. W., & Winkler, K.-H. 2000, *J.Comput.Phys.*, 158, 225 [27](#)
- Smagorinsky, J. S. 1963, *Mon. Weather Rev.*, 91, 99 [17](#)
- Strang, G. 1968, *SIAM J.Numer.Anal.*, 5, 506 [27](#)
- Suda, T., Aikawa, M., Machida, M. N., Fujimoto, M. Y., & Iben, I. J. 2004, *ApJ*, 611, 476 [45](#)
- Sweigart, A. V. & Gross, P. G. 1978, *ApJS*, 36, 405 [10](#), [58](#)
- Swesty, F. D. & Myra, E. S. 2006, *ArXiv Astrophysics e-prints* [38](#)
- Thomas, H.-C. 1967, *Zeitschrift fur Astrophysik*, 67, 420 [8](#), [10](#), [19](#)
- Timmes, F. X. & Swesty, F. D. 2000, *ApJS*, 126, 501 [22](#)
- Tomasko, M. G. 1970, *ApJ*, 162, 125 [9](#)
- Turkel, E. 1999, *Annu. Rev. Fluid Mech.*, 31, 385 [30](#), [55](#)
- Villere, K. R. 1976, PhD thesis, AA(California Univ., Santa Cruz.) [10](#)
- Vitense, E. 1953, *Zeitschrift fur Astrophysik*, 32, 135 [11](#), [14](#), [41](#)
- Wagenhuber, J. 1996, PhD thesis, , Techn. Univ. München, (1996) [45](#)
- Weiss, A., Hillebrandt, W., Thomas, H.-C., & Ritter. 2004, *Cox and Giuli's Principles of Stellar Structure* (Gardners Books) [5](#), [9](#), [14](#), [24](#), [41](#), [89](#)

- Weiss, A. & Schlattl, H. 2000, *A&AS*, 144, 487 [43](#), [45](#)
- Weiss, A. & Schlattl, H. 2007, *Ap&SS*, 341 [43](#), [45](#)
- Weiss, A., Schlattl, H., Salaris, M., & Cassisi, S. 2004, *A&A*, 422, 217 [45](#)
- Wickett, A. J. 1977, in *Lecture Notes in Physics*, Berlin Springer Verlag, Vol. 71, Problems of Stellar Convection, ed. E. A. Spiegel & J.-P. Zahn, 284–289 [10](#)
- Wood, P. R. & Zarro, D. M. 1981, *ApJ*, 247, 247 [45](#)
- Woodward, P. & Colella, P. 1984, *Journal of Comp.Phys.*, 54, 115 [32](#)
- Woodward, P., Herwig, F., Porter, D., et al. 2008, in *American Institute of Physics Conference Series*, Vol. 990, First Stars III, 300–308 [87](#)
- Yakovlev, D. G. & Urpin, V. A. 1980, *Soviet Astronomy*, 24, 303 [25](#)
- Zahn, J.-P. 1991, *A&A*, 252, 179 [75](#)
- Zimmermann, R. 1970, PhD thesis, University of California at Los Angeles, (1970) [10](#)



# Acknowledgment

For the last three wonderful and enriching years I want to thank mainly my both supervisors Ewald Müller and Achim Weiss. They were leading me always carefully on my way in very relaxed atmosphere. The same big thanks belongs also to Konstantinos Kifonidis whose experience with hydrodynamical codes and numerical simulations was essential for the toughest problems I've encountered during my PhD and allowed me to extend the Herakles code in a reasonable time.

## Danke schön

Thanks to all my friends who were here in Munich and at the MPA with me. I had a great time with you chaps. Our unforgettable parties have stuck to my mind I hope forever. Especially, thanks to Marco Baldi, Umberto Maio and Raphael Gobat who were here with me from the very first moments.

Special thanks belongs to my family at home in Slovakia. Home is home, wherever it is. Thank you za Vašu trpezlivosť a pomoc. Thanks to my friends and teachers from my Alma Matter. It is always so good to see and talk to you again. Thank you Norbi; “Yeahh, you're right, it was great to share again the same flat”

Thank you Evka, for great time and care which you were giving to me during my studies. Svet a život je s tebou pre mňa omnoho krajší.

I want thank to the Leibniz-Rechenzentrum of the Bavarian Academy of Sciences and Humanities and to the Rechenzentrum Garching where all my simulations were performed.

I want to thank Frank Timmes for some of his public Fortran subroutines which I used in the Herakles code for calculating of the core helium flash models. Thanks also to Kurt Achatz, whose hydrodynamic simulations of the core helium flash as part of his diploma work inspired us. I am indebted to Casey Meakin for several enlightening discussions and helpful comments.